Interaction of atmospheric boundary layer flow with wind turbines: theoretical and experimental studies

THÈSE N° 7529 (2017)

PRÉSENTÉE LE 10 FÉVRIER 2017

À LA FACULTÉ DE L'ENVIRONNEMENT NATUREL, ARCHITECTURAL ET CONSTRUIT LABORATOIRE D'INGÉNIERIE ÉOLIENNE ET D'ÉNERGIE RENOUVELABLE PROGRAMME DOCTORAL EN MÉCANIQUE

ÉCOLE POLYTECHNIQUE FÉDÉRALE DE LAUSANNE

POUR L'OBTENTION DU GRADE DE DOCTEUR ÈS SCIENCES

PAR

Majid BASTANKHAH

acceptée sur proposition du jury:

Prof. F. Gallaire, président du jury Prof. F. Porté Agel, directeur de thèse Prof. J. N. Sørensen, rapporteur Prof. C. Meneveau, rapporteur Prof. K. Mulleners, rapporteuse





Acknowledgements

This dissertation owes its existence to the help, support and inspiration of several people. First, I would like to express my sincere appreciation and deepest gratitude to my advisor, Prof. Fernando Porté-Agel. I am indebted to his support and availability during my PhD. Fernando is one of the best teachers that I have ever seen, and without his guidance and persistent help, this dissertation would not have been possible. I would also like to thank my committee members, Prof. Jens Nørkær Sørensen, Prof. Charles Meneveau, Prof. Karen Mulleners and Prof. François Gallaire for their valuable suggestions and comments on this dissertation.

I had this opportunity to work with very nice people in WiRE who created an enjoyable and unforgettable environment for me during my PhD. My sincere thanks go to my current colleagues: Sina, Fernando, Vincent, Ka Ling, Carole, Jiannong, Wai Chi, Lionel, Kevin and Farshid; and the former ones: Mahdi, Vera, Deepu, Joel, Valerio, Corinne, Corey, Ting and so many others whom I had the privilege to work with and learn from. Thanks for being not just great colleagues but better friends!

I am also indebted to my friends in Lausanne who supported and helped me on so many levels and made my stay in beautiful Switzerland more pleasant. Special thanks go to my close friends: Mokhtar, Samira, Farhang, Saba, Nima, Sahar, Elham, Amin, Samira Asgari, Somayyeh, Mahdi Khorramshahi, Mohammad Razzaghi, Reza, Elaheh, Mostafa, Mohammad Azadifar and so many other friends that are too numerous to be mentioned here.

I owe to my parents all the things that I have, and I would like to thank them from the bottom of my heart for all their sacrifices and difficulties that they went through for me. I also would like to thank my siblings (Masoud, Mahsa and Yasaman) for their spiritual support and empathy. Special thanks also go to my parents-in-law for their kindness and support.

Last but definitely not least, I would like to thank my wife and my best friend Arezou for her love, unconditional support and all her encouragement during the last five years. I cannot imagine how I could have finished this dissertation without her countless sacrifices and supports. Words cannot express my appreciation to you, Arezou! Thank you so much for sharing your life with me.

Abstract

As wind turbines operate within the atmospheric boundary layer (ABL), the study of their interaction with the ABL flow can help us better understand and predict their performance. In addition to the performance of wind turbines, this interaction has an effect on the flow both upwind and downwind (i.e., wake region) of the turbines. In particular, the study of turbine wakes is of great importance because they are the main cause of power losses and fatigue loads in wind farms. In the current thesis, four studies are conducted to fully examine the turbine interaction with the ABL flow, with an emphasis on turbine wakes.

In the first study, a new analytical wake model is proposed and validated to predict the wind velocity distribution in the far-wake region, where downwind turbines usually operate. The proposed model is derived by applying the conservation of mass and momentum and assuming a Gaussian distribution for the velocity deficit in the wake. This simple model only requires one parameter to predict the velocity distribution in the far wake of a wind turbine. In general, it is found that the velocity deficit in the wake predicted by the proposed analytical model is in good agreement with the experimental and numerical data. Furthermore, the results show that the new model predicts the power extracted by downwind wind turbines more accurately than other common analytical models, some of which are based on less accurate assumptions like considering a top-hat shape for the velocity deficit.

In the second study, wind tunnel measurements are carried out to systematically investigate turbine wakes under yawed conditions. The detailed experimental data are used to perform a budget study of the continuity and Reynolds-averaged Navier-Stokes equations. This theoretical analysis reveals some notable features of the wakes of yawed turbines, such as the asymmetric distribution of the wake skew angle with respect to the wake center. Under highly yawed conditions, the formation of a counter-rotating vortex pair in the wake cross-section as well as the vertical displacement of the wake center are also shown and analyzed. Finally, this study enables us to develop general governing equations upon which a simple and computationally inexpensive analytical model is built. The proposed model aims at predicting the wake deflection and the far-wake velocity distribution for yawed turbines. The findings of this study can be especially useful to assess the possibility of optimizing wind-farm power production by controlling the yaw angle of the turbines.

In the third study, comprehensive wind tunnel experiments are performed to study the interaction of a turbulent boundary layer with a wind turbine operating under different tip-speed ratios and yaw angles. Force and power measurements are performed to characterize the wind turbine performance. Moreover, a high-resolution stereoscopic particle-image velocimetry

Acknowledgements

(S-PIV) system and hot-wire anemometry are used to study the flow in the upwind, near-wake and far-wake regions. This study provides new insights on the turbine and flow characteristics such as the evolution of tip vortices and wake meandering.

Finally, the last study concerns the design and the performance analysis of a new three-bladed horizontal-axis miniature wind turbine with a rotor diameter of 15 cm. Due to its small size, this turbine is particularly suitable for studies of wind farm flows and the interaction of the turbine with an incoming boundary-layer flow. Special emphasis is placed on accurate measurements of the mechanical power extracted by the miniature turbine from the incoming wind. In order to do so, a new setup is developed to measure the torque of the rotor shaft. The thrust and power coefficients of the miniature turbine are found to be around 0.8 and 0.4 in optimal conditions, respectively, which are close to the ones of large-scale turbines in the field.

Key words: Analytical model; Atmospheric boundary layer; Miniature wind turbine; Power coefficient; Thrust coefficient; Torque measurements; Turbulent boundary layer; Velocity deficit; Wake measurements; Wind tunnel experiments; Wind turbine wakes; Yaw angle; Yawed condition

Résumé

Les éoliennes fonctionnant dans la couche limite atmosphérique (CLA), l'étude de leur interaction avec l'écoulement de la CLA aide à une meilleure compréhension et à prédire les performances de celles-ci. En plus d'affecter les performances de l'éolienne, cette interaction a un effet sur l'écoulement en amont et en aval (i.e. le sillage). En particulier, l'étude du sillage des éoliennes est primordiale car il est la principale cause de la réduction de la production d'énergie et des charges en fatigue des parcs éoliens. Cette thèse présente quatre études qui explorent l'interaction entre la turbine et l'écoulement de la CLA, avec une emphase sur le sillage de l'éolienne.

Dans la première étude, un nouveau modèle analytique est proposé et validé afin de prédire la distribution de vitesse dans la région éloignée en aval de l'éolienne, où opèrent habituellement d'autres éoliennes. Le modèle proposé est dérivé en appliquant les lois de conservation de la masse et du moment en faisant l'hypothèse que le déficit de vitesse dans le sillage suit une loi gaussienne. Ce modèle simple ne requiert qu'un paramètre pour prédire la distribution de vitesse. Le déficit de vitesse calculé par ce modèle correspond en général au mesures expérimentales et aux études numériques disponibles. De plus, la puissance produite par une éolienne située dans le sillage d'une autre est calculée avec plus de précision avec le nouveau modèle qu'avec d'autres modèles analytiques basés sur des hypothèses moins précises, telle qu'une distribution uniforme pour le déficit de vitesse.

Dans la deuxième étude, une campagne de mesures en soufflerie est menée afin d'investiguer le sillage d'éoliennes lorsque le plan de la turbine n'est pas perpendiculaire à l'écoulement et qu'un angle de lacet est formé (yawed conditions). Les données expérimentales sont ensuite utilisées pour faire un bilan de masse et de moment, en considérant un modèle RANS (Raynolds-averaged Navier-Stokes). Cette étude théorique révèle des caractéristiques notables des sillages créés par des éoliennes avec un angle de lacet, notamment une distribution asymétrique de l'angle d'obliquité par rapport au centre du sillage. Lorsque l'angle de lacet devient important, la formation d'une paire de tourbillons contrarotatifs dans une section normale au sillage ainsi qu'un déplacement vertical du centre du sillage sont décrits et analysés. Finalement cette étude permet de développer un ensemble d'équations constitutives sur lesquelles est basé et implémenté un modèle analytique simple et computationnellement efficace. Le but de ce modèle est de prédire la déflexion du sillage et la distribution de vitesse loin en aval d'une turbine avec un angle de lacet. Les conclusions de cette étude peuvent être particulièrement utiles pour valider la possibilité d'optimiser un parc éolien en contrôlant l'angle de lacet des turbines.

Acknowledgements

Dans la troisième étude, une campagne de mesures en soufflerie complète est conduite pour étudier l'interaction entre une couche limite turbulente et une turbine fonctionnant avec des angles de lacets et des rapport de vitesse de pointe différents. Des mesures de force et de puissance sont faites afin de caractériser les performances de l'éolienne. En plus, des mesures haute-résolution de vélocimétrie stéréoscopique par images de particules (S-PIV) et d'anémométrie avec un fil chaud sont faites en amont de la turbine, dans le sillage proche et dans le sillage lointain. Cette étude fournit de nouveaux éléments sur les éoliennes et les caractéristiques de l'écoulement tel que l'évolution des tourbillons marginaux et de la déviation du centre du sillage.

Pour terminer, la dernière étude concerne la conception et l'analyse de performance d'une nouvelle géométrie d'éolienne miniature à trois pales à axe horizontal dont le diamètre du rotor est de 15 cm. Grâce à sa petite taille, cette turbine est particulièrement adaptée à des études de l'écoulement dans des parcs éoliens et des interactions avec une couche limite. Une attention particulière est portée afin d'obtenir des mesures précises de la puissance du vent extraite par les éoliennes miniatures. Afin de remplir ces objectifs, un nouveau dispositif est développé pour mesurer le couple résistant sur l'arbre du rotor. Les coefficients de poussée et de puissance des éoliennes miniatures sont autour de 0.8 et 0.4 dans des conditions optimales, qui sont proches de celles des parcs éoliens existants.

Mots clefs : Modèle analytique ; Couche limite turbulente ; Éolienne miniature ; Coefficient de puissance ; Coefficient de poussée ; Mesures de couple ; Couche limite turbulente ; Déficit de vitesse ; Mesures de sillage ; Expériences en soufflerie ; Sillage d'éoliennes ; Angle de lacet

Contents

Ac	knov	wledgements	j
Ał	ostra	ct (English/Français)	iii
Co	onter	nts	vii
Li	st of	figures	ix
Li	st of	tables	xvi
1	Intr	roduction	1
2	A ne	ew analytical model for wind-turbine wakes	3
	2.1	Introduction	3
	2.2	Wake model	7
	2.3	Results and discussion	9
	2.4	Summary	16
3	Exp	erimental and theoretical study of yawed-turbine wakes	19
	3.1	Introduction	20
	3.2	Wind tunnel measurements	22
	3.3	Governing equations	27
		3.3.1 Continuity equation	27
		3.3.2 Reynolds-Averaged Navier-Stokes (RANS) equations	31
		3.3.3 Integral form of RANS equations	35
	3.4	Self-similarity	38
	3.5	Model derivation for the far-wake region	40
	3.6	Onset of the far-wake region	43
	3.7	Model predictions	49
	3.8	Summary	52
	3.9	Appendix 1	54
	3.10	Appendix 2	55

Contents

4	Win	nd tunnel study of a wind turbine under different operating conditions	57	
	4.1	Introduction	58	
		4.1.1 Wind turbine performance	58	
		4.1.2 Upwind region	59	
		4.1.3 Near-wake region	60	
		4.1.4 Far-wake region	60	
	4.2	Experimental setup and incoming flow conditions	62	
	4.3	results and discussions	65	
		4.3.1 Wind turbine performance	65	
		4.3.2 Upwind region	67	
		4.3.3 Near-wake region	69	
		4.3.4 Far-wake region	73	
		4.3.5 POD analysis	80	
	4.4	Summary	84	
5	A ne	ew miniature wind turbine for wind tunnel experiments	87	
	5.1	Introduction	88	
	5.2	Wind turbine design	90	
		5.2.1 Rotor size	90	
		5.2.2 Airfoil geometry	90	
		5.2.3 Design tip-speed ratio	91	
		5.2.4 Optimum chord and twist distributions	93	
	5.3	Wind turbine performance	93	
		5.3.1 Thrust force	93	
		5.3.2 Power extraction	96	
	5.4	Turbine interaction with a turbulent boundary layer	103	
	5.5	Summary	109	
	5.6	Appendix 1	110	
6	Ove	erall summary and future research perspectives	113	
		Overall summary	113	
	6.2	Future research perspectives	115	
Ri	hling		129	
Cı	arric	ulum Vitae	131	

List of Figures

2.1	Schematic of the vertical profiles of the mean velocity (<i>top</i>) and velocity deficit	
	(bottom) downwind of a wind turbine obtained by assuming: (a) a top-hat and	_
	(b) a Gaussian distribution for the velocity deficit in the wake	5
2.2	Schematic of the two control volumes: (a) downwind of the wind turbine, and	_
	(b) around the wind turbine	6
2.3	The self-similar velocity deficit profiles of the wind-tunnel measurements (Chamor and Porté-Agel, 2010) (Case 1) and the LES data (Wu and Porté-Agel, 2012) (Cases	ro
	2-5) at different downwind distances	10
2.4	Normalized standard deviation of the velocity deficit profiles: case 1 (<i>asterisk</i>), case 2 (<i>square</i>), case 3 (<i>triangle</i>), case 4 (<i>circle</i>) and case 5 (<i>crosses</i>). Fitted lines	
	are represented by solid lines	11
2.5	Normalized velocity deficit, at hub height, versus normalized downwind distance in the wake of wind turbines (<i>Cases 1-5</i>): Wind-tunnel measurements (Chamorro and Porté-Agel, 2010) (<i>crosses</i>), LES data (Wu and Porté-Agel, 2011, 2012) (<i>open circle</i>), new proposed model (<i>solid line</i>), the model proposed by Jensen (1983)	
	(dashed line) and the model proposed by Frandsen et al. (2006) (dotted line)	12
2.6	Contours of streamwise velocity (ms^{-1}) in the vertical plane normal to the wind	
	turbine, at zero span (Case 1): New proposed model (top) and wind-tunnel	
	measurements (Chamorro and Porté-Agel, 2010) (bottom)	14
2.7	Vertical profiles of the normalized velocity deficit in the wakes of real-scale turbines installed on flat surfaces with different roughness lengths (Cases 2-5): LES data (Wu and Porté-Agel, 2012) (<i>open circle</i>), new proposed model (<i>solid line</i>), the model proposed by Jensen (1983) (<i>dashed line</i>) and the model proposed	
0.0	by Frandsen et al. (2006) (dotted line)	15
2.8	Variation of $P_{av}/P_{LES,av}$ at $x/d_0 = 7$ as a function of wind direction for different analytical models: Case 2 (<i>square</i>), Case 3(<i>triangle</i>), Case 4 (<i>circle</i>), and Case 5 (<i>crosses</i>)	16
3.1	Characteristics of the incoming turbulent boundary layer: (a) the normalized mean streamwise velocity profile, and (b) the streamwise turbulence intensity profile. The <i>horizontal dashed lines</i> represent the turbine hub height. (c) The normalized mean streamwise velocity profile in a semi-logarithmic scale. The <i>solid line</i> shows the fitted logarithmic profile	23

3.2	Turbine performance versus tip-speed ratio (thrust coefficient C_T (<i>left</i>), and	V
	power coefficient C_p (right)) for different yaw angles: $\gamma = 0^{\circ}$ (circle), $\gamma = 10^{\circ}$ (diamond),
	$\gamma = 20^{\circ} (square)$, and $\gamma = 30^{\circ} (triangle)$. For red-colored points, PIV measurements	24
		24
3.3	Contours of the normalized mean streamwise velocity \bar{u}/\bar{u}_h in the horizontal	
	plane at hub height downwind of a turbine for different yaw angles ($\gamma = 0^{\circ}$, 10° ,	
	20° and 30°) at $\lambda = \lambda_o$. White dots and white lines represent the wake-center	
	trajectory in the horizontal plane obtained from the wind tunnel measurements,	
	and Jiménez et al. (2010) (Eq. 3.1), respectively. Black lines show the initial wake	
	deflection predicted by Coleman et al. (1945) (Eq. 3.44). Overlapped locations of	
	PIV planes are indicated by vertical dashed lines.	25
3.4	Contours of the normalized mean spanwise velocity (\bar{v}/\bar{u}_h) in the horizontal	
	plane at hub height downwind of a turbine for two different yaw angles (γ =	
	0° , and 30°) at $\lambda = \lambda_o$. Black dots represent the wake center trajectory in the	
	horizontal plane, and overlapped locations of PIV planes are indicated by vertical	
	dashed lines	25
3.5	Contours of the normalized streamwise velocity deficit in yz planes at different	
	downwind locations and different yaw angles for a turbine operating at λ =	
	λ_o . Black circles indicate the frontal area of the wind turbine and white dots	
	represent the wake-center position at each downwind location. The vector field	
		26
3.6	Contours of the terms of the mean continuity equation (Eq. 3.4) in the horizontal	
	plane at hub height for two different yaw angles ($\gamma = 0^{\circ}$, and 30°) at $\lambda = \lambda_o$.	
	Contours are non-dimensionalized with \bar{u}_h and d . Black dots represent the	
	locus of the maximum velocity deficit in the measured plane, and overlapped	
	ž v	28
3.7	Schematic figure of the mechanism leading to the formation of the CVP	29
3.8	Wake center displacement predicted by the potential theory. Red curves show	
	the displacement of the wake center, and blue ones show the displacement of	
	the CVP. The <i>Horizontal dashed lines</i> indicate the initial position of the wake	
	center which is equal to the normalized turbine hub height z_h/d . The initial	
	position of the pair of vortices is $z_h/d \pm 0.5$. Vectors show the flow field at $t = 1.5$ s.	31
3.9	Contours of the terms of the x -RANS equation (Eq. 3.9) measured in the horizon-	
	tal plane at hub height for two different yaw angles ($\gamma = 0^{\circ}$, and 30°) at $\lambda = \lambda_o$.	
	Contours are non-dimensionalized with \bar{u}_h^2 and d . Black dots represent the	
	locus of the maximum velocity deficit in the measured plane, and overlapped	
	locations of PIV planes are indicated by vertical dashed lines	32
3.10	Contours of the terms of the x -RANS equation (Eq. 3.9) measured in a yz plane	
	at $x/d = 6$ for two different yaw angles ($\gamma = 0^{\circ}$, and 30°) at $\lambda = \lambda_o$. Contours are	
	non-dimensionalized with \bar{u}_h^2 and d . Black circles indicate the frontal area of	
	the wind turbine. The vector field represents in-plane velocity components :	32

3.11	Lateral profiles of the terms of the x-RANS equation (Eq. 3.9) at $x/d = 6$ for $x = 30^{\circ}$ and $\lambda = \lambda$. Profiles are non-dimensionalized with \bar{u}^2 and d	34
2 12	$\gamma = 30^{\circ}$ and $\lambda = \lambda_o$. Profiles are non-dimensionalized with \bar{u}_h^2 and d Variation of the maximum values of the dominant terms of the <i>x</i> -RANS equation	34
3.12	•	
	(Eq. 3.9) at hub height as a function of the downwind distance for two different very angles $(v = 0^\circ)$ and 20°) at $1 = 1$. Profiles are non-dimensionalized with \bar{v}^2	
	yaw angles ($\gamma = 0^{\circ}$, and 30°) at $\lambda = \lambda_o$. Profiles are non-dimensionalized with \bar{u}_h^2	24
0.10	and d .	34
3.13	Variation of θ , $\frac{1}{\bar{u}_h} \frac{\partial \bar{u}}{\partial (y/d)}$ and $\frac{\bar{u}}{\bar{u}_h}$ in the spanwise direction at three different downwind positions $(x/d-2, 4, \text{ and } 5)$ for a turbing with $x=20^\circ$ and $1=1$.	25
0.14	wind positions ($x/d = 3$, 4, and 5) for a turbine with $\gamma = 30^{\circ}$ and $\lambda = \lambda_0$	35
3.14	Contours of the terms of the <i>y</i> -RANS equation (Eq. 3.14) measured in the hori-	
	zontal plane at hub height for two different yaw angles ($\gamma = 0^{\circ}$, and 30°) at $\lambda = \lambda_o$.	
	Contours are non-dimensionalized with \bar{u}_h^2 and d . Black dots represent the	
	locus of the maximum velocity deficit in the measured plane, and overlapped	26
2.15	locations of PIV planes are indicated by vertical dashed lines	36
3.13	Contours of the terms of the y-RANS equation (Eq. 3.14) measured in a yz plane of $x/d = 6$ for two different year angles ($x = 0^\circ$ and 30°) at $1 = 1$. Contours are	
	at $x/d = 6$ for two different yaw angles ($\gamma = 0^{\circ}$, and 30°) at $\lambda = \lambda_o$. Contours are non-dimensionalized with \bar{u}_h^2 and d . Black circles indicate the frontal area of	
	the wind turbine. The vector field represents the in-plane velocity components.	36
2 16	The self-similar lateral profiles of (a) velocity deficit, and (b) wake skew angle at	30
5.10	different downwind positions in the wake of a turbine with $\gamma = 30^{\circ}$ and $\lambda = \lambda_o$.	40
2 17		40
3.17	Variation of the normalized lateral wake width σ_y/d for $\lambda = \lambda_o$: $\gamma = 0^\circ$ (<i>plus</i>), $\gamma = 10^\circ$ (<i>circle</i>), $\gamma = 20^\circ$ (<i>asterisk</i>), $\gamma = 30^\circ$ (<i>square</i>). Fitted lines with the slope of	
	$\gamma = 10^{\circ}$ (case), $\gamma = 20^{\circ}$ (asierisk), $\gamma = 30^{\circ}$ (square). Fitted lines with the slope of 0.022 are shown by blue lines	41
3 18	Schematic of the wake of a yawed turbine.	44
	Variation of the maximum normalized wake velocity deficit in the horizontal	77
3.13	plane at hub height for different yaw angles shown by black lines. <i>Solid lines</i> and	
	dashed lines correspond to $\lambda = \lambda_0$ and λ_f , respectively. Horizontal and vertical	
	blue lines represent the values of u_0 and x_0 for each case, respectively	46
3 20	(a) The value of the normalised lateral wake width at $x = x_0$, σ_{y_0}/d , for different	
0.20	yaw angles. The light gray bars show the values predicted by Eq. 3.42, and the	
	black ones show the experimental data. (b) The prediction of the normalized	
	potential core length x_0/d compared with the experimental data for different	
	yaw angles and tip-speed ratios.	48
3.21	Lateral profiles of the normalized streamwise velocity \bar{u}/\bar{u}_h in the wake of a	
	turbine with $\gamma = 0^{\circ}$, 10° and 20° at $\lambda = \lambda_o$: wind tunnel measurements (<i>open</i>	
	circle), and new proposed model (blue solid line). Red dots show the wake center	
	position predicted by the proposed model. Horizontal dashed lines indicate the	
	location of the side tips of the turbine. For each downwind location, $\bar{u}/\bar{u}_h=1$ on	
	the vertical thick black line. The width of grid squares corresponds to 15% of \bar{u}_h .	51
3.22	Variation of δ_∞/d as a function of the incoming streamwise turbulence intensity	
	$I = \sqrt{\overline{u'^2}}/\bar{u}_h$ for different values of thrust coefficient C_T . The yaw angle γ is	
	assumed to be 20°	52

4.1	Schematic figure of the different wind tunnel measurements performed in the current study.	62
4.2	Characteristics of the incoming boundary layer: normalized mean velocity (left), turbulence intensity (right). The $\mathit{horizontal-dashed\ lines}$ represent the turbine axis	63
4.3	(a) Normalized mean streamwise velocity profile of the incoming boundary layer in a semi-logarithmic scale. The dashed line shows the fitted logarithmic profile. (b) Normalized streamwise velocity spectra $(E_u(z)u_*^{-2}z^{-1})$ versus k_xz at different heights.	63
4.4	Turbine performance versus tip-speed ratio (thrust coefficient C_T ($left$), and power coefficient C_p ($right$)) for different yaw angles: $\gamma = 0^\circ(circle)$, $\gamma = 10^\circ(diamond)$, $\gamma = 20^\circ(square)$, and $\gamma = 30^\circ(triangle)$. For red-coloured points, PIV measurements were performed	65
4.5	(a) Variation of $C_T(\lambda)/C_T^{\gamma=0}(\lambda)$ and $C_p(\lambda)/C_p^{\gamma=0}(\lambda)$ for different tip-speed ratios versus $\cos \gamma$ in a semi-logarithmic scale. <i>Dashed, dotted</i> and <i>solid</i> lines represent $\cos^{1.5} \gamma$, $\cos^2 \gamma$ and $\cos^3 \gamma$ curves, respectively. (b) Variation of the angle between the net thrust force T and the rotor axis (β°) versus tip-speed ratio λ for different yaw angles	66
4.6	(a) Vectors of mean normal and tangential velocities induced by the turbine with $\gamma=0^\circ$ and $\lambda=\lambda_o$ in the upwind region. The background shows contours of the normalized mean streamwise velocity \bar{u}/\bar{u}_h . While lines are iso-velocity contours, and dashed lines represent the side tips of the rotor. (b) Variation of the mean normalized streamwise velocity in the upwind region along the rotor axis	67
4.7	(a) Vectors of mean normal and tangential velocities induced by the turbine with $\gamma=30^\circ$ and $\lambda=\lambda_o$ in the upwind region. The background shows contours of the normalized mean streamwise velocity \bar{u}/\bar{u}_h . While lines are iso-velocity contours, and dashed lines represent the side tips of the rotor. (b) Profiles of the normal induction factor a for different upwind positions. The shaded area indicates the frontal area of the nacelle.	68
4.8	Contour plots of the mean normalized streamwise velocity \bar{u}/\bar{u}_h in the near-wake region for different turbine operating conditions.	69
4.9	Contours of the instantaneous out-of-plane vorticity ω_z , non-dimensionalized with \bar{u}_h and d , for different turbine operating conditions.	70
4.10	Contours of the phase-averaged out-of-plane vorticity $\bar{\omega}_z$, non-dimensionalized with \bar{u}_h and d , for three different operating conditions	72
4.11	Profiles of the normalized mean streamwise velocity \bar{u}/\bar{u}_h downwind of a non-yawed turbine at different downwind locations for different tip-speed ratios: optimal tip-speed ratio λ_o (solid lines), and free-rotating tip-speed ratio λ_f (dashed lines). For each downwind location, $\bar{u}=\bar{u}_h$ on the vertical thick blue lines. The width of grid squares corresponds to 17% of \bar{u}_h	73
4.12	Contours of the normalized lateral turbulent momentum flux $\overline{u'v'}/\bar{u}_h^2$ downwind of the turbine with zero yaw angle for two different tip-speed ratios: the optimal tip-speed	. 3
	ratio λ_o (<i>left</i>), and the free rotating tip-speed ratio λ_f (<i>right</i>)	74

4.13	(a) Non-dimensionalized pre-multiplied spectrum $k_x\Phi_{uu}/u_*^2$ of the incoming streamwise velocity at hub height versus the streamwise wavelength λ_x . (b) Auto-correlation of the streamwise velocity fluctuation ρ_{uu} for the incoming boundary layer at different heights	76
4.14	Contours of the two-point correlation of the streamwise velocity fluctuation R_{uu} in the upwind region of the turbine with $\gamma=0^\circ$ and $\lambda=\lambda_o$ for two different arbitrarily-chosen reference positions: $x_{ref}=-0.7d$ and $y_{ref}=0$ ($left$), and $x_{ref}=-0.7d$ and $y_{ref}=-0.5$ ($right$)	77
4.15	Contours of the two-point correlation of the streamwise velocity fluctuation R_{uu} for different downwind locations. The turbine operates at $\gamma=0^\circ$ and $\lambda=\lambda_o$. For each contour plot, the respective reference position (x_{ref},y_{ref}) is indicated by a <i>white plus</i> sign	77
4.16	Contours of the instantaneous streamwise wake velocity u (<i>left</i>) and its fluctuation component $u' = u - \bar{u}$ (<i>right</i>), both normalized with \bar{u}_h . Solid black lines represent the	
4 17	instantaneous wake center position calculated by Eq. 4.6	78 79
	Schematic figure of the wake meandering at two different time instances Standard deviation of the wake-center position normalized with the rotor diameter d	13
4.10	for different turbine operating conditions	80
4.19	Vectors of streamwise and spanwise components of the first six POD modes ϕ_u , ϕ_v for three different FOVs in the wake of the turbine operating at $\gamma=0^\circ$ and $\lambda=\lambda_o$. The background shows the contour plot of the streamwise component of POD modes ϕ_u . The turbine operates at $\gamma=0^\circ$ and $\lambda=\lambda_o$	82
4.20	(a) Energy of the first 100 POD modes for three different FOVs of <i>PIV-setup II</i> in a semi-logarithmic scale. (b) Sum of the energy for a given number of successive POD modes.	83
4.21	The approximated instantaneous velocity field reconstructed by the first: 3 POD modes (<i>left</i>), 10 POD modes (<i>middle</i>) and 100 POD modes (<i>right</i>). The original instantaneous flow field is shown in Fig. 4.16.	84
5.1	Airfoil geometry: the cambered plate with very thin edges (<i>blue color</i>), and the cambered plate with constant thickness modified due to construction limits (<i>red color</i>)	92
5.2	(a) The velocity triangle for a rotor blade element. (b) The most achievable power coefficient $C_{P,max}$ as a function of the design tip-speed ratio for $C_L/C_D=13$. Dashed line represents the Betz limit	92
5.3	Twist and chord distributions for the blade of the miniature turbine shown by <i>blue circles</i> . The ones suggested by the Glauert design method are shown with black lines.	93
5.4	Variation of the thrust coefficient C_T of the miniature turbine with the tip-speed ratio λ at different free-stream incoming velocities	94

5.5	Variation of the thrust coefficient C_T with the normal induction factor a for an annulus at two different design tip-speed ratios ($\lambda_{design} = 4$ and 6). The airfoil profile is NACA0012, operating at $Re_c = 1.76 \times 10^6$. The black lines represent the relationship based on the momentum approach, while the colored lines show it from the blade-element approach. For each tip-speed ratio, the operating condition is indicated by hollow white circles	95
5.6	Energy conversion in a miniature wind turbine	97
5.7	Equivalent electrical circuit of a permanent magnet DC generator	98
5.8	Schematic of the setup for direct measurements of the shaft torque Q_{sh} of DC generators	99
5.9	Measured values of $(Q_{sh}-KI)$ versus the rotational velocity Ω for different electrical currents and DC machines in both <i>motor</i> and <i>generation</i> modes. The black lines show the prediction of the friction torque Q_f based on Eq. 5.11 and using the manufacturer-provided data	101
5.10	Variation of the power coefficient C_P with the tip-speed ratio λ for the miniature turbine with two different DC machines under the same inflow conditions. For each DC machine, the turbine power is calculated with different methods. The free-stream incoming velocity is equal to 8 ms^{-1}	103
5.11	Variation of the thrust coefficient C_P of the miniature turbine with the tip-speed ratio λ at different free-stream incoming velocities	104
5.12	(a) Schematic figure of the miniature wind turbine placed in the turbulent boundary layer. (b) Variation of C_T and C_P with the tip-speed ratio λ for the miniature turbine placed in the boundary layer with $\bar{u}_h = 5 \text{ ms}^{-1}$	105
5.13	Spectral density of the incoming velocity at hub height u_h , the thrust force T and $(1/2)\rho u_h^2 AC_T$ for two different tip-speed ratios. The rotational frequency of the rotor f_T and its harmonics are shown by dashed lines. One half of the rotor rotational frequency $0.5f_T$ and its harmonics are shown by dotted lines	105
5.14	Contours of the normalized velocity deficit $\Delta \bar{u}_h/\bar{u}_h$ in yz planes at different downwind locations for the miniature turbine operating at $\lambda=\lambda_o$. The vector field represents the in-plane velocity components. The black circles show the frontal area of the wind turbine	107
5.15	Contours of the normalized vertical momentum turbulent flux $\overline{u'w'}/\bar{u}_h^2$ in yz planes at different downwind locations for the miniature turbine operating at $\lambda = \lambda_o$. The vector field represents the in-plane velocity components. The black circles show the frontal area of the wind turbine	107
5.16	Contours of the normalized lateral momentum turbulent flux $\overline{u'v'}/\bar{u}_h^2$ in yz planes at different downwind locations for the miniature turbine operating at $\lambda = \lambda_o$. The vector field represents the in-plane velocity components. The black circles show the frontal area of the wind turbine	100
	CHOICS SHOW THE HORITAL AREA OF THE WIHL LUIDING	108

5.17	Contours of the added streamwise turbulence intensity $I_{u,add}$ in yz planes at	
	different downwind locations for the miniature turbine operating at $\lambda = \lambda_o$. The	
	vector field represents the in-plane velocity components. The black circles show	
	the frontal area of the wind turbine	109
5.18	Lateral (top) and vertical (bottom) profiles of the normalized velocity deficit	
	through the hub level at different downwind locations. Blue dashed lines repre-	
	sent the rotor axis	110
5.19	Lateral profiles of the normalized vertical velocity (top) and vertical profiles of	
	the normalized spanwise velocity (<i>bottom</i>) through the hub level at different	
	downwind locations. Blue dashed lines represent the rotor axis	111
5.20	Lateral (<i>top</i>) and vertical (<i>bottom</i>) profiles of the added streamwise turbulence	
	intensity through the hub level at different downwind locations. Blue dashed	
	lines represent the rotor axis	111
5.21	Lateral profiles of the normalized lateral momentum turbulent flux (<i>top</i>) and	
	vertical profiles of the normalized vertical momentum turbulent flux (<i>bottom</i>)	
	through the hub level at different downwind locations. Blue dashed lines repre-	
	sent the rotor axis.	112

List of Tables

2.1	Different experimental and LES case studies used to validate the new proposed			
	model	10		
4.1	Key characteristics of the incoming boundary layer as well as the wind turbine dimensions.	64		
5.1	Airfoil design conditions	92		
5.2	Manufacturer-provided data of the DC machines studied in this paper	99		

1 Introduction

Wind turbines have been used to harness wind energy since the advent of Persian vertical-axis turbines in the tenth century (Spera, 1994). Since then, wind turbines have been continuously evolving until three-bladed horizontal-axis turbines (HAWTs) have become the most popular types of wind turbines nowadays (Sørensen, 2015). During the last four decades, extensive research has been performed to study the performance of HAWTs and the airflow disturbed by their presence (see the reviews of Crespo et al., 1999; Vermeer et al., 2003; Sørensen, 2011). Nevertheless, the interaction of wind turbines with the atmospheric boundary layer (ABL) flow remains an open issue and it is far from being fully understood. Wind turbines are continuously subject to changes in wind magnitude and direction due to their interaction with the highly turbulent ABL flow. As a consequence, wind turbines operate in different conditions (e.g., yaw angle and tip-speed ratio) during their lifespan. The study of the ABL interaction with wind turbines can therefore help us better predict and optimize the performance of wind turbines under different operating conditions. Moreover, given the fast growth in the number and size of installed wind farms, the cumulative effect of turbine wakes in wind farms is another important open issue in the wind energy community. As many wind turbines in wind farms have to operate in the wakes of upwind turbines, they are exposed to incoming wind velocities that are smaller than those under unperturbed conditions. As a result, turbine wakes and their cumulative effect are the main cause of power losses in wind farms (Barthelmie et al., 2009). This calls for a better understanding and prediction of turbine wakes under different operating conditions, which can ultimately lead us to develop more effective strategies for maximizing wind energy production in wind farms. For instance, yaw angle control is one of the strategies that can be used to alleviate the cumulative effect of turbine wakes by deflecting them away from downwind turbines (Dahlberg and Medici, 2003). In order to assess the viability of these strategies, however, more systematic studies on turbine wakes should be first performed.

This thesis aims at addressing the above-mentioned open issues by means of wind tunnel experiments and analytical studies. Wind tunnel experiments can be used as a versatile tool to study the performance of wind turbines and their wakes under fully controlled conditions.

Chapter 1. Introduction

Extensive wind tunnel studies have been recently performed in the wind energy community (e.g., Medici and Alfredsson, 2006; Chamorro and Porté-Agel, 2009; Zhang et al., 2012). Generally speaking, these studies are either limited to uniform inflow conditions or, in the case of boundary-layer inflow conditions, only one given turbine operating condition. We therefore perform detailed wind tunnel measurements in this thesis to elucidate the interaction of the ABL flow with a wind turbine under different operating conditions (e.g., different tip-speed ratios and yaw angles). Prior wind tunnel studies also used miniature wind turbines that usually suffer from poor performance with respect to their large-scale counterparts in the field. To develop a new generation of miniature turbines with more realistic characteristics, a turbine suitable for wind tunnel experiments is designed and fully analyzed in this thesis.

In spite of the fast growth of numerical and experimental techniques, simple analytical models with low computational costs are still useful tools to predict the flow within wind farms under the wide variety of different conditions imposed by the unsteadiness of the ABL flow. Different simple models have been proposed in the literature to predict turbine wakes (e.g., Jensen, 1983; Frandsen et al., 2006). However, they are usually based on unrealistic assumptions such as considering a top-hat shape for the velocity deficit. Moreover, they are limited to turbine wakes in non-yawed conditions, and hence they cannot be used to assess the suitability of yaw-angle control for wind farm power optimization. Theoretical studies are performed in this thesis with the aim of developing simple analytical wake models to predict the velocity distribution in turbine wakes under different operating conditions.

The structure of the thesis is as follows. In **chapter 2**, a new simple analytical wake model is proposed and validated to predict the velocity distribution in the wake of a non-yawed turbine. **Chapter 3** concerns wind tunnel measurements performed to study the wake of a yawed turbine. A new analytical model is also proposed to predict the wake deflection and velocity distribution in the wake of a yawed turbine. **Chapter 4** presents the wind tunnel study of the turbine interaction with the ABL flow for different tip-speed ratios and yaw angles. In addition to the wind turbine performance, the flow fields in the upwind, near-wake and far-wake regions are studied. **Chapter 5** provides the design and performance analysis of a new miniature turbine. It also presents a new setup developed to measure the extracted power of wind turbines. Finally, overall summary and future research perspectives are presented in **Chapter 6**.

2 A new analytical model for windturbine wakes¹

Abstract

A new analytical wake model is proposed and validated to predict the wind velocity distribution downwind of a wind turbine. The model is derived by applying conservation of mass and momentum and assuming a Gaussian distribution for the velocity deficit in the wake. This simple model only requires one parameter to determine the velocity distribution in the wake. The results are compared to high-resolution wind-tunnel measurements and large-eddy simulation (LES) data of miniature wind-turbine wakes, as well as LES data of real-scale wind-turbine wakes. In general, it is found that the velocity deficit in the wake predicted by the proposed analytical model is in good agreement with the experimental and LES data. The results also show that the new model predicts the power extracted by downwind wind turbines more accurately than other common analytical models, some of which are based on less accurate assumptions like considering a top-hat shape for the velocity deficit.

2.1 Introduction

Due to the fast growth in the number and size of installed wind farms around the world, wind-turbine wakes have become important topics of study. As many wind turbines in wind farms have to operate in the wakes of upwind turbines, they are exposed to incoming wind velocities that are smaller than those under unperturbed (unwaked) conditions. As a result, turbine wakes are responsible for important power losses in wind farms (Vermeer et al., 2003; Barthelmie et al., 2009; Porté-Agel et al., 2013). Extensive analytical, numerical and experimental efforts have been carried out to better understand and predict turbine wake flows. Although numerical and experimental techniques have become increasingly sophisticated and accurate in recent years, simple analytical models are still useful tools to predict wind-turbine wake flows and their effect on power production. They are widely used due to their simplicity

¹The contents of this chapter are published in: M. Bastankhah and F. Porté-Agel. A new analytical model for wind-turbine wakes. *Renewable Energy*, 70:116–123, 2014.

and low computational cost (Crespo et al., 1999). Various analytical investigations have been conducted on wind-turbine wakes (e.g., Katić et al., 1986; Kiranoudis and Maroulis, 1997; Frandsen, 1992). One of the pioneering analytical wake models is the one proposed by Jensen (1983), which assumes a top-hat shape for the velocity deficit in the wake (see Fig. 2.1(a)) and states:

$$\frac{\Delta U}{U_{\infty}} = \left(1 - \sqrt{1 - C_T}\right) / \left(1 + \frac{2k_{wake}x}{d_0}\right)^2,\tag{2.1}$$

where C_T is the thrust coefficient of the turbine, k_{wake} the rate of wake expansion, d_0 the diameter of the wind turbine and x the downwind distance. $\Delta U/U_{\infty}$ is the normalized velocity deficit, which is defined as:

$$\frac{\Delta U}{U_{\infty}} = \frac{U_{\infty} - U_{w}}{U_{\infty}},\tag{2.2}$$

where U_{∞} is the incoming wind velocity and U_w the wake velocity in the streamwise direction. Jensen (1983) considered a constant value for the rate of wake expansion ($k_{wake} = 0.1$). However, the suggested values for k_{wake} in the literature are 0.075 (Barthelmie et al., 2005) for on-shore cases and 0.04 (Barthelmie and Jensen, 2010; Cleve et al., 2009) or 0.05 (Barthelmie et al., 2005, 2007) for off-shore ones. Katić et al. (1986) also used the top-hat model proposed by Jensen (1983). They claimed that the top-hat model gives an estimate of the energy content rather than describing the velocity field accurately, and hence they adopted a top-hat shape for the velocity deficit in the wake because of its simplicity and low computational cost. Nevertheless, note that the energy available in the wind varies as the cube of the wind speed (Burton et al., 1995) and, therefore, an improper evaluation of velocity field in a wind farm can lead to large errors in the prediction of the energy output. This will be discussed in detail in Sect. 2.3.

Eq. 2.1 has been extensively used in the literature (e.g., Marmidis et al., 2008) and commercial softwares such as WAsP (Barthelmie et al., 2005), WindPRO (Thøgersen, 2005), WindSim (Crastoa et al., 2012), WindFarmer (Gar, 2009) and OpenWind (AWS, 2010). However, there are two important limitations of this simple model that should be pointed out: (a) The assumption of the top-hat distribution of the velocity deficit is not realistic (Chamorro and Porté-Agel, 2010; Gaumond et al., 2013). (b) Even though Jensen (1983) and Katić et al. (1986) claimed using momentum conservation to derive Eq. 2.1, it will be shown in the following that in reality they only used mass conservation to derive their model.

Jensen (1983) considered a control volume immediately downwind of the turbine. Fig. 2.2.a shows a schematic of this control volume with the left cross-sectional area (side 1) equal to the area swept by the wind-turbine blades, A_0 , and the right area (side 3) equal to the cross-sectional area of the wake, A_w . The incoming flow also enters into the control volume through the lateral surface (side 2) with the velocity of U_∞ . According to mass conservation:

$$\dot{m}_2 = \rho U_w A_w - \rho U_a A_0,\tag{2.3}$$

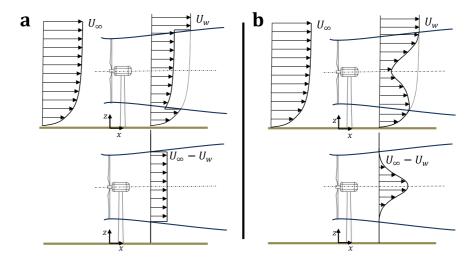


Figure 2.1 – Schematic of the vertical profiles of the mean velocity (*top*) and velocity deficit (*bottom*) downwind of a wind turbine obtained by assuming: (a) a top-hat and (b) a Gaussian distribution for the velocity deficit in the wake.

where \dot{m}_2 is the mass flow rate through the lateral surface, ρ the density of the air and U_a the wind velocity just behind the wind turbine (see Fig. 2.2(a)). Note that if \dot{m}_2 is replaced with $\rho U_{\infty}(A_w-A_0)$ in the mass conservation equation (Eq. 2.3), without considering momentum conservation, the basic equation that Jensen (1983) used to establish his model will be obtained. It implies, therefore, that this model can be derived by considering mass conservation alone without any consideration of the balance of momentum.

Later, Frandsen et al. (2006) applied mass and momentum conservation to a control volume around the turbine (Fig. 2.2(b)) and proposed the following expression for the velocity deficit in the wake:

$$\frac{\Delta U}{U_{\infty}} = \frac{1}{2} \left(1 - \sqrt{1 - 2\frac{A_0}{A_w} C_T} \right),\tag{2.4}$$

where $A_w(x=0)=A_a$, and A_a is the cross-sectional area of the wake just after the initial wake expansion. In other words, they assumed that the distance downwind of a rotor that the flow requires to reach the pressure of the free flow is negligible, so they considered A_a as the wake cross-sectional area at x=0. It is, however, difficult to identify exactly this distance in reality. Crespo et al. (1999) stated that the length of this region is in the order of one rotor diameter. Even though this assumption is crude, it ensures a solution for all C_T values between 0 and 1 (Frandsen et al., 2006). According to the actuator disk concept (Burton et al., 1995), A_a is given by:

$$A_a = \beta A_0, \tag{2.5}$$

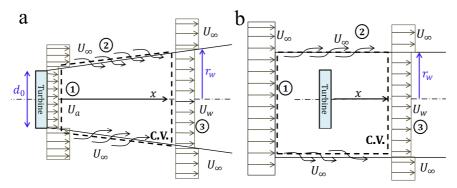


Figure 2.2 – Schematic of the two control volumes: (a) downwind of the wind turbine, and (b) around the wind turbine.

where β is a function of C_T and can be expressed as:

$$\beta = \frac{1}{2} \frac{1 + \sqrt{1 - C_T}}{\sqrt{1 - C_T}}. (2.6)$$

They also used an asymptotic solution for an infinite row of two-dimensional obstacles to write the wake diameter, d_w , as:

$$d_w = (\beta + \alpha x/d_0)^{1/2} d_0, \tag{2.7}$$

where the expansion factor α is of order $10k_{wake}$ (Frandsen et al., 2006). While Frandsen et al. (2006) employed the mass and momentum equations, their model still assumed a top-hat shape for the velocity deficit in the wake.

Wakes of bluff bodies in free stream flows have been extensively studied in classical theories of shear flows (e.g., Tennekes and Lumley, 1972; Johansson et al., 2003; Dufresne and Wosnik, 2013a). In these studies, the self-similar Gaussian profile of the velocity deficit is found in the far-wake regions. For wind-turbine wakes in turbulent boundary layers, even though the velocity distribution does not show axisymmetric behavior (Chamorro and Porté-Agel, 2009), the velocity deficit in the wake has an approximately Gaussian axisymmetric shape after some downwind distances (Chamorro and Porté-Agel, 2009; Troldborg et al., 2007) (Fig. 2.1(b)). This Gaussian shape of the velocity deficit in turbine wakes has been observed by wind-tunnel measurements (e.g., Chamorro and Porté-Agel, 2009; Medici and Alfredsson, 2006; Markfort et al., 2012; Zhang et al., 2013; Porté-Agel et al., 2011), numerical simulations (e.g., Wu and Porté-Agel, 2012) and data of operating wind farms (e.g., Gaumond et al., 2013; Nygaard et al., 2013). Therefore, the Gaussian distribution is appropriate to describe the velocity deficit in the far wake regions, regardless of the incoming wind conditions.

The intention of the work described in this paper is to propose and validate a simple and efficient analytical model for the prediction of the velocity downwind of a wind turbine. For this purpose, a Gaussian distribution is considered for velocity deficit profiles in the wake, and

momentum and mass conservation are applied to find the velocity distribution downwind of the wind turbine. The results are tested against the wind-tunnel measurements (Chamorro and Porté-Agel, 2010) and the LES data (Wu and Porté-Agel, 2011) for the wake of a miniature wind turbine, as well as the LES data (Wu and Porté-Agel, 2012) of a real-scale wind turbine under four different atmospheric turbulence conditions.

In Sect. 2.2, the wake model is derived. The results are then presented and compared with wind-tunnel measurements and LES data in Sect. 2.3. The summary and future research are presented in Sect. 2.4.

2.2 Wake model

If we neglect viscous and pressure terms in the momentum equation, the following equation can be obtained for the wake by applying mass and momentum conservation (Tennekes and Lumley, 1972)):

$$\rho \int U_w (U_\infty - U_w) dA = T, \tag{2.8}$$

where *T* is the total force over the wind turbine. *T* can be determined by (Burton et al., 1995):

$$T = \frac{1}{2} C_T \rho A_0 U_\infty^2. \tag{2.9}$$

Next, the self-similarity in the wake describes the normalised velocity deficit as (Pope, 2000):

$$\frac{\Delta U}{U_{\infty}} = C(x) f(r/\delta(x)), \qquad (2.10)$$

where C(x) represents the maximum normalized velocity deficit at each downwind location which occurs at the center of the wake; r is the radial distance from the center of the wake and $\delta(x)$ the characteristic wake width at each x. As explained in the previous section, the velocity deficit in the turbine wake, regardless of incoming conditions, is assumed to have a Gaussian shape. Thus, Eq. 2.10 can be written as:

$$\frac{\Delta U}{U_{\infty}} = C(x)e^{-\frac{r^2}{2\sigma^2}},\tag{2.11}$$

where σ is the standard deviation of the Gaussian-like velocity deficit profiles at each x. Note that σ is not associated with *turbulent velocity fluctuations* in this paper. According to Eq. 2.11, the wake velocity is given by:

$$U_w = U_\infty \left(1 - C(x)e^{-\frac{r^2}{2\sigma^2}} \right). \tag{2.12}$$

Inserting Eqs. 2.9 and 2.12 into Eq. 2.8 and integrating from 0 to ∞ yield:

$$8\left(\frac{\sigma}{d_0}\right)^2 C(x)^2 - 16\left(\frac{\sigma}{d_0}\right)^2 C(x) + C_T = 0.$$
 (2.13)

By solving Eq. 2.13, one can obtain two values for C(x) while only one of them, which predicts the smaller value for the velocity deficit at larger downwind distances, is physically acceptable:

$$C(x) = 1 - \sqrt{1 - \frac{C_T}{8(\sigma/d_0)^2}}. (2.14)$$

If we assume a linear expansion for the wake region like the one considered by Jensen (1983), σ/d_0 can be written as:

$$\frac{\sigma}{d_0} = k^* \frac{x}{d_0} + \varepsilon,\tag{2.15}$$

where $k^* = \partial \sigma/\partial x$ is the growth rate and ε is equivalent to the value of σ/d_0 as x approaches zero. Note that $k^* = \partial \sigma/\partial x$ is different from $k_{wake} = \partial r_w/\partial x$ used by Jensen (1983). Inserting Eqs. 2.14 and 2.15 into Eq. 2.11 and rearranging give:

$$\frac{\Delta U}{U_{\infty}} = \left(1 - \sqrt{1 - \frac{C_T}{8(k^* x/d_0 + \varepsilon)^2}}\right) \times exp\left(-\frac{1}{2(k^* x/d_0 + \varepsilon)^2} \left\{ \left(\frac{z - z_h}{d_0}\right)^2 + \left(\frac{y}{d_0}\right)^2 \right\} \right), \tag{2.16}$$

where y and z are spanwise and vertical coordinates, respectively, and z_h is the hub height. Eq. 2.16 gives the normalized velocity deficit in the wake as a function of normalized coordinates $(x/d_0, y/d_0 \text{ and } z/d_0)$, C_T and k^* . In order to use the above equation, the value of ε should be determined in advance.

Next, the value of ε will be determined by equating the total mass flow deficit rate at x=0 obtained by Frandsen et al. (2006) and the one obtained by the new proposed model (Eq. 2.16). The velocity deficit just behind the turbine is usually assumed to have a uniform distribution and it changes to a Gaussian shape further downstream. Thus, at x=0, Eq. 2.16 is not likely to predict the velocity profile accurately. However, the total mass flow deficit rate at x=0 predicted by this equation should be the same as the one obtained by Frandsen et al. (2006) since both of these models are derived by applying the same governing equations. According to Eq. 2.4, the total mass flow deficit rate at x=0 obtained by Frandsen model is:

$$\int \frac{\Delta U}{U_{\infty}} dA = \frac{\pi}{8} d_0^2 \beta \left(1 - \sqrt{1 - \frac{2}{\beta} C_T} \right), \tag{2.17}$$

where β is defined in Eq. 2.6. On the other hand, from Eq. 2.16, the total mass flow deficit rate

at x = 0 based on the new proposed model is given by:

$$\int \frac{\Delta U}{U_{\infty}} dA = \int_{0}^{+\infty} \left(1 - \sqrt{1 - \frac{C_T}{8\varepsilon^2}} \right) exp\left(\frac{-r^2}{2\varepsilon^2 d_0^2} \right) 2\pi r dr$$

$$= 2\pi \varepsilon^2 d_0^2 \left(1 - \sqrt{1 - \frac{C_T}{8\varepsilon^2}} \right). \tag{2.18}$$

By equating Eqs. 2.17 and 2.18, it can be concluded that:

$$\varepsilon = 0.25\sqrt{\beta}.\tag{2.19}$$

2.3 Results and discussion

In this section, we present the results obtained by the new proposed model and compare them with 5 different LES and experimental case studies (see Table 2.1). Case (1) in Table 2.1 corresponds to the wind-tunnel measurements reported by Chamorro and Porté-Agel (2010) and the LES performed by Wu and Porté-Agel (2011) to investigate the wake of a miniature wind turbine in a turbulent boundary layer flow. Later, Wu and Porté-Agel (2012) also used LES to study the effect of atmospheric turbulence on wakes of real-scale wind turbines. To this end, they simulated the wake of a Vestas V80-2MW wind turbine with four different aerodynamic surface roughness lengths (Cases 2-5 in Table 2.1). Note that I_0 denotes the ambient streamwise turbulence intensity in Table 2.1, and z_0 is the aerodynamic roughness of the terrain. These roughness lengths shown for Cases (2-5) in Table 2.1 are representative of different land surface types, including very rough terrain ($z_0 = 0.5m$), farmlands ($z_0 = 0.005m$), grasslands ($z_0 = 0.005m$), and snow-covered flats ($z_0 = 0.00005m$) (Wu and Porté-Agel, 2012).

Figure 2.3 shows the self-similar velocity-deficit profiles $f = \Delta U/\Delta U_{max}$ for wind-tunnel measurements (Chamorro and Porté-Agel, 2010) (Case 1) and the LES data (Wu and Porté-Agel, 2012) (Cases 2-5) at different downwind distances. The wake's half-width $r_{1/2}(x)$, defined at each x as

$$\frac{\Delta U(r = r_{1/2})}{U_{\infty}} = \frac{1}{2} \frac{\Delta U_{max}}{U_{\infty}} = \frac{1}{2} C(x), \tag{2.20}$$

is used as the characteristic wake width in this figure. The figure shows that the profiles of $f = \Delta U/\Delta U_{max}$ plotted against $r/r_{1/2}$ approximately collapse onto a single Gaussian curve except at the edge of the wake. It means that the velocity deficit profile can be assumed to have a self-similar Gaussian shape after some downwind distance $(x/d_0 \gtrsim 3)$.

In Fig. 2.4, the normalized standard deviation of the Gaussian curves fitted to the velocity deficit profiles in the wakes is plotted as a function of normalized downwind distance for the different cases. It shows that the wake expands approximately linearly in the range of $2 < x/d_0 < 15$ for the different cases, although classical theories of shear flows predict the

Cases	$d_0(m)$	$z_h(m)$	$U_{hub}(m/s)$	C_T	$z_0(m)$	$I_0(z=z_h)$
Case 1	0.15	0.125	2.2	0.42	0.00003	0.070
Case 2	80	70	9	8.0	0.5	0.134
Case 3	80	70	9	8.0	0.05	0.094
Case 4	80	70	9	8.0	0.005	0.069
Case 5	80	70	9	8.0	0.00005	0.048

Table 2.1 – Different experimental and LES case studies used to validate the new proposed model.

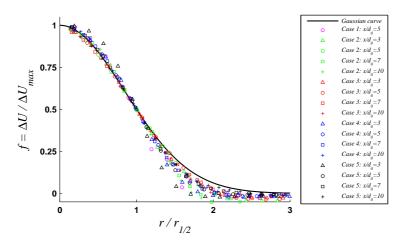


Figure 2.3 – The self-similar velocity deficit profiles of the wind-tunnel measurements (Chamorro and Porté-Agel, 2010) (Case 1) and the LES data (Wu and Porté-Agel, 2012) (Cases 2-5) at different downwind distances.

wake width varies as $x^{1/3}$ (Tennekes and Lumley, 1972). This discrepancy might be due to the following reasons: (1) To derive this power law dependence of wake width on x in classical studies, $\Delta U/U_{\infty}$ at the wake center is assumed to tend to zero (lower than 0.1) (Pope, 2000) whereas it is not a good assumption in our region of interest $(x/d_0 \lesssim 20)$ for the turbine wake (see values of $\Delta U/U_{\infty}$ in Fig. 2.5). (2) More importantly, in classical studies (e.g., Tennekes and Lumley, 1972), the effect of ambient turbulence intensity on the wake growth is not considered (Crespo et al., 1999). In turbulent boundary layers, the wake is, however, known to recover faster than in non-turbulent flows since both ambient turbulence and shear-generated turbulence contribute to the growth rate in this case (e.g., Wu and Porté-Agel, 2012). Thus, it seems reasonable to observe a faster wake recovery compared to that predicted by classical studies.

The figure also shows that the wakes recover faster with increasing the ambient turbulence intensity (compare Cases 2-5). It is due to the fact that higher incoming turbulence enhances mixing processes, which result in faster wake recovery. However, the wake recovery is approximately the same for Cases (4) and (5) with different ambient turbulence intensities. One

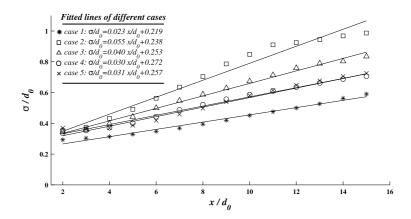


Figure 2.4 – Normalized standard deviation of the velocity deficit profiles: case 1 (*asterisk*), case 2 (*square*), case 3 (*triangle*), case 4 (*circle*) and case 5 (*crosses*). Fitted lines are represented by solid lines.

possible explanation is that the ratio of the ambient turbulence intensity to the turbulence intensity added by turbines is small in Cases (4) and (5). Thus, the wake recovery in these cases is likely to be more influenced by the turbulence added by the turbine than the ambient turbulence. Now, let us compare Case (4) with the higher value of C_T to Case (1) with the lower value of C_T but approximately the same value of I_0 . Figure 2.4 shows that the wake width in Case (4) is larger than Case (1). However, it seems that this difference is mostly created at smaller downwind distances, and it remains approximately constant further downstream (x/d > 6). It is worth mentioning that the above discussions about the wake growth behavior are based on the experimental and numerical results presented in this research. In fact, we believe that deep understanding of the turbine wake growth under different conditions suffers from the lack of fundamental studies, and thus, we aim to extensively study this in our future research.

The value of ε for the different cases can also be estimated by extrapolating the fitted lines in Fig. 2.4. The comparison between the values of ε obtained by extrapolating the LES data and the ones derived analytically (Eq. 2.19) reveals that Eq. 2.19 is able to predict the trend for the different cases in such a way that the turbines with higher values of C_T (Cases 2-5) generally have larger values of ε compared to the one with lower value of C_T (Case 1). Nonetheless, Eq. 2.19 overestimates the value of ε for all cases. It is probably due to the fact that we equated the total mass flow rate at x=0 obtained by the new proposed model with the one proposed by Frandsen et al. (2006) to derive the value of ε . As discussed in Sect. 2.1, Frandsen et al. (2006) neglected the distance downwind of the turbine that the flow requires to reach the pressure of the free flow and so assumed that $A_w(x=0)=A_a$ where A_a is determined by Eq. 2.5. Hence, in reality the value predicted by Eq. 2.19 corresponds to some small distance downwind of the turbine, instead of immediately behind the turbine. The value of ε should therefore be lower than the one predicted by Eq. 2.19. According to the LES data shown in Fig. 2.4, the below expression with the lower constant coefficient gives a better estimation of the value of ε for

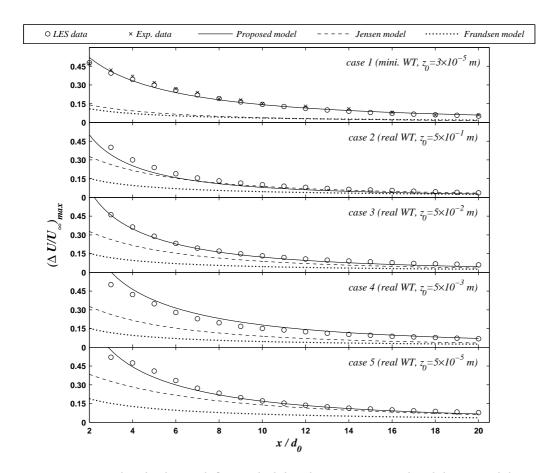


Figure 2.5 – Normalized velocity deficit, at hub height, versus normalized downwind distance in the wake of wind turbines (*Cases 1-5*): Wind-tunnel measurements (*Chamorro and Porté-Agel, 2010*) (*crosses*), LES data (*Wu and Porté-Agel, 2011, 2012*) (*open circle*), new proposed model (*solid line*), the model proposed by Jensen (1983) (*dashed line*) and the model proposed by Frandsen et al. (2006) (*dotted line*).

the different cases:

$$\varepsilon = 0.2\sqrt{\beta}.\tag{2.21}$$

In the following, the results obtained by the new proposed and other analytical models are compared against LES and experimental data for the different cases. For the new proposed model, the value of k^* is found from the LES data of the different cases (see Fig. 2.4), then Eq. 2.16 is used to predict the velocity deficit in the wake for each case. For Jensen model, k_{wake} is set to 0.05 for Case (5) since the surface roughness in this case is on the order of off-shore cases, and $k_{wake} = 0.075$ is used for other cases. Fig. 2.5 shows the change of the normalized velocity deficit, at turbine hub height, as a function of normalized downwind distance for different analytical models, the wind-tunnel measurements performed by Chamorro and Porté-Agel (2010) and the LES data reported by Wu and Porté-Agel (2011) and Wu and Porté-Agel (2012).

The figure shows that the model proposed by Jensen (1983) can predict the maximum velocity deficit reasonably well in some regions (e.g., $x/d_0 > 6$ in Case 2), but this model underestimates the maximum velocity deficit in other regions with respect to the LES (Wu and Porté-Agel, 2011, 2012) and experimental data (Chamorro and Porté-Agel, 2010). This underestimation is more obvious for relatively small downwind distances $(x/d_0 < 8)$. This departure can be attributed to: (a) the assumption of a uniform velocity distribution in the wake which leads to the observed underestimation at the center of the wake (where the maximum velocity deficit is found), and (b) the sole use of mass conservation to derive the model. The model proposed by Frandsen et al. (2006) also underestimates the velocity deficit at turbine hub height. In addition to the top-hat assumption for the velocity deficit, the failure of their model can be attributed to the assumed nonlinear expansion for the wake which is, as described earlier, not in agreement with the LES data at distances $x/d_0 < 20$. On the other hand, the new proposed model is able to predict reasonably well the maximum velocity deficit in the wake of miniature and real-scale wind turbines placed over different land surface types, ranging from a very rough terrain (Case 2) to a smooth one (Case 5). We only need to have a reasonable estimation of the growth rate k^* .

Fig. 2.6 shows contours of the streamwise velocity for Case (1) measured in the wind-tunnel experiment (Chamorro and Porté-Agel, 2010) and predicted by the proposed analytical model on a vertical plane perpendicular to the wind turbine at zero span. It shows that the results obtained with the new proposed model are in acceptable agreement with the wind-tunnel measurements, and the model can thoroughly capture the non-axisymmetric velocity distribution in the wake due to the presence of the turbulent boundary layer.

Vertical profiles of the velocity deficit in Cases (2-5) for the different analytical models and the LES data (Wu and Porté-Agel, 2012) are shown in Fig. 2.7 for chosen downwind locations (x/d = 3,5,7,10). The figure shows that the results obtained from the proposed model for the velocity deficit in the wake of the real-scale turbine are in acceptable agreement with the LES data (Wu and Porté-Agel, 2012) at different heights. It also shows that the top-hat models not only do underestimate the velocity deficit at hub height but also overestimate it near the edge of the wake.

It should be mentioned that the effect of ground on turbine wakes is neglected in this research. The ground can generally have two effects on turbulent wake flows: (a) suppression of turbulent velocity near the ground, and (b) the inviscid potential effect of the ground (Lissaman, 1979). Firstly, since the suppression of turbulence due to the presence of the ground occurs in a region very close to the ground, its effect is assumed to be trivial at the hub-height level. Secondly, the inviscid potential effect can be simulated by imaging techniques. Based on this technique, a symmetrical turbine is considered below the ground, and the velocity deficits of both the real and image turbines are added, so that the drag conservation is satisfied (Crespo et al., 1999; Lissaman, 1979). If this image technique is used to consider the ground effect in Cases (1-5), the normalized velocity deficit differs less than 0.01 at hub height for x/d < 20 with respect to a single turbine wake without ground effect. Thus, it seems that the ground has

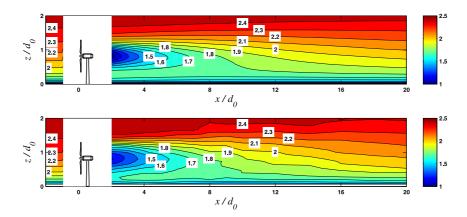


Figure 2.6 – Contours of streamwise velocity (ms^{-1}) in the vertical plane normal to the wind turbine, at zero span *(Case 1)*: New proposed model (top) and wind-tunnel measurements (Chamorro and Porté-Agel, 2010) (bottom).

a weak effect on our region of interest, and it is, therefore, neglected in the present research for sake of simplicity.

Another difference between turbine wakes and purely axisymmetric wakes is that the turbine wake rotates in the opposite direction to that of the blades due to conservation of angular momentum (Manwell et al., 2010). However, experimental (Zhang et al., 2012) and numerical studies (Porté-Agel et al., 2011; Wu and Porté-Agel, 2011) reported that the wake rotation is weak in the far wake (x/d > 5) in the presence of turbulent boundary layer. Hence, its effect is neglected in this study for simplicity.

Next, we investigate the ability of the different analytical wake models to estimate the wind power available for extraction by another turbine placed at a given downwind location, and experiencing full-wake or partial-wake conditions. This available power is denoted as P_{av} and is defined as:

$$P_{av} = \int_{A_0} \frac{1}{2} \rho U_w^3 dA. \tag{2.22}$$

Therefore, if another turbine is located at that downwind location, it will extract an amount of power from the wind equal to P_{av} multiplied the power coefficient of the turbine C_p , which quantifies the ability of the turbine to extract the energy from the available wind (Burton et al., 1995). Fig. 2.8 shows the available power of the wind passing through a hypothetical turbine rotor located at x/d = 7 for different wind directions. In this figure, P_{av} denotes the available power predicted by analytical models, and the one obtained by the LES is denoted by $P_{LES,av}$. The variation of $P_{av}/P_{LES,av}$ versus the wind direction, θ , for the top-hat models reveals that the effect of assuming a top-hat shape for the velocity deficit leads to an inherent error in power prediction with respect to the LES data (see Fig. 2.8(c) and (d)). In fact, if a wind turbine operates in the full-wake of the upwind turbine (i.e., $\theta = 0^{\circ}$ in Fig. 2.8), top-hat

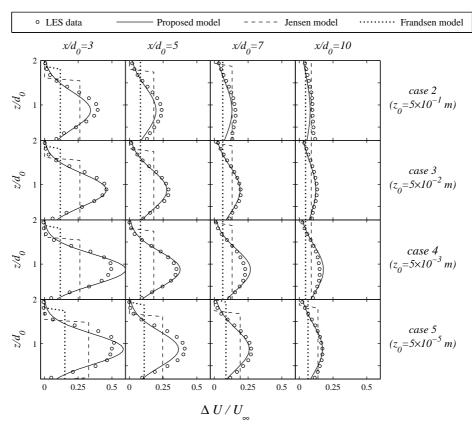


Figure 2.7 – Vertical profiles of the normalized velocity deficit in the wakes of real-scale turbines installed on flat surfaces with different roughness lengths (Cases 2-5): LES data (Wu and Porté-Agel, 2012) (*open circle*), new proposed model (*solid line*), the model proposed by Jensen (1983) (*dashed line*) and the model proposed by Frandsen et al. (2006) (*dotted line*).

models typically overestimate its produced power since they underestimate the velocity deficit in these regions. In contrast, if a turbine is located near the edge of the wake (partial-wake conditions), top-hat models underestimate the power due to the overestimation of the velocity deficit (e.g., $\theta = 5^{\circ}$ in Fig. 2.8(c)).

The above discussion therefore leads to the conclusion that top-hat models are adversely sensitive to the relative position of the turbines with respect to the wind direction. For instance, if the wind direction changes only 5 degrees (from $\theta = 0^{\circ}$ to 5°), $P_{av}/P_{LES,av}$ in Jensen model changes from 15 to 30 percent for the different cases (Fig. 2.8(c)), and this variation is even more for Frandsen model (Fig. 2.8(d)). It is important to note that if these models are used to optimize a wind-farm layout configuration with varying wind directions, this unrealistic behavior of top-hat models can cause considerable errors in the power prediction. By contrast, as shown by Fig. 2.8(b), the difference between the available power predicted by the new proposed model and the one obtained by the LES is much smaller compared with the one

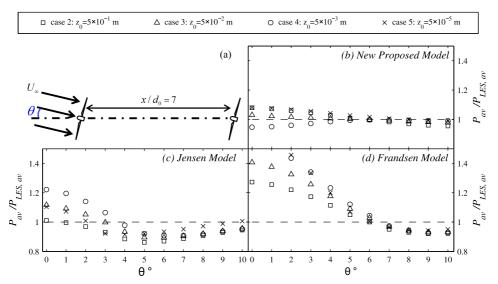


Figure 2.8 – Variation of $P_{av}/P_{LES,av}$ at $x/d_0 = 7$ as a function of wind direction for different analytical models: Case 2 (*square*), Case 3(*triangle*), Case 4 (*circle*), and Case 5 (*crosses*).

obtained with the top-hat models. Furthermore, there is not significant variation in the value of $P_{av}/P_{LES,av}$ as the wind direction changes. It changes only from 3 to 7 percent for the different cases if θ changes from 0° to 5° .

2.4 Summary

A new analytical model is proposed to predict the deficit of the streamwise velocity in the wake of a wind turbine. To this end, a Gaussian distribution is considered for the velocity deficit in the wake, and mass and momentum conservations are applied to evaluate the velocity profiles downwind of the turbine. Finally, the velocity deficit in the wake can be computed as:

$$\frac{\Delta U}{U_{\infty}} = \left(1 - \sqrt{1 - \frac{C_T}{8(k^* x/d_0 + 0.2\sqrt{\beta})^2}}\right) \times exp\left(-\frac{1}{2(k^* x/d_0 + 0.2\sqrt{\beta})^2} \left\{ \left(\frac{z - z_h}{d_0}\right)^2 + \left(\frac{y}{d_0}\right)^2 \right\} \right), \tag{2.23}$$

where β is obtained by Eq. 2.6 and k^* represents the wake growth rate. In order to predict the wake velocity distribution by the above equation, we only need to specify one parameter (value of k^*) for each case.

The comparison with the high-resolution wind-tunnel measurements (Chamorro and Porté-Agel, 2010) and the LES data (Wu and Porté-Agel, 2011, 2012) shows that the velocity profiles obtained with the proposed model are in acceptable agreement with the experimental and LES data for 5 different case studies including miniature and real-scale wind turbines with different boundary-layer turbulence conditions. By contrast, the top-hat models, as expected,

generally underestimate the velocity deficit at the center of the wake and overestimate it near the edge of the wake. Our results also reveal that the new proposed model is consistent and acceptably accurate in terms of power estimation whereas top-hat models are less accurate and adversely sensitive to the relative position of turbines with respect to the wind direction.

Future research will consider the effect of inflow conditions such as incoming velocity profile and ambient turbulence intensity on the wake expansion parameter, k^* . For this purpose, different experimental and numerical datasets obtained for a range of surface cover types and atmospheric stabilities will be used. In addition, the proposed analytical model will be extended to evaluate velocity profiles inside wind farms for different farm layout configurations and inflow conditions.

3 Experimental and theoretical study of wind turbine wakes in yawed conditions¹

Abstract

This work is dedicated to systematically studying and predicting the wake characteristics of a yawed wind turbine immersed in a turbulent boundary layer. To achieve this goal, wind tunnel experiments were performed to characterize the wake of a horizontal-axis wind turbine model. A high-resolution stereoscopic particle image velocimetry (S-PIV) system was used to measure the three velocity components in the turbine wake under different yaw angles and tip-speed ratios. Moreover, power and thrust measurements were carried out to analyze the performance of the wind turbine. These detailed wind tunnel measurements were then used to perform a budget study of the continuity and Reynolds-averaged Navier-Stokes (RANS) equations for the wake of a yawed turbine. This theoretical analysis revealed some notable features of the wakes of yawed turbines, such as the asymmetric distribution of the wake skew angle with respect to the wake center. Under highly yawed conditions, the formation of a counterrotating vortex pair (CVP) in the wake cross-section as well as the vertical displacement of the wake center were shown and analyzed. Finally, this study enabled us to develop general governing equations upon which a simple and computationally inexpensive analytical model was built. The proposed model aims at predicting the wake deflection and the far-wake velocity distribution for yawed turbines. Comparisons of model predictions with the wind tunnel measurements show that this simple model can acceptably predict the velocity distribution in the far wake of a yawed turbine. Apart from the ability of the model to predict wake flows in yawed conditions, it can provide valuable physical insight on the behaviour of turbine wakes in this complex situation.

¹The contents of this chapter are published in: M. Bastankhah and F. Porté-Agel. Experimental and theoretical study of wind turbine wakes in yawed conditions. *Journal of Fluid Mechanics*, 806:506–541, 2016.

3.1 Introduction

In order to address the increasing demand of wind energy production, researchers seek ways to improve the efficiency of existing and future wind farms. The most important cause of power losses in wind farms is the fact that turbines usually operate in the wakes of upwind ones. Yaw angle control is one of the methods that could be used to alleviate this situation by deflecting the wakes away from downwind turbines (Dahlberg and Medici, 2003). Even though yawing a turbine reduces its power production, it can potentially increase the total power generated by the whole wind farm.

To assess the viability of yaw-angle control strategies, a better understanding of the wakes of yawed turbines is crucial. Most of the previous studies of yawed turbines are limited to the performance of the turbine or the near-wake characteristics (e.g., Haans et al., 2005, 2007; Micallef et al., 2013; Sant, 2007; Krogstad and Adaramola, 2012; Grant et al., 1997; Grant and Parkin, 2000). Yawed turbines and their near wakes have also benefited from extensive studies of flow through helicopter rotors in forward flight as they are conceptually similar (e.g, Coleman et al., 1945).

Studies of the far wakes of yawed turbines, by contrast, have received rather little attention. In some of the early studies, Dahlberg and Medici (2003) and later Medici and Alfredsson (2006) quantified the far-wake velocity distribution at a few downwind locations for a yawed turbine located in a uniform flow. Their wind tunnel measurements confirmed that yawing the turbine can be used as a promising method to manipulate turbine wakes and mitigate their effects on downwind turbines. Later, Jiménez et al. (2010) used large-eddy simulation (LES) to investigate the deflection of wakes of yawed turbines with different thrust coefficients. They pointed out that, for a given yaw angle, the wake deflects more for turbines with higher thrust coefficients. Recently, Fleming et al. (2014) also used LES to study the wake of a turbine in yawed conditions and showed that yawing a turbine is an effective method to redirect its wake.

Even though these numerical simulations and wind tunnel measurements showed the potential of yaw-angle control, due to their high computational or measurement costs, they cannot be employed to fully assess the capability of this strategy under the wide variety of conditions that have to be considered for the optimum design and operation of wind farms. For example, wind farms are continuously exposed to change in mean wind magnitude and direction, ambient turbulence, thermal stability and wind turbine characteristics (Porté-Agel et al., 2013). Therefore, simple and inexpensive models that can predict the wakes of yawed turbines with an acceptable accuracy are still needed. Jiménez et al. (2010) assumed a top-hat profile for the wake velocity deficit and developed a simple formula to predict the wake deflection angle based on the conservation of mass and momentum for a control volume (CV) around the turbine. Based on this study, the wake skew angle θ is determined by

$$\theta = \frac{\sin \gamma C_T}{2\left(1 + \zeta \frac{x}{d}\right)^2},\tag{3.1}$$

where γ denotes the yaw angle, x is the downwind distance, d is the rotor diameter and ζ is the wake growth rate for the top-hat velocity-deficit profile which was chosen to be 0.1 for $\gamma = 10^\circ$, 20° and 0.125 for $\gamma = 30^\circ$ (Jiménez et al., 2010). In Eq. 3.1 and the remainder of this paper, the yaw angle γ is positive in the clockwise direction, and θ is positive in the counter-clockwise direction, seen from the top. Note that the apparent difference between Eq. 3.1 and the formula in the original work is due to the different definitions used for the thrust coefficient of the turbine C_T . In the current study, C_T is defined as

$$C_T = \frac{T}{0.5\rho \left(\frac{\pi}{4}d^2\right)\bar{u}_h^2},\tag{3.2}$$

where T is the total force exerted on the turbine by the incoming wind, ρ is the air density and \bar{u}_h is the incoming velocity at the hub height of the turbine. Later, Gebraad et al. (2014) integrated Eq. 3.1 to find the wake-center trajectory for a yawed turbine. They also used the top-hat model suggested by Jensen (1983) to describe the wake velocity, although the applicability of this model for wakes of yawed turbines is questionable.

Most of the aforementioned studies on far wakes of yawed turbines have been done from a pragmatic point of view. In other words, they essentially aimed at finding the amount of the wake deflection in different conditions, and whether or not the yaw-angle control can improve the wind farm power production. Despite the merit of those studies, many valuable insights could emerge from a more in-depth theoretical analysis of turbine wakes in yawed conditions. In addition to providing a better understanding, such theoretical analysis can ultimately help us develop more robust and accurate analytical models.

In the present work, detailed wind tunnel measurements are used to study the wake of a yawed wind turbine placed in a neutrally stratified boundary layer. Highly spatially resolved velocity measurements, together with thrust and power measurements, enable us to systematically study the interaction of the wake of the model turbine with the incoming turbulent boundary layer. These experimental data are then taken to study the budget of the steady-state continuity and Reynolds-averaged Navier-Stokes (RANS) equations. This budget study reveals some valuable features of turbine wakes in yawed conditions. In addition, the simplification of RANS equations results in the approximate governing equations upon which an inexpensive analytical model is built. This analytical model intends to acceptably predict the velocity distribution in the wake of a yawed turbine under different conditions.

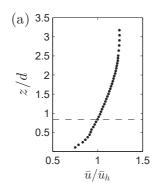
The remainder of this paper is organized as follows. In section 3.2, the experimental set-up and some key measurements are shown. The budget study of governing equations is then presented in Sect. 3.3. Section 3.4 is dedicated to examining the self-similarity for wakes of yawed turbines. An analytical model for the prediction of the far-wake velocity is then developed in Sect. 3.5, and the required wake characteristics in the onset of the far-wake region are specified in Sect. 3.6. The model predictions and the comparison with wind tunnel measurements are shown in Sect. 3.7. Finally, a summary is presented in Sect. 3.8.

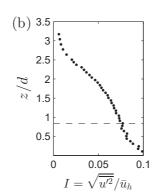
3.2 Wind tunnel measurements

Experiments were performed in the new closed-loop boundary-layer wind tunnel at the WIRE Laboratory of EPFL. The test section, designed for atmospheric boundary-layer studies, is 2.0 m high, 2.6 m wide and 28 m long. There is a contraction with a 5:1 area ratio upwind of the test section, and the tunnel is driven by a 130 kW fan. The turbulence intensity in the center of the wind tunnel (free stream) is lower than 0.1%. The turbulent boundary layer is naturally developed over the wind tunnel floor thanks to the long test section. In the current study, the measurements were performed approximately 22 meters downstream of the test section entrance. The time-averaged incoming velocity at the hub height of the turbine \bar{u}_h is kept constant at 4.88 m/s. Figures 3.1(a) and (b) show the vertical profiles of the normalized mean streamwise velocity \bar{u}/\bar{u}_h and the streamwise turbulence intensity I in the boundary layer in absence of the turbine obtained with hot-wire anemometry. The boundary-layer thickness is approximately 0.4 m at the turbine location. The aerodynamic surface roughness length and the friction velocity were found to be $z_0 = 0.022$ mm and $u_* = 0.22$ m/s, respectively, based on fitting a logarithmic velocity profile to the measured velocity profile in the surface layer (approximately lowest 15% of the boundary layer) as shown in Fig. 3.1(c).

A high-resolution S-PIV system from LaVision was used to measure three velocity components downstream of the turbine in the horizontal plane at hub height, i.e., xy plane, where x and y denote streamwise and spanwise directions, respectively. Two 29MP 12-bit CCD cameras (6600 × 4400 pixels) together with 105 mm lenses were installed on Scheimpflug mountings to maximize the focused area in the field of view (FOV). The area and spatial resolution of the FOV are $4d \times 2.5d$ and 0.015d, respectively, where d is the diameter of the wind turbine (15 cm). Data were sampled at a frequency of 1 Hz. The measurements were performed in three FOVs with some overlapping to capture the wake flow in a broad streamwise range from the near-wake (0.4d) to the far-wake region (12d). The mean velocity field was obtained by ensemble averaging 800 to 1000 instantaneous velocity fields. In addition to this PIV set-up, S-PIV measurements were performed in planes normal to the incoming flow (i.e., yz planes, where z denotes the vertical direction) at few selected downwind locations, mainly to study the structure of the wake cross-section under yawed conditions. Two 16-bit sCMOS cameras $(2560 \times 2160 \text{ pixels})$ were used to capture the wake flow in FOVs with the size of $3d \times 2d$ and the spatial resolution of 0.023d. Data were sampled at a frequency of 10 Hz. The mean velocity field was obtained by ensemble averaging 1200 instantaneous velocity fields.

The model wind turbine used in this experiment was designed and built at the WIRE laboratory of EPFL. This horizontal-axis turbine is three bladed, with a diameter of 15 cm. The blade profile is a 5% thick plate with a 5% circular arc camber. The height of the turbine hub above the floor is 12.5 cm. The blockage ratio of the wind turbine model to the wind tunnel cross-sectional area is less than 0.004, indicating that the confinement effect of the wind tunnel walls on the turbine wake is negligible. The turbine rotor drives a small DC-generator to extract the energy from the wind. The tower of the turbine was mounted on a multi-axis strain gauge sensor to measure the thrust force exerted by the wind on the model turbine. The tip-speed





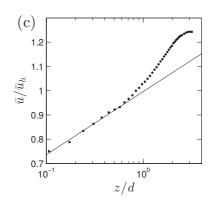


Figure 3.1 – Characteristics of the incoming turbulent boundary layer: (a) the normalized mean streamwise velocity profile, and (b) the streamwise turbulence intensity profile. The *horizontal dashed lines* represent the turbine hub height. (c) The normalized mean streamwise velocity profile in a semi-logarithmic scale. The *solid line* shows the fitted logarithmic profile.

ratio was also varied by applying different electrical loads on the generator attached to the turbine rotor.

Figure 3.2 shows the variation of the thrust coefficient C_T and power coefficient C_p of the wind turbine versus tip-speed ratio for different yaw angles. The value of C_T is calculated by Eq. 3.2 and C_p is calculated by

$$C_p = \frac{Q\Omega}{0.5\rho \left(\frac{\pi}{4}d^2\right)\bar{u}_h^3},\tag{3.3}$$

where Q is the torque generated by the rotor, and Ω is the rotational velocity of the rotor. The value of the generated torque Q is estimated by multiplying the generated electrical current by the torque constant of the DC-generator. The rotational velocity Ω is measured by the digital encoder attached to the DC-generator.

Figure 3.2 shows that both the thrust force and the generated power clearly decrease as the yaw angle increases which is expected and in agreement with previous studies (e.g., Krogstad and Adaramola, 2012).

For each yaw angle, the wake-flow measurements were performed for two different tip-speed ratios: (i) the tip-speed ratio of the turbine when the electrical circuit connected to the generator is open, so the turbine rotates freely. This tip-speed ratio is called λ_f later on in this paper. (ii) The tip-speed ratio at which the turbine has the maximum power production, and it is called the optimal tip-speed ratio λ_o in the following. λ_f and λ_o for each yaw angle are indicated in Fig. 3.2 with red colored points. For the sake of brevity, however, the following discussions will focus mostly on the data related to the optimal tip-speed ratio λ_o , unless otherwise stated.

Figure 3.3 shows contours of the normalized mean streamwise velocity \bar{u}/\bar{u}_h for different

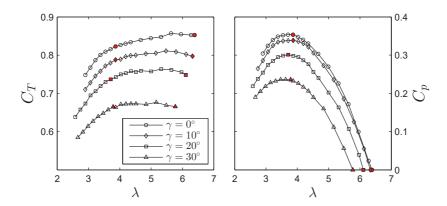


Figure 3.2 – Turbine performance versus tip-speed ratio (thrust coefficient C_T (*left*), and power coefficient C_p (*right*)) for different yaw angles: $\gamma = 0^\circ$ (*circle*), $\gamma = 10^\circ$ (*diamond*), $\gamma = 20^\circ$ (*square*), and $\gamma = 30^\circ$ (*triangle*). For red-colored points, PIV measurements were performed.

yaw angles ($\gamma=0^\circ$, 10° , 20° and 30°) in the horizontal plane at hub height. It can be seen that the wake velocity deficit reduces as the yaw angle increases because of the reduction in the total thrust force of the turbine (see Fig. 3.2). White dots in the figure show the loci of the maximum velocity deficit in the measured PIV plane at different downwind locations. As expected, the wake deflection increases with the increase of yaw angle. The black lines in the figure show the initial wake deflection predicted by Coleman et al. (1945). This study is further discussed in Sect. 3.6. Moreover, the white lines in Fig. 3.3 show the wake deflection predicted by the work of Jiménez et al. (2010), described by Eq. 3.1. As shown in the figure, this model considerably overestimates the wake trajectory for all cases. One can indeed improve the predictions by empirically adjusting the coefficient ζ in Eq. 3.1 for each case. However, this case specificity highlights the need for more realistic and robust modeling of turbine wakes in yawed conditions.

Although it is difficult to accurately predict the wake deflection, its cause can be explained simply by the conservation of momentum. A yawed turbine exerts a lateral force on the incoming airflow. Based on momentum conservation, this lateral force induces a spanwise wake velocity. This can be confirmed by Fig. 3.4 that shows contours of the normalized spanwise velocity \bar{v}/\bar{u}_h for two different yaw angles ($\gamma=0^\circ$ and 30°). As a result of this strong spanwise velocity distribution, the wake of a yawed turbine deflects to one side. It is also interesting to note that the peak of spanwise velocity surprisingly does not occur where the streamwise velocity deficit is maximum. This will be elucidated in the following section. In fact, it will be shown later in Sect. 3.3.2 that, based on the budget study of RANS equations, the spanwise velocity distribution has to be asymmetric with respect to the wake center.

Next, Fig. 3.5 shows contours of the normalized velocity deficit $\Delta \bar{u}/\bar{u}_h$ overlaid with vectors of in-plane velocity components in four yz planes located at different downwind locations (x/d=2,4,6 and 8) for five different yaw angles ($\gamma=0^\circ,10^\circ,20^\circ,30^\circ$ and -30°). The wake

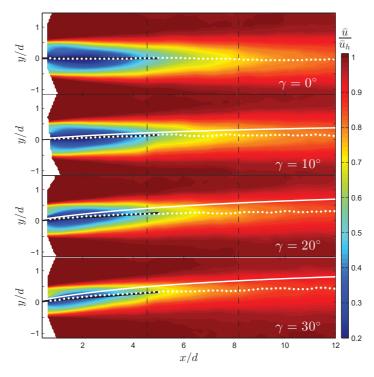


Figure 3.3 – Contours of the normalized mean streamwise velocity \bar{u}/\bar{u}_h in the horizontal plane at hub height downwind of a turbine for different yaw angles ($\gamma = 0^{\circ}$, 10° , 20° and 30°) at $\lambda = \lambda_o$. White dots and white lines represent the wake-center trajectory in the horizontal plane obtained from the wind tunnel measurements, and Jiménez et al. (2010) (Eq. 3.1), respectively. Black lines show the initial wake deflection predicted by Coleman et al. (1945) (Eq. 3.44). Overlapped locations of PIV planes are indicated by vertical dashed lines.

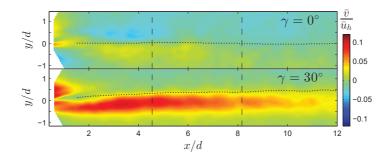


Figure 3.4 – Contours of the normalized mean spanwise velocity $(\bar{\nu}/\bar{u}_h)$ in the horizontal plane at hub height downwind of a turbine for two different yaw angles ($\gamma = 0^{\circ}$, and 30°) at $\lambda = \lambda_o$. Black dots represent the wake center trajectory in the horizontal plane, and overlapped locations of PIV planes are indicated by vertical dashed lines.

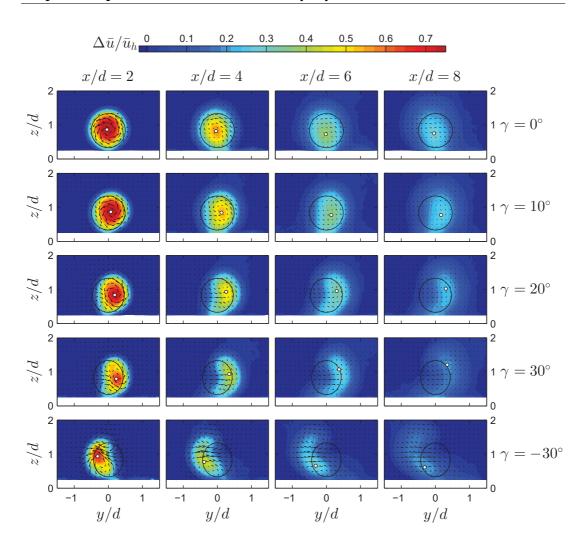


Figure 3.5 – Contours of the normalized streamwise velocity deficit in yz planes at different downwind locations and different yaw angles for a turbine operating at $\lambda = \lambda_o$. Black circles indicate the frontal area of the wind turbine and white dots represent the wake-center position at each downwind location. The vector field represents the in-plane velocity components.

center, defined as the point where the velocity deficit is maximum at each downwind location, is also shown by white dots in the figure.

As seen in the figure, a counter-rotating vortex pair (CVP) is formed as the wake moves downstream for higher yaw angles, so the wake has a kidney-shaped cross-section in the far-wake region. In addition to the current study, this kidney-shaped cross-section has been very recently reported for the wake of a yawed porous disk in uniform flows performed by Howland et al. (2016). However, no explanation regarding the formation mechanism of the CVP was provided in the mentioned study. The budget study of mean continuity equation will be employed in Sect. 3.3.1 to explain the mechanism leading to the CVP under highly yawed conditions. Moreover, the wake center is observed to move vertically for high yaw angles (e.g.,

 γ = 30°) and, more interestingly, the direction of this vertical displacement depends on the yaw-angle direction. This will be elaborated in Sect. 3.3.1.

3.3 Governing equations

3.3.1 Continuity equation

The mean continuity equation is

$$\underbrace{\frac{\partial \bar{u}}{\partial x}}_{(I)} + \underbrace{\frac{\partial \bar{v}}{\partial y}}_{(II)} + \underbrace{\frac{\partial \bar{w}}{\partial z}}_{(III)} = 0, \tag{3.4}$$

where u, v and w are the streamwise, spanwise and vertical velocities, respectively, and the overbar denotes ensemble averaging. Figure 3.6 shows contours of the terms of Eq. 3.4 in the horizontal plane at hub height of a turbine operating at two different yaw angles ($\gamma = 0^{\circ}$ and 30°). All the terms shown in the figure are normalized with respect to the averaged incoming velocity at hub height \bar{u}_h and the rotor diameter d. Note that only variations in the x and y directions can be calculated with S-PIV measurements in a horizontal plane, so term (III) shown in Fig. 3.6 is calculated based on the fact that Eq. 3.4 has to be balanced. The figure shows that although the terms of Eq. 3.4 are of the same order of magnitude for the non-yawed turbine, terms (II) and (III) are considerably bigger than term (I) in the far-wake region under yawed conditions.

In the following, the scale analysis of Eq. 3.4 will be used to explain the fundamental difference between the structure of wakes under non-yawed versus yawed conditions. The velocity scale \tilde{u}_s for the variation of \bar{u} can be defined as the maximum velocity deficit at each streamwise position (Tennekes and Lumley, 1972). Thus, we can write $\partial \bar{u}/\partial x = \mathcal{O}(\tilde{u}_s/L)$, where L denotes the scale of change in the x direction. Moreover, we define the velocity scale \tilde{v}_s for the variation of \bar{v} which is equal to the maximum value of \bar{v} at each streamwise position. This leads to $\partial \bar{v}/\partial y = \mathcal{O}(\tilde{v}_s/l)$, where l is the cross-stream scale, and $l/L \to 0$ in far wakes. One possibility is to assume that terms (I) and (II) in Eq. 3.4 are of the same order of magnitude which leads to the conclusion that $\tilde{v}_s = \tilde{u}_s l/L$. This means that \tilde{v}_s is considerably smaller than \tilde{u}_s in far wakes which occurs under non-yawed conditions (see Fig. 3.4). Equation 3.4 also implies that \tilde{w}_s , the velocity scale for the variation of \bar{w} , cannot be higher than $\tilde{u}_s l/L$ in this case.

For higher yaw angles, however, \tilde{v}_s cannot be assumed negligible compared to \tilde{u}_s . As already discussed, based on momentum conservation, \tilde{v}_s is generated due to the lateral component of the thrust force (i.e., $\approx T \sin \gamma$), whereas \tilde{u}_s is due to the streamwise component of the thrust force (i.e., $\approx T \cos \gamma$). As a result, if the yaw angle is large enough (i.e., $\tan \gamma \to 1$), we can write $\tilde{v}_s \approx \tilde{u}_s$. In this case, term (II) in Eq. 3.4 is considerably bigger than term (I), and consequently it has to be balanced with term (III). In other words, the continuity equation in the far wake of

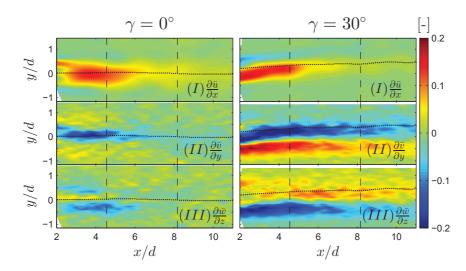


Figure 3.6 – Contours of the terms of the mean continuity equation (Eq. 3.4) in the horizontal plane at hub height for two different yaw angles ($\gamma = 0^{\circ}$, and 30°) at $\lambda = \lambda_o$. Contours are non-dimensionalized with \bar{u}_h and d. Black dots represent the locus of the maximum velocity deficit in the measured plane, and overlapped locations of PIV planes are indicated by vertical dashed lines.

a rotor with a high yaw angle is reduced to

$$\frac{\partial \bar{v}}{\partial y} + \frac{\partial \bar{w}}{\partial z} \approx 0 \tag{3.5}$$

Equation 3.5 states that the strong variation of \bar{v} in the y direction that occurs in wakes of turbines with a high yaw angle results in a strong variation of \bar{w} in the z direction, which in turn alters the shape of the wake cross-section. In fact, we hypothesize that the formation of the CVP presented in Fig. 3.5 can be explained with the analysis of Eq. 3.5. This is demonstrated in the schematic of the wake cross-section shown in Fig. 3.7. For the sake of simplicity, the incoming flow is assumed to be uniform and the wake rotation and ground effects are ignored for now but will be addressed later. In this regard, the horizontal line at the hub height can be considered as a symmetry line with $\bar{w} = 0$. Point **A** in Fig. 3.7 signifies the position where \bar{v} is maximum and, as already seen in Fig. 3.4, it does not occur in the locus of the maximum velocity deficit shown by point **C** in Fig. 3.7. On the left side of point **A** (region I), $\partial \bar{v}/\partial y > 0$ and from Eq. 3.5, $\partial \bar{w}/\partial z < 0$. On the other hand, $\partial \bar{v}/\partial y < 0$ and $\partial \bar{w}/\partial z > 0$ on the right side of point A (region II). As a result, \bar{w} becomes negative in region I and positive in region II. This spatial distribution of $\bar{\nu}$ and \bar{w} induces flow rotation as shown by solid arrows in the figure. At the wake edge shown by the horizontal dotted line in the figure, the induced spanwise velocity \bar{v} due to yawing the turbine becomes negligible, but the vertical component of velocity \bar{w} is still non-zero and variable due to the flow rotation mentioned above. In order to satisfy continuity, the flow rotation has to be therefore complete as shown by dotted arrows in the figure. With a similar argument, the presence of a counter-rotating vortex in the lower half of

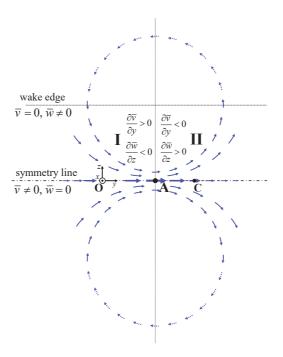


Figure 3.7 – Schematic figure of the mechanism leading to the formation of the CVP.

the wake cross-section can be expected.

A general conclusion that can be drawn by the aforementioned discussion is that any type of free shear flow with a strong variation of cross-wind velocity experiences the formation of CVP to satisfy the continuity. For instance, the presence of CVP in the cross-section of cross-flow jets can be justified similarly. Several different mechanisms for the formation of the CVP in cross-flow jets have been suggested in the literature (e.g., Broadwell and Breidenthal, 1984; Kelso et al., 1996; Cortelezzi and Karagozian, 2001; Muppidi and Mahesh, 2006; Marzouk and Ghoniem, 2007). See the review of Mahesh (2013) for more information in this context. However, to our best knowledge, it is the first time that mass conservation is used to explain the formation of the CVP. Indeed, it will be of great interest to further investigate the validity of our suggested mechanism leading to the CVP for other types of similar flows in future studies.

As mentioned earlier, the wake rotation and the presence of the ground are ignored in the idealized schematic figure of the wake cross-section shown in Fig. 3.7. In the following, we will examine how the CVP interacts with the ground and the wake rotation. For the sake of simplicity, we reduce the problem to a two-dimensional potential flow in the yz plane, where the CVP is modelled with counter-rotating vortices of strength Γ , and the wake rotation is modelled with a vortex of strength Γ' . Moreover, the presence of the ground is modelled by the method of images (see White, 2009, for more information). By using the complex variable

 $\xi = y + iz$, where $i = (-1)^{1/2}$, the complex potential $f(\xi)$ for this problem can be written as

$$f(\xi) = \frac{i\Gamma}{2\pi} (-\ln(\xi - \xi_1) + \ln(\xi - \xi_2) + \ln(\xi - \bar{\xi}_1) - \ln(\xi - \bar{\xi}_2)) + \frac{i\Gamma'}{2\pi} (-\ln(\xi - \xi_0) + \ln(\xi - \bar{\xi}_0)), (3.6)$$

where ξ_0 , ξ_1 and ξ_2 are the positions of the wake center and upper and lower vortices of the CVP, respectively, and the overbar denotes the complex conjugate. To find the velocities at each position, one can simply differentiate $f(\xi)$, so

$$\frac{\mathrm{d}f}{\mathrm{d}\xi} = v - i\,w. \tag{3.7}$$

It is worth recalling that the superposition of potential-flow solutions implies that each vortex is displaced by the other vortices, so the velocity at each vortex center is only due to the other vortices. Once the velocities are known, the vortices' displacements over time can be found by

$$d\xi = dy + idz = \int_0^t v dt + i \int_0^t w dt,$$
(3.8)

which can be solved numerically. The results are shown in Fig. 3.8 for different values of Γ and Γ' over an arbitrarily chosen time period of t=1.5 s. For the given time period, the wake-center's displacement is shown by a red curve in each figure, while the displacements of the CVP are indicated by blue curves. The initial vertical positions of vortices are selected rather similar to their real positions in wakes of yawed turbines. Note also that Γ and Γ' are assumed to be constant over the time for the sake of simplicity although both change in real situations.

In Figs. 3.8(a) and (b), the wake rotation is set to zero (i.e., $\Gamma' = 0$), so that the sole effect of the ground can be studied for both negative and positive Γ , which correspond to positive and negative yaw angles, respectively. The figures show that the wake center tends to slightly move upward with the same magnitude for both positive and negative yaw angles. If the wake rotation is taken into account, Figs. 3.8(c) and (d), however, show that the vertical displacement of the wake center can be either upward or downward depending on the direction of the wake rotation with respect to the one of the CVP. As can be seen in the figures, the wake rotation makes the wake center move upward if Γ and Γ' have the same sign, and *vice versa*. It is also interesting to note that the magnitude of the wake center displacement is smaller in both horizontal and vertical directions in Fig. 3.8(d) compared to the one in Fig. 3.8(c) which is consistent with the wind tunnel measurements shown in Fig. 3.5. This is due to the fact that the wake rotation and ground effects act against each other in Fig. 3.8(d). The accurate prediction of the wake-center displacement for real situations is obviously not possible via this simple method based on the potential theory. However, the comparison of Figs. 3.5 and 3.8 reveals that the employed method can provide useful insights on the origin and behavior of the wake-center vertical displacement observed for wakes of turbines with high yaw angles.

The vertical displacement of the wake center increases the net wake deflection under yawed conditions, which potentially can further mitigate wake effects on downwind turbines. As dis-

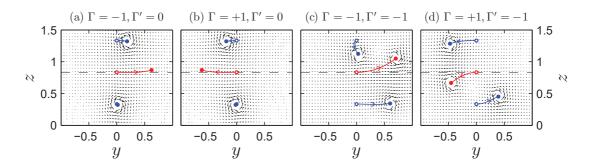


Figure 3.8 – Wake center displacement predicted by the potential theory. Red curves show the displacement of the wake center, and blue ones show the displacement of the CVP. The *Horizontal dashed lines* indicate the initial position of the wake center which is equal to the normalized turbine hub height z_h/d . The initial position of the pair of vortices is $z_h/d \pm 0.5$. Vectors show the flow field at $t = 1.5 \ s$.

cussed earlier, the direction of this vertical displacement depends on the yaw-angle direction for rotating wakes (e.g., wind turbine wakes). The wake can therefore be pushed towards the ground if the yaw angle is selected accordingly. This situation might be favorable in very large wind farms as the kinetic energy is transferred mainly from higher regions in the boundary layer towards wind turbines (Cal et al., 2010; Calaf et al., 2010; Lu and Porté-Agel, 2011; Abkar and Porté-Agel, 2013). On the other hand, yawing the turbine in the opposite direction moves the wake upward which leads to a slightly bigger wake deflection as shown in Figs. 3.5 and 3.8. Moreover, the upward motion of the wake may reduce the shear in the incoming flow and lead to a more uniform flow, which in turn can reduce unsteady loads on the blades of downwind turbines. It is, therefore, unclear at this stage which yaw-angle direction is more suitable, but this topic definitely deserves more attention in future studies. Note also that the vertical displacement of the wake center reduces with the decrease in yaw angle (see Fig. 3.5) simply because the CVP weakens for lower yaw angles.

3.3.2 Reynolds-Averaged Navier-Stokes (RANS) equations

The RANS equation in the streamwise direction at high Reynolds numbers is (Pope, 2000)

$$\underbrace{\bar{u}\frac{\partial \bar{u}}{\partial x} + \bar{v}\frac{\partial \bar{u}}{\partial y}}_{\text{(II)}} + \underbrace{\bar{w}\frac{\partial \bar{u}}{\partial z}}_{\text{(IV)}} = -\underbrace{\frac{1}{\rho}\frac{\partial \bar{p}}{\partial x}}_{\text{(IV)}} - \underbrace{\frac{\partial \bar{u}'^2}{\partial x}}_{\text{(V)}} - \underbrace{\frac{\partial \bar{u}'v'}{\partial y}}_{\text{(VI)}} - \underbrace{\frac{\partial \bar{u}'w'}{\partial z}}_{\text{(VII)}}, \tag{3.9}$$

where primes indicate turbulent fluctuations and p is the static pressure. Figure 3.9 shows contours of the terms in Eq. 3.9 measured in the horizontal plane at hub height for the wake of a turbine operating at two different yaw angles ($\gamma = 0^{\circ}$ and 30°). Additionally, the contours of the terms of Eq. 3.9 measured in a yz plane at x/d = 6 are shown in Fig. 3.10 for two different yaw angles ($\gamma = 0^{\circ}$ and 30°). On the line of intersection of the xy and yz PIV planes, all the

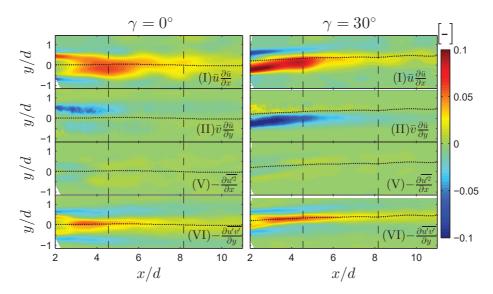


Figure 3.9 – Contours of the terms of the x-RANS equation (Eq. 3.9) measured in the horizontal plane at hub height for two different yaw angles ($\gamma=0^\circ$, and 30°) at $\lambda=\lambda_o$. Contours are non-dimensionalized with \bar{u}_h^2 and d. Black dots represent the locus of the maximum velocity deficit in the measured plane, and overlapped locations of PIV planes are indicated by vertical dashed lines.

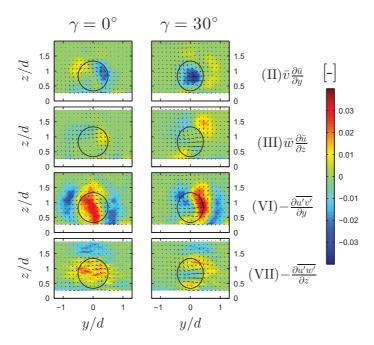


Figure 3.10 – Contours of the terms of the x-RANS equation (Eq. 3.9) measured in a yz plane at x/d=6 for two different yaw angles ($\gamma=0^\circ$, and 30°) at $\lambda=\lambda_o$. Contours are non-dimensionalized with \bar{u}_h^2 and d. Black circles indicate the frontal area of the wind turbine. The vector field represents in-plane velocity components.

terms of Eq. 3.9 except the pressure one, term (IV), can be calculated. Figure 3.11 shows the lateral profiles of all the measured terms on the line of intersection at x/d=6 for a turbine with $\gamma=30^\circ$. Firstly, the residual that is basically equal to the pressure term (term (IV)) in Eq. 3.9 is seen to be small. We, therefore, neglect this term compared to the dominant terms of Eq. 3.9 in the remainder of this paper. Secondly, Fig. 3.11 shows that terms (I), (II) and (VI) are bigger than the other terms at hub height. In order to quantify the change of these terms by moving downstream, the maximum of their normalized magnitude in the horizontal plane at hub height is plotted as a function of downwind distance in Fig. 3.12 for $\gamma=0^\circ$ and 30° . It can be seen that in the near wake of a yawed turbine, the convective terms are considerably higher than the shear stress term. The convective terms, however, diminish quickly as the wake moves downstream, and thus the shear stress becomes noteworthy in the far-wake region. In other words, the wake of a yawed turbine changes from a flow mostly dominated by gradients of mean velocities in the near wake to a turbulent free shear flow in the far wake, and it ultimately asymptotes to the wake of a non-yawed turbine.

Further analysis of Eq. 3.9 can reveal some important features of turbine wakes in yawed conditions. Multiplying the continuity equation (Eq. 3.4) by \bar{u} and then subtracting the resultant equation from Eq. 3.9 yields

$$\bar{v}\frac{\partial \bar{u}}{\partial y} - \bar{u}\frac{\partial \bar{v}}{\partial y} + \bar{w}\frac{\partial \bar{u}}{\partial z} - \bar{u}\frac{\partial \bar{w}}{\partial z} = -\frac{\partial \overline{u'^2}}{\partial x} - \frac{\partial \overline{u'v'}}{\partial y} - \frac{\partial \overline{u'w'}}{\partial z}.$$
(3.10)

As shown in Figs. 3.9 and 3.11, the first term on the right-hand side of the equation is negligible compared to the other terms. Moreover, $\overline{u'v'}$ and $\overline{u'w'}$ in the second and third terms on the right-hand side can be modelled with $-v_T(\partial\bar{u}/\partial y)$ and $-v_T(\partial\bar{u}/\partial z)$, respectively, where v_T is the turbulent viscosity. The left-hand side can also be rearranged based on the quotient derivative rule, which yields

$$\frac{\partial(\bar{v}/\bar{u})}{\partial y} + \frac{\partial(\bar{w}/\bar{u})}{\partial z} = -\frac{v_T}{\bar{u}^2} \frac{\partial^2 \bar{u}}{\partial y^2} - \frac{v_T}{\bar{u}^2} \frac{\partial^2 \bar{u}}{\partial z^2}.$$
 (3.11)

 \bar{v}/\bar{u} in the above equation is equal to $\arctan\theta$, where θ denotes the wake skew angle with respect to the streamwise direction. Our wind tunnel measurements as well as LES data (Jiménez et al., 2010) show that θ is always small even in extreme conditions (much smaller than 10° even at $\gamma=30^\circ$ and $C_T=0.8$), so $\tan\theta\approx\theta$ and \bar{v}/\bar{u} can be replaced with θ in Eq. 3.11. The above equation can be therefore written as

$$\frac{\partial \theta}{\partial y} + \frac{\partial (\bar{w}/\bar{u})}{\partial z} = -\frac{v_T}{\bar{u}^2} \frac{\partial^2 \bar{u}}{\partial y^2} - \frac{v_T}{\bar{u}^2} \frac{\partial^2 \bar{u}}{\partial z^2}.$$
 (3.12)

In appendix A, Eq. 3.12 is employed to mathematically prove that $\partial \bar{u}/\partial y$ has an extremum (i.e., $\partial^2 \bar{u}/\partial y^2 = 0$) if the skew angle has an extremum (i.e., $\partial \theta/\partial y = 0$). The proof is provided for the wake of a turbine with a low yaw angle and a uniform inflow. However, Fig. 3.13 shows that this finding is in good agreement with the PIV data even for the turbine wake with $\gamma = 30^\circ$ in boundary layer inflow conditions. In fact, it can be seen in the figure that the maximum

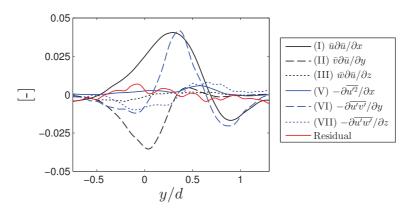


Figure 3.11 – Lateral profiles of the terms of the *x*-RANS equation (Eq. 3.9) at x/d = 6 for $\gamma = 30^{\circ}$ and $\lambda = \lambda_o$. Profiles are non-dimensionalized with \bar{u}_h^2 and d.

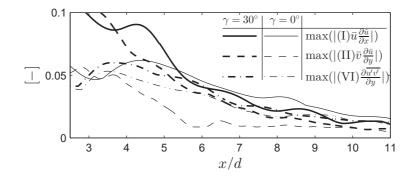


Figure 3.12 – Variation of the maximum values of the dominant terms of the *x*-RANS equation (Eq. 3.9) at hub height as a function of the downwind distance for two different yaw angles ($\gamma = 0^{\circ}$, and 30°) at $\lambda = \lambda_o$. Profiles are non-dimensionalized with \bar{u}_h^2 and d.

value of θ is in one side of the wake rather than the wake center, and it exactly occurs where $\partial^2 \bar{u}/\partial y^2 = 0$. It seems that there is another extremum for θ profiles on the other side of the wake where $\partial^2 \bar{u}/\partial y^2 = 0$ but it is difficult to comment on that as the magnitude of θ is very small on that side. It is worth mentioning that this finding, purely based on the x-RANS and continuity equations, is likely to be valid for other similar free shear flows such as inclined jets in crossflow.

This asymmetric distribution of the skew angle with respect to the wake center can also provide more insight on the origin of the wake deflection for yawed turbines. As shown in Fig. 3.11, terms (I), (II) and (VI) are the dominant terms of Eq. 3.9 at hub height in the far wake of a yawed turbine. They can be readily rewritten as

$$\frac{\partial \bar{u}}{\partial x} \approx \frac{v_T}{\bar{u}} \frac{\partial^2 \bar{u}}{\partial y^2} - \theta \frac{\partial \bar{u}}{\partial y}.$$
 (3.13)

The first term on the right-hand side of Eq. 3.13 is approximately symmetric with respect to the

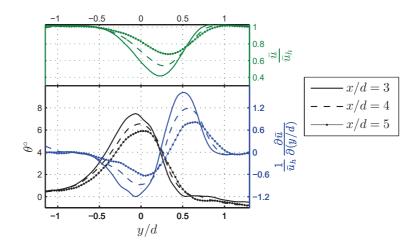


Figure 3.13 – Variation of θ , $\frac{1}{\bar{u}_h} \frac{\partial \bar{u}}{\partial (y/d)}$ and $\frac{\bar{u}}{\bar{u}_h}$ in the spanwise direction at three different downwind positions (x/d=3,4, and 5) for a turbine with $\gamma=30^\circ$ and $\lambda=\lambda_o$.

wake center. The maximum value of the second term on the right-hand side, however, occurs where θ is maximum (see Fig. 3.13). As a result, the term on the left side of Eq. 3.13, $\partial \bar{u}/\partial x$, has to be asymmetric with respect to the wake center so that the equation remains balanced. This implies that the wake velocity recovers faster on the side of the wake in which θ is bigger and, as a consequence, the wake shifts to the opposite side as it moves downstream. In other words, the wake deflection for yawed turbines cannot occur unless θ has an asymmetric distribution with respect to the wake center.

The RANS equation in the spanwise direction at high Reynolds numbers is

$$\underbrace{\bar{u}\frac{\partial\bar{v}}{\partial x}}_{(I)} + \underbrace{\bar{v}\frac{\partial\bar{v}}{\partial y}}_{(II)} + \underbrace{\bar{w}\frac{\partial\bar{v}}{\partial z}}_{(III)} = -\underbrace{\frac{1}{\rho}\frac{\partial\bar{p}}{\partial y}}_{(IV)} - \underbrace{\frac{\partial\bar{u}'v'}{\partial x}}_{(V)} - \underbrace{\frac{\partial\overline{v'^2}}{\partial y}}_{(VI)} - \underbrace{\frac{\partial\overline{v'w'}}{\partial z}}_{(VII)}.$$
(3.14)

Contours of the terms of Eq. 3.14 measured in the horizontal plane are shown in Fig. 3.14. In addition, contours of the terms of Eq. 3.14 measured in a yz plane at x/d = 6 are shown in Fig. 3.15. It can be seen that $\partial \overline{v'^2}/\partial y$ is generally bigger than the other terms, particularly in the far-wake region. This term is likely to be balanced with the pressure gradient term (term (IV)) which is the only term of Eq. 3.14 not measured in the present work. Note that these two terms are also in balance in the two-dimensional boundary-layer form of RANS equations (Pope, 2000).

3.3.3 Integral form of RANS equations

The integral form of the RANS equation in the streamwise direction has been extensively used in classical studies of bluff-body wakes (see Tennekes and Lumley, 1972; Pope, 2000;

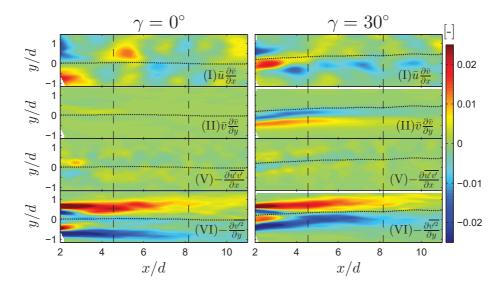


Figure 3.14 – Contours of the terms of the *y*-RANS equation (Eq. 3.14) measured in the horizontal plane at hub height for two different yaw angles ($\gamma = 0^{\circ}$, and 30°) at $\lambda = \lambda_o$. Contours are non-dimensionalized with \bar{u}_h^2 and d. Black dots represent the locus of the maximum velocity deficit in the measured plane, and overlapped locations of PIV planes are indicated by vertical dashed lines.

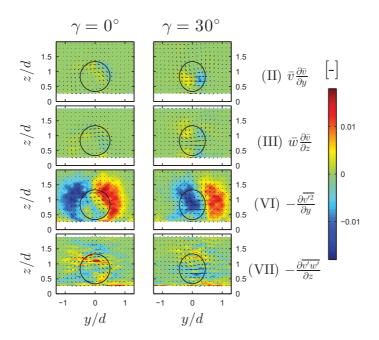


Figure 3.15 – Contours of the terms of the *y*-RANS equation (Eq. 3.14) measured in a yz plane at x/d=6 for two different yaw angles ($\gamma=0^\circ$, and 30°) at $\lambda=\lambda_o$. Contours are non-dimensionalized with \bar{u}_h^2 and d. Black circles indicate the frontal area of the wind turbine. The vector field represents the in-plane velocity components.

Johansson et al., 2003). As the mean incoming velocity \bar{u}_{∞} is only a function of z, equation 3.9, after neglecting the pressure term, can be written as

$$\bar{u}\frac{\partial(\bar{u}_{\infty}-\bar{u})}{\partial x} + \bar{v}\frac{\partial(\bar{u}_{\infty}-\bar{u})}{\partial y} + \bar{w}\frac{\partial(\bar{u}_{\infty}-\bar{u})}{\partial z} = \frac{\partial\overline{u'^2}}{\partial x} + \frac{\partial\overline{u'v'}}{\partial y} + \frac{\partial\overline{u'w'}}{\partial z} + \bar{w}\frac{\mathrm{d}\bar{u}_{\infty}}{\mathrm{d}z}.$$
 (3.15)

Equation 3.15 can also be written in conservative form. In order to do that, we multiply the continuity equation (Eq. 3.4) by $(\bar{u}_{\infty} - \bar{u})$ and then add the resultant equation to the left-hand side of Eq. 3.15. We obtain

$$\frac{\partial \bar{u}(\bar{u}_{\infty} - \bar{u})}{\partial x} + \frac{\partial \bar{v}(\bar{u}_{\infty} - \bar{u})}{\partial y} + \frac{\partial \bar{w}(\bar{u}_{\infty} - \bar{u})}{\partial z} = \frac{\partial \overline{u'^2}}{\partial x} + \frac{\partial \overline{u'v'}}{\partial y} + \frac{\partial \overline{u'w'}}{\partial z} + \bar{w}\frac{\mathrm{d}\bar{u}_{\infty}}{\mathrm{d}z}.$$
 (3.16)

In order to integrate Eq. 3.16 with respect to y and z from $-\infty$ to ∞ , we neglect the presence of the ground. Note that, however, this assumption might be questionable for very far-wake regions, where the wake clearly hits the ground. Integrating Eq. 3.16 leads to

$$\left(\frac{\mathrm{d}}{\mathrm{d}x}\int_{-\infty-\infty}^{\infty}\int_{-\infty}^{\infty}\left[\bar{u}\left(\bar{u}_{\infty}-\bar{u}\right)-\overline{u'^{2}}\right]\mathrm{d}y\mathrm{d}z\right)-\int_{-\infty-\infty}^{\infty}\int_{-\infty}^{\infty}\bar{w}\frac{\mathrm{d}\bar{u}_{\infty}}{\mathrm{d}z}\,\mathrm{d}y\mathrm{d}z=0.$$
(3.17)

The last term of the above equation can be neglected if: (i) the velocity gradient $d\bar{u}_{\infty}/dz$ of the incoming boundary layer is not very large and (ii) the yaw angle is not very high. Note that from the discussion of Sect. 3.3.1, \bar{w} is much smaller than the streamwise velocity deficit in the far-wake region for low yaw angles. Additionally, as shown in Fig. 3.9, the variation of \bar{u}'^2 in the streamwise direction is considerably smaller than the streamwise convective term, so it can be neglected in Eq. 3.17. Thus, Eq. 3.17 can be approximated as

$$\frac{\mathrm{d}}{\mathrm{d}x} \int_{-\infty}^{\infty} \int_{-\infty}^{\infty} \left[\bar{u} \left(\bar{u}_{\infty} - \bar{u} \right) \right] \, \mathrm{d}y \, \mathrm{d}z \approx 0. \tag{3.18}$$

This well-known equation states that *the streamwise momentum deficit flow rate* is conserved and independent of the downwind location.

To predict the wake deflection for a yawed turbine, we also need the integral form of the RANS equation in the spanwise direction. Multiplying the continuity equation (Eq. 3.4) by \bar{v} and then adding the resultant equation to the left-hand side of Eq. 3.14 leads to

$$\frac{\partial \bar{u}\bar{v}}{\partial x} + \frac{\partial \bar{v}\bar{v}}{\partial y} + \frac{\partial \bar{w}\bar{v}}{\partial z} = -\frac{1}{\rho}\frac{\partial \bar{p}}{\partial y} - \frac{\partial \overline{u'v'}}{\partial x} - \frac{\partial \overline{v'^2}}{\partial y} - \frac{\partial \overline{v'w'}}{\partial z}.$$
(3.19)

Integrating with respect to y and z from $-\infty$ to ∞ , we obtain

$$\frac{\mathrm{d}}{\mathrm{d}x} \int_{-\infty-\infty}^{\infty} \int_{-\infty}^{\infty} \left(\bar{u}\bar{v} + \overline{u'v'} \right) \mathrm{d}y \mathrm{d}z = 0. \tag{3.20}$$

It is interesting to note that both dominant terms of the differential form of the spanwise momentum equation (terms (IV) and (VI) in Eq. 3.14) are eliminated in its integral form Eq. 3.20. As no specific assumption is made to develop Eq. 3.20, it can be used for similar type of flows such as the wakes of airfoils or inclined jets in cross-flow. To our knowledge, our work is the first study that analyzes the budget of RANS equations in both streamwise and spanwise directions for a turbine wake, and also develops the integral form of RANS equation in the spanwise direction. Equation 3.20 can be simplified since the shear stress term is generally smaller than the advection term for a yawed turbine (see Fig. 3.14). $\bar{\nu}$ can be also replaced with $\bar{\nu}\theta$, hence

$$\frac{\mathrm{d}}{\mathrm{d}x} \int_{-\infty}^{\infty} \int_{-\infty}^{\infty} \bar{u}^2 \theta \, \mathrm{d}y \mathrm{d}z \approx 0. \tag{3.21}$$

The above equation states that *the flow rate of spanwise momentum* is conserved, regardless of the downwind location.

3.4 Self-similarity

It is well known that bluff-body wakes achieve self-similarity at a certain downwind distance. This means that the velocity deficit $\Delta \bar{u}$ profiles normalized by the maximum velocity deficit $\Delta \bar{u}_c$ against y^*/σ collapse onto a single curve for different downwind locations (Tennekes and Lumley, 1972), where σ is the characteristic width of the wake and y^* is the lateral distance from the wake center. Different possible ways were introduced in the literature to define the characteristic width of the wake: (i) the wake half-width $r_{1/2}$, where the velocity deficit is half of its maximum value (Pope, 2000), (ii) the position where the velocity is 99% of the incoming velocity and (iii) the standard deviation of a Gaussian fit of the velocity-deficit profile (Bastankhah and Porté-Agel, 2014). The first two methods are rather sensitive to the measurement uncertainty and the latter only works accurately for purely Gaussian profiles. If spatially resolved wake velocity profiles (e.g., from LES or PIV data) are available, the below equation does not have the mentioned limitations, and it can provide a more robust definition for the wake width:

$$\sigma_{y} = \frac{1}{\sqrt{2\pi} (\bar{u}_{\infty} - \bar{u}_{c})} \lim_{y \to \infty} \int_{-y}^{y} (\bar{u}_{\infty} - \bar{u}) \, d\hat{y}, \tag{3.22}$$

where σ_y is the wake width in y direction, \bar{u}_c is the velocity of the wake center, and \hat{y} is the integration variable. The integral can be calculated numerically to find the wake width at each downstream position. An equation similar to Eq. 3.22 can be also written for the wake width in the vertical direction. Note that for a pure Gaussian profile, Eq. 3.22 reduces to the standard deviation of the profile.

Previous studies showed that the velocity profiles in turbine wakes with zero yaw become

self-similar rather quickly (Bastankhah and Porté-Agel, 2014; Xie and Archer, 2015; Abkar and Porté-Agel, 2015). Figure 3.16(a) shows the lateral profiles of the normalized velocity deficit for the wake of a yawed turbine. As seen in the figure, despite the wake deflection, the wake of yawed turbines exhibits some degree of self-similarity in the horizontal plane at hub height. As mentioned earlier, one side of the wake (the left side in Fig. 3.16(a)) is influenced by the strong spanwise velocity distribution which makes the wake velocity profile slightly skewed and, as a result, the degree of self similarity is inferior in this side. However, the figure shows that in general self-similarity can be assumed for lateral velocity profiles in the far-wake region. Additionally, akin to bluff-body wakes, a Gaussian distribution, written as

$$\frac{\Delta \bar{u}}{\Delta \bar{u}_c} = \mathbf{e}^{-0.5(y_*/\sigma_y)^2},\tag{3.23}$$

acceptably fits the self-similar velocity profiles for most of the wake except the edges. In addition to the velocity profiles, the lateral profiles of the wake skew angle θ exhibit self-similarity to some extent, as shown by Fig. 3.16(b). Although the collapse of the θ -profiles is not as remarkable as the one for the velocity profiles, the figure shows that a Gaussian curve can be still used to approximately express the variation of θ . The center of the fitted Gaussian curve for θ profiles, however, lies somewhere close to $y^* = -\sigma_y$. Note that the peak value of θ should be located exactly at $y^* = -\sigma_y$ for a pure Gaussian velocity profile given the fact that at this lateral position $\partial^2 \bar{u}/\partial y^2 = 0$, and θ is thus maximum according to Eq. 3.12 and confirmed in figure 3.13. This small difference seen in the figure is due to the moderately asymmetric distribution of the velocity profiles discussed earlier. The wake skew angle distribution in the y direction can be therefore approximated by

$$\frac{\theta}{\theta_m} = \mathbf{e}^{-0.5\left(\frac{y_*}{\sigma_y} + 1\right)^2},\tag{3.24}$$

where θ_m is the maximum skew angle at each downwind location.

The value of the wake width at each downstream position is very important as it is used to examine self similarity. Furthermore, the proper estimation of its variation with the downwind distance is critical for the accurate prediction of the wake velocity distribution. In the absence of ambient turbulence, classical theories of free shear flows (see Tennekes and Lumley, 1972; Pope, 2000) state the well-known fact that three-dimensional turbulent wakes of bluff bodies such as disks and spheres grow proportional to $x^{-1/3}$, and the velocity deficit decays with x as $x^{-2/3}$. Far wakes of wind turbines are also shown to behave similarly under laminar inflow conditions (Dufresne and Wosnik, 2013b; Okulov et al., 2015). The evolution of wake flows is, however, considerably modified in the case of turbulent inflow conditions (Wu and Faeth, 1994; Bagchi and Balachandar, 2004; Amoura et al., 2010). Different numerical and experimental studies on wakes of spheres (e.g., Legendre et al., 2006), cylinders (e.g., Eames et al., 2011b) and wind turbines (see Bastankhah and Porté-Agel, 2014; Johnson et al., 2014) showed that turbulent far wakes grow approximately linearly with x in the presence of ambient turbulence. Eames et al. (2011a) tried to mathematically model the interaction of the ambient

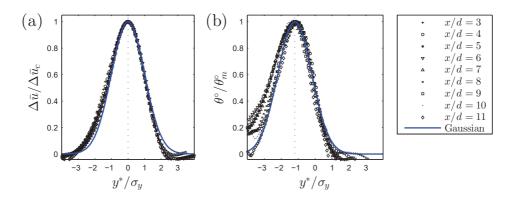


Figure 3.16 – The self-similar lateral profiles of (a) velocity deficit, and (b) wake skew angle at different downwind positions in the wake of a turbine with $\gamma = 30^{\circ}$ and $\lambda = \lambda_o$.

turbulence with wake flows. They suggested that the wake grows linearly with *x* and the wake growth rate is proportional to the incoming streamwise turbulence intensity provided that: (i) the velocity deficit is comparable or smaller than the standard deviation of the incoming velocity, and (ii) the wake radius is not bigger than the integral length scale of the incoming flow. In turbulent boundary-layer flows, both of these conditions are expected to be fulfilled for a broad streamwise range in turbine far wakes.

Figure 3.17 shows the wake width variation with the downwind distance calculated by Eq. 3.22 for different yaw angles. It can be seen that the wake width varies approximately linearly in the far-wake region for different yaw angles which is consistent with previous studies as the incoming flow is turbulent. In addition, the figure shows notably that the wake growth rate k is approximately the same for all the different yaw angles (k = 0.022 for this experimental configuration). This is in contrast with the common conjecture stating that the wake growth rate increases with increase in yaw angle (Jiménez et al., 2010). This can be explained by the fact that, as discussed in Sect. 3.3.2, the wake of a yawed turbine quickly asymptotes to a turbulent free shear flow in the far-wake region. In this flow regime, the wake recovery is mainly influenced by the incoming flow properties such as the ambient turbulence (Vermeulen, 1980). Turbine characteristics such as the thrust coefficient C_T or the yaw angle γ are likely to only affect the wake characteristics in the onset of the far-wake region. See for instance the intercepts of parallel lines corresponding to different yaw angles in Fig. 3.17. In the current study, the incoming turbulent boundary layer remained unchanged during the measurements, so the wake growth rate k is expected to be the same for different yaw angles.

3.5 Model derivation for the far-wake region

It is shown in Sect. 3.4 that velocity-deficit and skew angle profiles in the y direction can be acceptably represented by self-similar Gaussian distributions even for high yaw angles. However, a Gaussian profile cannot be fitted satisfactorily to the profiles in the z direction

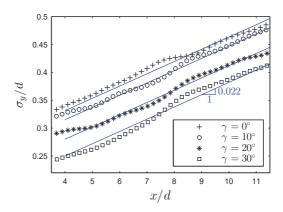


Figure 3.17 – Variation of the normalized lateral wake width σ_y/d for $\lambda = \lambda_o$: $\gamma = 0^\circ$ (*plus*), $\gamma = 10^\circ$ (*circle*), $\gamma = 20^\circ$ (*asterisk*), $\gamma = 30^\circ$ (*square*). Fitted lines with the slope of 0.022 are shown by blue lines.

for turbines with high yaw angles (e.g., $\gamma = 30^{\circ}$) since the wake cross-section has a kidney shape due to the presence of the CVP, as discussed in detail in Sect. 3.3.1 and shown in Fig. 3.5. Therefore, one may consider a more complicated shape in the z direction for this case, e.g., a bimodel distribution as used by Kikkert (2006) to represent the cross-section of cross-flow jets. However, yaw angles greater and equal to 30° are rather impractical for yaw-angle control methods, which is our main motivation to derive a simple analytical model for wind turbine wakes in yawed conditions. This is due to the fact that the substantial reduction in turbine power caused by a yaw angle of 30° is unlikely to be compensated by the increase in the power of downwind turbines (Jiménez et al., 2010).

As seen in our PIV measurements of turbine wakes as well as flow visualizations of inclined jets in cross-flow (Wang and Kikkert, 2014), the presence of the CVP is not strong for angles smaller than 30° , so a Gaussian distribution may still be used to approximate the wake in the z direction for yaw angles smaller than 30° . As a result, it seems unnecessary to consider a more complicated profile in the z direction, and a Gaussian distribution in both the y and z directions is used in this paper to approximate the velocity and skew angle profiles. It is worth mentioning that similar distribution has been also extensively used in studies of cross-flow jets (e.g., Fan, 1967; Abraham, 1970; Ooms, 1972) due to its simplicity. The velocity and skew angle distribution in the wake of a yawed turbine can be therefore written as

$$\frac{\bar{u}(x,y,z)}{\bar{u}_{\infty}} = 1 - C \mathbf{e}^{-\frac{(y-\delta)^2}{2\sigma_y^2}} \mathbf{e}^{-\frac{(z-z_h)^2}{2\sigma_z^2}},$$

$$\frac{\theta(x,y,z)}{\theta_m} = \mathbf{e}^{-\frac{(y-\delta+\sigma_y)^2}{2\sigma_y^2}} \mathbf{e}^{-\frac{(z-z_h)^2}{2\sigma_z^2}},$$
(3.25)

where *C* is the velocity deficit at the wake center normalized with the incoming velocity (i.e.,

Chapter 3. Experimental and theoretical study of yawed-turbine wakes

 $\Delta \bar{u}_c/\bar{u}_\infty$) and δ is the wake-center deflection at each downwind location. The wake center in Eq. 3.25 is assumed to remain at hub height z_h as the vertical displacement of the wake center is rather small for lower yaw angles (see Fig. 3.5). Furthermore, different wake widths in the y and z directions are considered in Eq. 3.25, denoted by σ_y and σ_z , respectively. Previous studies showed that the wake of a non-yawed turbine might have different widths in the spanwise and vertical directions due to the effect of ground (Xie and Archer, 2015) or incoming boundary-layer conditions (Abkar and Porté-Agel, 2015). The difference is, however, inevitable and more significant for a yawed turbine as its frontal area is an ellipse, instead of a circle, with the minor axis equal to $d\cos\gamma$ in the spanwise direction and the major axis equal to d in the vertical direction.

Substituting \bar{u} in Eq. 3.18 with Eq. 3.25 and integrating results in

$$\pi \bar{u}_{\infty}^2 \frac{\mathrm{d}}{\mathrm{d}x} \left[\sigma_y \sigma_z C (2 - C) \right] = 0. \tag{3.26}$$

The above equation is valid only in the far-wake region where the velocity distribution can be expressed by Eq. 3.25. In other words, Eq. 3.26 can be used from $x = x_0$ to ∞ , where x_0 indicates the downwind location where the velocity distribution achieves self-similarity. Thus, Eq. 3.26 can be written as

$$\sigma_{\nu_0}\sigma_{z_0}C_0(2-C_0) = \sigma_{\nu}\sigma_z C(2-C). \tag{3.27}$$

The values of variables at $x = x_0$ are shown with a zero in the subscript in Eq. 3.27 and in the remainder of this paper. All the variables related to $x = x_0$ will be determined in Sect. 3.6. For now, they are assumed as known values. Solving Eq. 3.27 for C gives

$$C = 1 - \sqrt{1 - \frac{\left(\sigma_{y_0} \sigma_{z_0}\right) M_0}{\left(\sigma_{y} \sigma_{z}\right)}},\tag{3.28}$$

where $M_0 = C_0 (2 - C_0)$. Equation 3.28 gives the maximum velocity deficit as a function of wake conditions in the far-wake onset $(\sigma_{y_0}, \sigma_{z_0} \text{ and } M_0)$ and wake widths $(\sigma_y \text{ and } \sigma_z)$. It is already seen in Sect. 3.4 that turbine far wakes expands approximately linearly with x in our interested streamwise range under the boundary-layer inflow condition which is always the case for wind turbines operating in the field. Therefore, σ_y and σ_z can be estimated by

$$\frac{\sigma_y}{d} = k_y \frac{(x - x_0)}{d} + \frac{\sigma_{y_0}}{d},$$

$$\frac{\sigma_z}{d} = k_z \frac{(x - x_0)}{d} + \frac{\sigma_{z_0}}{d},$$
(3.29)

where k_y and k_z are the wake growth rates in the spanwise and vertical directions, respectively.

Next, the wake deflection in the far-wake region will be determined. Inserting Eq. 3.25 in Eq.

3.21 and then integrating yields

$$\frac{2\pi\bar{u}_{\infty}^2}{3e^{1/3}}\frac{d}{dx}\left[\theta_m\sigma_y\sigma_z\left(C^2 - 3e^{1/12}C + 3e^{1/3}\right)\right] = 0,$$
(3.30)

so the wake skew angle of the wake center θ_c ($\theta_c = \theta_m \mathrm{e}^{-0.5}$) can be written as

$$\theta_c = \frac{\theta_{c_0}(\sigma_{y_0}\sigma_{z_0})E_0}{\sigma_y\sigma_z(C^2 - 3e^{1/12}C + 3e^{1/3})},$$
(3.31)

where $E_0 = C_0^2 - 3e^{1/12}C_0 + 3e^{1/3}$. Equation 3.31 can be integrated to find the wake deflection. After some algebraic manipulations (see Appendix B), δ can be written as

$$\delta = \delta_0 + \frac{\theta_{c_0} E_0}{5.2} \sqrt{\frac{\sigma_{y_0} \sigma_{z_0}}{k_y k_z M_0}} \ln \left[\frac{\left(1.6 + \sqrt{M_0}\right) \left(1.6 \sqrt{\frac{\sigma_y \sigma_z}{\sigma_{y_0} \sigma_{z_0}}} - \sqrt{M_0}\right)}{\left(1.6 \sqrt{\frac{\sigma_y \sigma_z}{\sigma_{y_0} \sigma_{z_0}}} + \sqrt{M_0}\right)} \right]. \tag{3.32}$$

Equation 3.32 gives the value of the wake deflection δ at each downwind location as a function of the wake characteristics in the far-wake onset as well as the wake growth rate. Note that Eq. 3.32 only takes into account the wake deflection due to yawing of the turbine, and the slight horizontal deflection caused by the interaction of the rotating wake and the incoming shear flow reported by Fleming et al. (2014) is not considered in the current study.

To close the model, the wake characteristics in the onset of the far-wake region (i.e., the values of variables at $x = x_0$) should be determined. The values of C_0 , θ_{c_0} , σ_{y_0} , σ_{z_0} and δ_0 will therefore be specified in Sect. 3.6.

3.6 Onset of the far-wake region

To find the wake characteristics in the onset of the far-wake region, one can benefit from the analogy between wakes and coflowing jets. For a jet in coflow, a region with a uniform velocity, called *potential core*, develops after the jet exit. The potential core, however, diminishes gradually as it moves downstream due to its interaction with the surroundings (Rajaratnam, 1976). After a certain downwind distance, the potential core ultimately disappears and the velocity profile develops fully into a self-similar Gaussian distribution (Fan, 1967). Few early studies (e.g., Lissaman, 1979; Vermeulen, 1980) tried to model the near wake of a non-yawed turbine in a similar manner. Although this idealized image of the near wake cannot evidently predict the detailed characteristics of this complex region, it will be shown in the following that it can be used to provide key characteristics of the far-wake onset, which are needed to model the far-wake region.

Figure 3.18 shows an idealized schematic of the wake of a yawed turbine. As the wake moves downstream, the potential core becomes smaller until it eventually ends at $x = x_0$. Before reaching this point, however, the central part of the potential core is not influenced by the

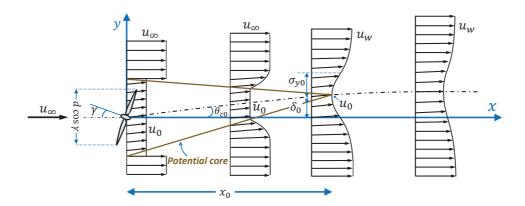


Figure 3.18 – Schematic of the wake of a yawed turbine.

ambient flow. Accordingly, the flow angle and the velocity magnitude in the wake center do not change across the potential core. After the termination of the potential core, the recovery of the wake center starts, and the wake deflection angle decreases due to the interaction with the ambient flow. The velocity and the wake deflection angle in the potential core are denoted by u_0 and θ_{c_0} , respectively, in Fig. 3.18.

As mentioned in Sect. 3.1, extensive research has been performed on yawed rotors and the flow passing through them mainly to improve the performance of helicopters and autogiros. Different methods have been suggested in the literature to relate C_T of yawed rotors to the induction factor in the direction normal to the rotor denoted by a. The one suggested by Glauert (1926) is widely used in previous studies (e.g., Sant, 2007; Haans, 2011) as it is simple and also able to estimate the thrust force of yawed turbines correctly (Burton et al., 1995). A more complicated alternative model is the one obtained with the vortex theory (see Burton et al. (1995) for the detailed discussion). However, both predict rather similar variation of C_T as a function of a, especially for $\gamma \le 20^\circ$. Thus, the former one is used in the current study for the sake of simplicity. Based on this model, the thrust coefficient C_T of a yawed rotor is determined by

$$C_T = \frac{4au_R}{u_{\infty}} = 4a\sqrt{1 - a(2\cos\gamma - a)},$$
 (3.33)

where u_R is the wind velocity at the rotor. Since we need to know the value of the normal induction factor a for a given C_T , the current form of (6.1) is not suitable because it has to be solved numerically for each value of C_T . Alternatively, an approximate expression of a can be found from Eq. 3.33 as seen in the following. First, Eq. 3.33 can be simplified as in general $\sqrt{1-x}$ asymptotes to (1-0.5x) for small values of x. Moreover, a can be ignored compared to $2\cos\gamma$, especially for lower yaw angles. Hence,

$$C_T \approx 4a\left(1 - a\cos\gamma\right). \tag{3.34}$$

From Eq. 3.34, we obtain

$$a \approx \frac{1}{2\cos\gamma} \left(1 - \sqrt{1 - C_T \cos\gamma} \right). \tag{3.35}$$

The value of *a* predicted by Eq. 3.35 always lies within $\pm 5\%$ of the true value provided that $C_T \le 1$ and $\gamma \le 30^\circ$. Substituting Eq. 3.35 into Eq. 3.33 gives u_R as a function of C_T and γ :

$$\frac{u_R}{u_\infty} = \frac{C_T \cos \gamma}{2\left(1 - \sqrt{1 - C_T \cos \gamma}\right)}.$$
(3.36)

The pressure of the air drops as it passes through the rotor; however, it returns to atmospheric pressure shortly downstream. Based on Bernoulli's equation, the velocity further decreases from u_R to u_0 (Sørensen, 2015). Applying the Bernoulli's equation in both upwind and downwind sides of the rotor results in

Upwind
$$p_{\infty} + \frac{1}{2}\rho u_{\infty}^2 = p_R^+ + \frac{1}{2}\rho u_R^2,$$
 (3.37)

downwind
$$p_R^- + \frac{1}{2}\rho u_R^2 = p_\infty + \frac{1}{2}\rho u_0^2$$
, (3.38)

where p_R^+ and p_R^- are the air pressure in front and back of the rotor, respectively. Subtracting the two equations to obtain the pressure drop across the rotor and then replacing the pressure drop with $(1/2)\rho u_\infty^2 C_T$ give the following simple relationship for u_0 :

$$\frac{u_0}{u_{\infty}} = \sqrt{1 - C_T}. (3.39)$$

Note that u_0 , unlike u_R , depends only on C_T for any yaw angle. The distance from the rotor to where the air velocity becomes equal to u_0 is typically assumed to be very small (Frandsen et al., 2006), so for the sake of simplicity, we assume that the air velocity remains equal to u_0 from x = 0 to x_0 across the whole potential core (see Fig. 3.18).

Figure 3.19 shows experimental values of the normalized maximum velocity deficit in the horizontal plane at hub height for different yaw angles and tip-speed ratios. In addition, the theoretical value of the normalized velocity deficit in the potential core (i.e., $C_0 = 1 - u_0/u_\infty$) predicted by Eq. 3.39 is shown in the figure by horizontal blue lines. As seen in the figure, not only are the real values of the maximum velocity deficit in all cases higher than the theoretical ones, but also they are not constant in the near-wake region in contrast with the assumption of constant velocity for the potential core. This departure is expected as the near-wake region has a highly complex structure due to the effect of the nacelle, rotating blades, etc. so we are unable to predict detailed characteristics of the near-wake region by assuming a potential core downwind of the turbine. However, it will be shown later that it can be still quite useful to provide some general but essential information about the near-wake region. As already implemented by Vermeulen (1980) for a non-yawed turbine, the location where the velocity

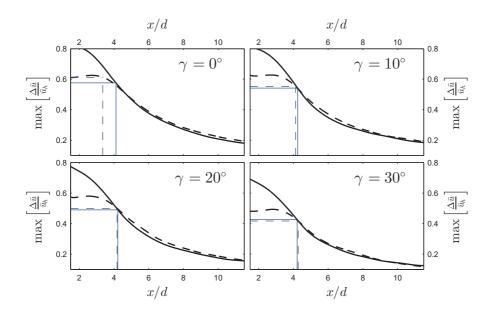


Figure 3.19 – Variation of the maximum normalized wake velocity deficit in the horizontal plane at hub height for different yaw angles shown by black lines. *Solid lines* and *dashed lines* correspond to $\lambda = \lambda_o$ and λ_f , respectively. Horizontal and vertical blue lines represent the values of u_0 and x_0 for each case, respectively.

deficit at the wake center reaches to the theoretical value can be considered as the end of the potential core (i.e., $x = x_0$) which is shown by vertical blue lines in Fig. 3.19.

It is important to note that as u_0 is smaller than u_R , the potential core area at x=0 should be considered bigger than the rotor area so that the mass is conserved. Based on mass conservation, the potential core area at x=0 is an ellipse whose vertical major axis is $d\sqrt{u_R/u_0}$ and lateral minor axis is equal to $d\cos\gamma\sqrt{u_R/u_0}$. It is worth remembering that the frontal rotor area is an ellipse with major and minor axes of d and $d\cos\gamma$, respectively.

As mentioned in Sect. 3.3.2, the streamwise momentum deficit flow rate is almost constant along the streamwise direction (Eq. 3.18). Given the velocity distribution at x = 0 and x_0 , the value of the streamwise momentum deficit flow rate can be calculated for these two locations as follows:

$$\int_{-\infty-\infty}^{\infty} \int_{-\infty}^{\infty} \left[u \left(u_{\infty} - u \right) \right] \, \mathrm{d}y \, \mathrm{d}z = \begin{cases} \frac{\pi d^2}{4} \frac{u_R}{u_0} \cos \gamma \, u_0 (u_{\infty} - u_0) & \text{at } x = 0 \\ \pi \sigma_{y_0} \sigma_{z_0} (u_{\infty} + u_0) (u_{\infty} - u_0) & \text{at } x = x_0. \end{cases}$$
(3.40)

Equating the two equations, and assuming an elliptic wake cross-section imposed by the rotor frontal area results in

$$\frac{\sigma_{z_0}}{d} = \frac{1}{2} \sqrt{\frac{u_R}{u_\infty + u_0}}, \qquad \frac{\sigma_{y_0}}{d} = \frac{\sigma_{z_0}}{d} \cos \gamma. \tag{3.41}$$

Inserting Eq. 3.36 and Eq. 3.39 into Eq. 3.41 leads to

$$\frac{\sigma_{z_0}}{d} = \sqrt{\frac{1 + \sqrt{1 - C_T \cos \gamma}}{8\left(1 + \sqrt{1 - C_T}\right)}} \approx \sqrt{\frac{1}{8}},$$

$$\frac{\sigma_{y_0}}{d} = \frac{\sigma_{z_0}}{d} \cos \gamma.$$
(3.42)

It is interesting to note that for a zero yawed turbine, σ_{y_0}/d and σ_{z_0}/d reduce to the constant value of $1/\sqrt{8}$. This might be used in general as an indicator to find the beginning of the self-similar region in limited wake measurements that usually occur in field measurements.

Figure 3.20(a) shows the values of σ_{y_0} predicted by Eq. 3.42 for different yaw angles against the ones obtained from the wind tunnel measurements. The comparison shows that the agreement is fairly good, especially for lower yaw angles.

Next, the wake skew angle in the potential core will be determined. Even though the model suggested by Glauert (1926) can estimate the thrust coefficient correctly (Burton et al., 1995), it is unable to properly estimate the skew angle of the flow past a yawed rotor. This is due to the fact that this model only takes into account the component of the induced velocity normal to the rotor, and not the tangential one. As a result, this model is expected to overestimate the flow skew angle at the rotor. Based on the vortex theory, however, the induced velocity at a yawed rotor has a tangential component equal to $a\tan(\chi/2)$, where χ is the flow skew angle with respect to the rotor axis (i.e., $\chi = \gamma + \theta$) (Coleman et al., 1945). Based on this work, the value of χ at the rotor disk can be approximated by (Burton et al., 1995)

$$\chi = \theta + \gamma = (0.6a + 1)\gamma. \tag{3.43}$$

By substituting a in Eq. 3.43 with Eq. 3.35, the value of θ at the rotor can be found by:

$$\theta \approx \frac{0.3\gamma}{\cos\gamma} \left(1 - \sqrt{1 - C_T \cos\gamma} \right). \tag{3.44}$$

Although Eq. 3.44 is intended for the estimation of the flow angle only at the rotor disk, it can acceptably predict the flow skew angle even up to a few rotor diameters downstream as shown in Fig. 3.3 by black lines. Thus, we use Eq. 3.44 to estimate the flow skew angle for the whole potential core indicated by θ_{c_0} in Fig. 3.18. It is noteworthy to mention that previous flow visualizations as well as inverse free wake simulations (Haans et al., 2005; Micallef et al., 2009) suggest an empirical formula of $\chi = (0.29C_T + 0.96)\gamma$ in the near wake of a yawed rotor. Although the predictions of the mentioned empirical formula are not shown here for the sake of brevity, they are found in good agreement with the predictions of Eq. 3.43.

Next, the wake deflection at $x = x_0$, δ_0 will be estimated. As the wake skew angle is assumed to be constant in the potential core, the value of δ_0 is simply equal to $x_0 \tan \theta_{c_0}$ or approximately $x_0 \theta_{c_0}$. To estimate the value of x_0 , we use a modified version of the hypothesis suggested by

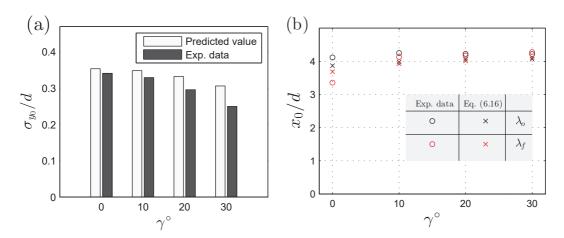


Figure 3.20 – (a) The value of the normalised lateral wake width at $x = x_0$, σ_{y_0}/d , for different yaw angles. The light gray bars show the values predicted by Eq. 3.42, and the black ones show the experimental data. (b) The prediction of the normalized potential core length x_0/d compared with the experimental data for different yaw angles and tip-speed ratios.

Lee and Chu (2012). It was originally used to find the length of the potential core for a round jet in coflow. Before applying this hypothesis for a yawed turbine, however, the interaction of the potential core and surroundings needs to be further elaborated. The difference in the velocity magnitude between these two regions creates a free shear layer between them as shown in Fig. 3.18. The velocity in this layer gradually increases from u_0 at the potential core border to u_∞ at the far lateral distance from the wake center. The velocity distribution in the horizontal plane at hub height for $0 \le x \le x_0$ can be therefore assumed to have the following distribution:

$$\frac{u}{u_{\infty}} = \begin{cases} 1 - C_0 & \text{if } r \le r_{pc}, \\ 1 - C_0 e^{-\frac{(r - r_{pc})^2}{2s^2}} & \text{if } r \ge r_{pc}, \end{cases}$$
(3.45)

where r is the lateral distance from the wake center, r_{pc} is the potential core radius in the horizontal plane at each x, and s denotes the characteristic width of the shear layer. The width of the shear layer increases from s=0 at x=0 to finally $s=\sigma_{y_0}$ at $x=x_0$. For a uniform and laminar incoming flow, Lee and Chu (2012) suggested that a change in width of a shear layer, in a Lagrangian frame of reference (moving with the eddies), is only proportional to the velocity difference between the potential core and unperturbed surroundings. In real situations, however, we know that the incoming turbulence also enhances the flow entrainment and consequently the growth of the shear layer. In this regard, we can generalize the model proposed by Lee and Chu (2012) by writing the variation of the shear layer width in the following form:

$$\frac{1}{u_{\infty}} \frac{\mathrm{d}s}{\mathrm{d}t} = \frac{u_s}{u_{\infty}} \frac{\mathrm{d}s}{\mathrm{d}x} = \alpha I + \beta \frac{u_e}{u_{\infty}},\tag{3.46}$$

where u_s is the characteristic velocity of the shear layer and is equal to $0.5(u_\infty + u_0)$, $I = \sqrt{\overline{u'^2}}/\bar{u}_h$ is the incoming streamwise turbulence intensity at hub height, u_e denotes the characteristic relative velocity in the shear layer which is equal to $0.5(u_\infty - u_0)$, and α and β are constants. Equation 3.46 can be integrated as follows:

$$\int_0^{\sigma_{y_0}} ds = \frac{u_\infty}{u_s} \left(\alpha I + \beta \frac{u_e}{u_\infty} \right) \int_0^{x_0} dx.$$
 (3.47)

Inserting the values of σ_{y_0} , u_s and u_e in Eq. 3.47 and integrating lead to

$$\frac{x_0}{d} = \frac{\cos\gamma \left(1 + \sqrt{1 - C_T}\right)}{\sqrt{2} \left[4\alpha I + 2\beta \left(1 - \sqrt{1 - C_T}\right)\right]}.$$
(3.48)

In order to use Eq. 3.48, values of α and β should first be estimated. The value of β can be determined thanks to the analogy with jet flows. In ideal conditions with no incoming turbulence (i.e., I = 0), Eq. 3.48 predicts a similar value for x_0 as the one reported in studies of jet flows if 2β is equal to 0.154. The value of α can then be found in such a way that Eq. 3.48 provides acceptable predictions for x_0 compared with our measured data. Figure 3.20(b) shows the values of x_0 for different cases predicted by Eq. 3.48 compared with the values obtained from the wind tunnel measurements. The value of α is chosen 0.58 to have an acceptable agreement with the experimental dataset. The available data are not likely to be sufficient to reliably find constant coefficients of Eq. 3.48; nonetheless, the figure shows that Eq. 3.48 is able to capture the variation of x_0 for different cases, provided α is properly specified. Indeed, more numerical simulations or wind tunnel measurements are needed to estimate the universal values of α and β . According to Eq. 3.48, it can be readily shown that the length of the potential core decreases with increasing thrust coefficient of the turbine, incoming turbulence and yaw angle. It is important to note that Eq. 3.48 does not aim to predict the detailed features of the near wake such as the location of the tip vortices' breakdown, but instead it is intended to estimate the length of the hypothetical potential core used for the far-wake modeling. It should be noted that the tip-speed ratio of the turbine and the wake rotation have no contribution in this equation as they have no effects on the far-wake region (Vermeer et al., 2003).

3.7 Model predictions

For the sake of completeness, the final form of the equations, which predict the far-wake velocity for a yawed turbine, is written in the following:

$$\frac{\Delta \bar{u}}{\bar{u}_{\infty}} = \left(1 - \sqrt{1 - \frac{C_T \cos \gamma}{8\left(\sigma_y \sigma_z / d^2\right)}}\right) \mathbf{e}^{-0.5\left(\frac{y - \delta}{\sigma_y}\right)^2} \mathbf{e}^{-0.5\left(\frac{z - z_h}{\sigma_z}\right)^2},\tag{3.49}$$

where the wake widths in the lateral and vertical directions can be, respectively, found by

$$\frac{\sigma_y}{d} = k_y \frac{(x - x_0)}{d} + \frac{\cos \gamma}{\sqrt{8}},$$

$$\frac{\sigma_z}{d} = k_z \frac{(x - x_0)}{d} + \frac{1}{\sqrt{8}}.$$
(3.50)

The normalized length of the potential core x_0/d is

$$\frac{x_0}{d} = \frac{\cos\gamma\left(1 + \sqrt{1 - C_T}\right)}{\sqrt{2}\left(\alpha^* I + \beta^* \left(1 - \sqrt{1 - C_T}\right)\right)},\tag{3.51}$$

where $\alpha^* = 2.32$ and $\beta^* = 0.154$. The normalized wake deflection δ/d is $\theta_{c_0}x/d$ for $x \le x_0$, and for $x > x_0$ it can be determined by

$$\frac{\delta}{d} = \theta_{c_0} \frac{x_0}{d} + \frac{\theta_{c_0}}{14.7} \sqrt{\frac{\cos \gamma}{k_y k_z C_T}} \left(2.9 + 1.3 \sqrt{1 - C_T} - C_T \right) \\
\times \ln \left[\frac{\left(1.6 + \sqrt{C_T} \right) \left(1.6 \sqrt{\frac{8\sigma_y \sigma_z}{d^2 \cos \gamma}} - \sqrt{C_T} \right)}{\left(1.6 - \sqrt{C_T} \right) \left(1.6 \sqrt{\frac{8\sigma_y \sigma_z}{d^2 \cos \gamma}} + \sqrt{C_T} \right)} \right], \quad (3.52)$$

where θ_{c_0} is calculated by Eq. 3.44. As x approaches to infinity, the wake deflection asymptotes to the constant value of

$$\frac{\delta_{\infty}}{d} = \theta_{c_0} \frac{x_0}{d} + \frac{\theta_{c_0}}{14.7} \sqrt{\frac{\cos \gamma}{k_y k_z C_T}} \left(2.9 + 1.3 \sqrt{1 - C_T} - C_T \right) \ln \left(\frac{1.6 + \sqrt{C_T}}{1.6 - \sqrt{C_T}} \right). \tag{3.53}$$

Figure 3.21 shows profiles of the wake velocities predicted by Eq. 3.49 against the wind tunnel measurements for $\gamma = 0^{\circ}$, 10° and 20° . To plot the model predictions, the wake growth rate in the vertical direction is assumed to be equal to the one in the horizontal direction (i.e., $k_y = k_z$) as the available velocity data in the z direction are limited. As clearly shown in the figures, the analytical model acceptably predicts the velocity distribution in the wake of a yawed turbine. The prediction on one side of the wake is, however, less accurate for higher yaw angles. This might be due to the fact that the wake velocity profiles are assumed to have a symmetric Gaussian distribution, whereas it was already shown that the velocity profiles are slightly skewed. This simple analytical model can, however, be particularly useful to assess the potential of yaw-angle control strategies for wind farm power optimizations.

It is worth mentioning that the proposed model is likely able to also predict the wake flow of a tilted turbine. In order to do so, the wake deflection δ in Eq. 3.49 should simply be reinserted into the Gaussian profile in the z direction, rather than the one in the y direction. However, one must bear in mind that the model should be used cautiously for tilted turbines because if

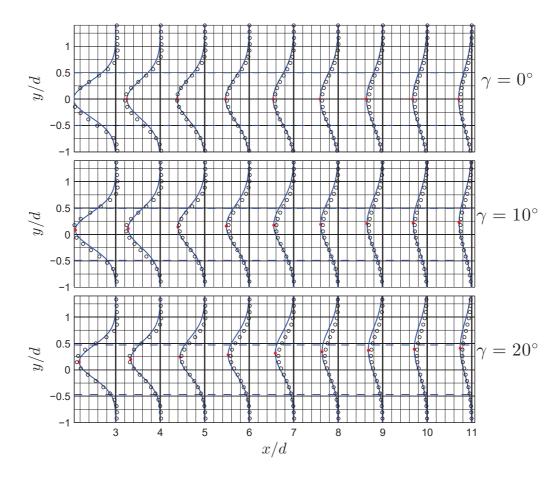


Figure 3.21 – Lateral profiles of the normalized streamwise velocity \bar{u}/\bar{u}_h in the wake of a turbine with $\gamma=0^\circ$, 10° and 20° at $\lambda=\lambda_o$: wind tunnel measurements (*open circle*), and new proposed model (*blue solid line*). Red dots show the wake center position predicted by the proposed model. Horizontal dashed lines indicate the location of the side tips of the turbine. For each downwind location, $\bar{u}/\bar{u}_h=1$ on the vertical thick black line. The width of grid squares corresponds to 15% of \bar{u}_h .

the turbine wake moves towards the ground, its interaction with the ground in the far-wake region cannot be considered negligible.

In addition to providing wake predictions, the proposed model can lead to a better understanding of the effect of different parameters on the turbine wake. For example, Fig. 3.22 shows the variation of the normalized wake deflection in the very far-wake region δ_{∞}/d predicted by the proposed model as a function of the incoming turbulence intensity I and the turbine thrust coefficient C_T for a turbine with $\gamma=20^\circ$. To calculate the wake deflection, the wake growth rate in the far-wake region is assumed to be linearly proportional to the incoming turbulence intensity as suggested by Johnson et al. (2014). It can be seen in the figure that the wake deflection increases with an increase in the thrust coefficient which is consistent with the finding of Jiménez et al. (2010). In addition, the figure shows that the

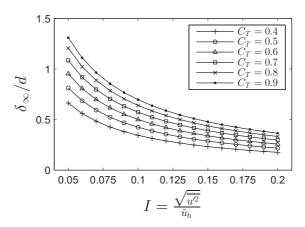


Figure 3.22 – Variation of δ_{∞}/d as a function of the incoming streamwise turbulence intensity $I=\sqrt{\overline{u'^2}}/\bar{u}_h$ for different values of thrust coefficient C_T . The yaw angle γ is assumed to be 20°.

wake deflection increases with a decrease in the incoming turbulence. The decrease in the incoming turbulence basically extends the length of the potential core, and it also reduces the flow entrainment in the far-wake region. As a result, the wake deflection increases in this case. This finding suggests that the implementation of yaw-angle control strategies in offshore wind farms, compared to onshore ones, is more promising.

It is important to note that, to estimate the wake characteristics in the onset of the far-wake region, we assumed that the turbine works in the windmill state, i.e., $C_T < 0.96$ (Manwell et al., 2010). Therefore, the model prediction is not likely to be valid for higher C_T values.

3.8 Summary

Wind tunnel measurements of the wake of a model wind turbine with different yaw angles $(0^{\circ}, 10^{\circ}, 20^{\circ})$ and $(0^{\circ}, 10^{\circ}, 20^{\circ})$ and tip-speed ratios were conducted in a turbulent boundary-layer flow. Power and thrust measurements were performed to study the performance of the wind turbine under these different operating conditions. In general, we found that, as expected, both the generated power and the thrust force of the turbine decrease with the increase of yaw angle. For each yaw angle, high-resolution S-PIV measurements were carried out in a horizontal plane at hub height covering a broad streamwise range (from (0.4d) to (

The detailed wind tunnel data were then used to study the budget of the continuity and the

RANS equations for the wake of a yawed turbine. The budget study of the continuity equation shows that a strong variation of the spanwise velocity occurring in highly yawed conditions leads to the formation of the CVP. Furthermore, a simple method based on the potential theory is employed to reveal that the vertical displacement of the wake center under yawed conditions is due to the interaction between the CVP, the ground and the wake rotation. The budget study of the RANS equations points out that the maximum value of the wake skew angle at each downwind location does not occur at the wake center, but instead it happens where the second derivative of the lateral profile of the streamwise velocity is zero. Our findings show that this asymmetric distribution of the wake skew angle with respect to the wake center is associated with the origin of the wake deflection for yawed turbines. The integral forms of the RANS equations in both streamwise and spanwise directions were then derived, which provides a solid basis for the development of a simple analytical model to predict the wake flows of yawed turbines.

In the far-wake region of a yawed turbine, self-similarity was examined for both the velocity and skew angle profiles. The results suggest that these profiles can be approximated with a self-similar Gaussian distribution in both spanwise and vertical directions for low yaw angles. The wake growth rate is found to be the same for different yaw angles. This is consistent with the assumption that the far-wake recovery is mainly influenced by incoming flow characteristics, and wind turbine characteristics solely affect the wake properties in the onset of the far-wake region.

The self-similarity analysis along with the budget study of RANS equations enabled us to develop an inexpensive analytical model to predict the velocity distribution in the far wake of a yawed turbine. A new method was employed to estimate the wake characteristics in the onset of the far-wake region (i.e., where self similarity holds). An idealized region with a uniform velocity, termed potential core, is assumed downwind of the turbine, analogous with coflowing jets. The potential core shrinks as the wake moves downstream until it eventually fades away, and after that the self-similar region starts to develop. Although the idealized concept of the potential-core flow cannot predict the complex three-dimensional structure of the near-wake region, it is shown that it can be successfully employed to provide the necessary information for the beginning of the far-wake self-similar region.

Finally, comparison with the high-resolution wind tunnel measurements shows that the model predictions of the velocity profiles in the wake of a model turbine with different yaw angles are in good agreement with the experimental data. The proposed model can be used as a useful tool to assess the possibility of wind farm power optimization by controlling the yaw angle of turbines. In addition to being a quantitative predictive tool, the proposed model can examine the effect of different turbine and incoming flow characteristics on the wake of a yawed turbine. For instance, a decrease in the incoming turbulence intensity is found to increase wake deflection for a yawed turbine. This suggests that the yaw-angle control has more potential to improve the power production of offshore wind farms, compared with onshore ones.

3.9 Appendix 1

Theorem. Suppose that the incoming flow is uniform, the flow is extended to infinity in both lateral and vertical directions and the turbine yaw angle is low. Then $\partial^2 \bar{u}/\partial y^2 = 0$ if $\partial \theta/\partial y = 0$.

Proof. Writing Eq. 3.12 for the lateral position where $\partial \theta / \partial y = 0$ gives

$$\frac{\partial(\bar{w}/\bar{u})}{\partial z} = -\frac{v_T}{\bar{u}^2} \frac{\partial^2 \bar{u}}{\partial v^2} - \frac{v_T}{\bar{u}^2} \frac{\partial^2 \bar{u}}{\partial z^2}.$$
(3.54)

Integrating Eq. 3.54 with respect to z from $-\infty$ to ∞ yields

$$\frac{\bar{u}}{\bar{u}}\Big|_{z=-\infty}^{+\infty} = -v_T \int_{-\infty}^{\infty} \frac{1}{\bar{u}^2} \frac{\partial^2 \bar{u}}{\partial y^2} dz - v_T \int_{-\infty}^{\infty} \frac{1}{\bar{u}^2} \frac{\partial^2 \bar{u}}{\partial z^2} dz.$$
 (3.55)

The left-hand side of Eq. 3.55 can be neglected as \bar{w}/\bar{u} vanishes at large values of z. Next, let \bar{u}_{∞} and \bar{u}_{c} denote the incoming velocity and the velocity at the wake center, respectively. Then,

$$\frac{1}{\bar{u}_c^2} \frac{\partial^2 \bar{u}}{\partial z^2} \ge \frac{1}{\bar{u}^2} \frac{\partial^2 \bar{u}}{\partial z^2} \ge \frac{1}{\bar{u}_{\infty}^2} \frac{\partial^2 \bar{u}}{\partial z^2}.$$
(3.56)

Integrating Eq. 3.56 with respect to z from $-\infty$ to ∞ leads to

$$\frac{1}{\bar{u}_c^2} \frac{\partial \bar{u}}{\partial z} \Big|_{z=-\infty}^{+\infty} \ge \int_{-\infty}^{\infty} \frac{1}{\bar{u}^2} \frac{\partial^2 \bar{u}}{\partial z^2} \, \mathrm{d}z \ge \frac{1}{\bar{u}_\infty^2} \frac{\partial \bar{u}}{\partial z} \Big|_{z=-\infty}^{+\infty}.$$
(3.57)

The middle term in Eq. 3.57 has to be equal to zero as both side terms are equal to zero, which in turn suggests that the second term on the right-hand side of Eq. 3.55 is also equal to zero. Hence, from Eq. 3.55,

$$\int_{-\infty}^{\infty} \frac{1}{\bar{u}^2} \frac{\partial^2 \bar{u}}{\partial y^2} \, \mathrm{d}z = 0. \tag{3.58}$$

Now, assume that \bar{u} at each x has the form of the product,

$$\bar{u} = \phi(y)\psi(z),\tag{3.59}$$

where both $\phi(y) \ge 0$ and $\psi(z) \ge 0$ for all the values of y and z. Although Eq. 3.59 is unlikely to be valid for wakes of turbines with high yaw angles, it is an acceptable assumption for wakes of turbines with low yaw angles where the wake cross-section can be approximated by a two-dimensional Gaussian function found in Eq. 3.25. From Eq. 3.59, we can write

$$\frac{\partial^2 \bar{u}}{\partial y^2} = \phi''(y)\psi(z). \tag{3.60}$$

Based on Eq. 3.60, we conclude that the sign of $\partial^2 \bar{u}/\partial y^2$ in the given lateral position does not change from $z=-\infty$ to ∞ (i.e., it is strictly non-negative or non-positive). Therefore, $\partial^2 \bar{u}/\partial y^2$ has to be zero in order to satisfy Eq. 3.58.

3.10 Appendix 2

This appendix contains the algebraic manipulations needed for the estimation of the wake deflection δ . In order to find the trajectory of the wake center, θ_c in Eq. 3.31 should be replaced with $\mathrm{d}y/\mathrm{d}x$, then Eq. 3.31 can be integrated to find the wake deflection δ at each x. To make the integration simpler, the product of $\sigma_v\sigma_z$ is approximated by $\bar{\sigma}^2$ which is defined as

$$\bar{\sigma} = \bar{k}(x - x_0) + \bar{\sigma}_0,\tag{3.61}$$

where $\bar{k} = \sqrt{k_y k_z}$ and $\bar{\sigma}_0 = \sqrt{\sigma_{y_0} \sigma_{z_0}}$. Note that $\bar{\sigma}^2$ is exactly equal to $\sigma_y \sigma_z$ if $k_y \sigma_{z_0} = k_z \sigma_{y_0}$. Moreover, C in the right-hand side of Eq. 3.31 should be substituted by Eq. 3.28 which gives

$$C^{2} - 3e^{1/12}C + 3e^{1/3} = \left[2 + 3\left(e^{1/3} - e^{1/12}\right)\right] - \frac{\bar{\sigma}_{0}^{2}M_{0}}{\bar{\sigma}^{2}} + \left(3e^{1/12} - 2\right)\sqrt{1 - \frac{\bar{\sigma}_{0}^{2}M_{0}}{\bar{\sigma}^{2}}}$$

$$\approx 2.93 - \frac{\bar{\sigma}_{0}^{2}M_{0}}{\bar{\sigma}^{2}} + 1.26\sqrt{1 - \frac{\bar{\sigma}_{0}^{2}M_{0}}{\bar{\sigma}^{2}}}.$$
(3.62)

 $\sqrt{1-\frac{\tilde{\sigma}_0^2M_0}{\tilde{\sigma}^2}}$ in the above equation can be replaced with $(1-\frac{\tilde{\sigma}_0^2M_0}{2\tilde{\sigma}^2})$ as $\tilde{\sigma}$ quickly grows in the far wake (note that $\sqrt{1-x}$ asymptotes to (1-0.5x) as $x\to 0$). Equation 3.62 is therefore simplified to

$$C^2 - 3e^{1/12}C + 3e^{1/3} \approx 1.6\left(2.6 - \frac{\bar{\sigma}_0^2 M_0}{\bar{\sigma}^2}\right).$$
 (3.63)

Now, inserting Eq. 3.63 into Eq. 3.31 and replacing θ_c with dy/dx enable us to find the wake deflection δ :

$$\int_{\delta_0}^{\delta} \mathrm{d}y \approx \frac{\theta_{c_0} \bar{\sigma}_0^2 E_0}{1.6\bar{k}} \int_{\bar{\sigma}_0}^{\bar{\sigma}} \frac{\mathrm{d}\hat{\sigma}}{2.6\hat{\sigma}^2 - \bar{\sigma}_0^2 M_0},\tag{3.64}$$

where dx is replaced with $d\hat{\sigma}/\bar{k}$. Performing the integration leads to

$$\delta \approx \delta_0 + \frac{\theta_{c_0} \bar{\sigma}_0 E_0}{2.6 \bar{k} \sqrt{M_0}} \left[\operatorname{arctanh} \left(\frac{1.6}{\sqrt{M_0}} \right) - \operatorname{arctanh} \left(\frac{1.6}{\sqrt{M_0}} \frac{\bar{\sigma}}{\bar{\sigma}_0} \right) \right]. \tag{3.65}$$

Chapter 3. Experimental and theoretical study of yawed-turbine wakes

After using hyperbolic trigonometric identities, Eq. 3.65 can be simplified to

$$\delta \approx \delta_0 + \frac{\theta_{c_0} \bar{\sigma}_0 E_0}{5.2 \bar{k} \sqrt{M_0}} \ln \left[\frac{\left(1.6 + \sqrt{M_0} \right) \left(1.6 \frac{\bar{\sigma}}{\bar{\sigma}_0} - \sqrt{M_0} \right)}{\left(1.6 - \sqrt{M_0} \right) \left(1.6 \frac{\bar{\sigma}}{\bar{\sigma}_0} + \sqrt{M_0} \right)} \right]. \tag{3.66}$$

4 Wind tunnel study of the boundary layer flow interaction with a wind turbine under different operating conditions¹

Abstract

Comprehensive wind tunnel experiments were carried out to study the interaction of a turbulent boundary layer with a wind turbine operating under different tip-speed ratios and yaw angles. Force and power measurements were performed to characterize the variation of thrust force (both magnitude and direction) and generated power of the wind turbine under different operating conditions. Moreover, flow measurements, collected using high-resolution particle-image velocimetry (PIV) as well as hot-wire anemometry, were employed to systematically study the flow in the upwind, near-wake and far-wake regions. These measurements provide new insights into the effect of turbine operating conditions on flow characteristics in these regions. For the upwind region, the results show a strong lateral asymmetry under yawed conditions. For the near-wake region, the evolution of tip and root vortices was studied with the use of both instantaneous and phase-averaged vorticity fields. The results suggest that the vortex breakdown position cannot be determined based on phase-averaged statistics, particularly for tip vortices under turbulent inflow conditions. Moreover, the measurements in the near-wake region indicate a complex velocity distribution with a speed-up region in the wake center, especially for higher tip-speed ratios. In order to elucidate the meandering tendency of far wakes, particular focus was placed on studying the characteristics of verylarge-scale motions in the boundary layer and their interaction with wind turbines. Although the very-large-scale motions are elongated in the streamwise direction, their cross sections are found to have a size comparable to the rotor area, so they can be affected by the presence of the turbine. In addition, the study of spatial coherence in turbine wakes reveals that any statistics based on streamwise velocity fluctuations cannot provide reliable information about the size of large turbulent structures in turbine wakes due to the effect of wake meandering.

¹The contents of this chapter are under review in *Physics of Fluids*.

The results also suggest that the magnitude of wake meandering does not depend on turbine-operating conditions. Finally, the suitability of the proper orthogonal decomposition (POD) for studying wake meandering is examined.

4.1 Introduction

As wind turbines operate within the atmospheric boundary layer (ABL), the study of their interaction with the ABL is essential to better characterize their performance. Apart from ABL characteristics, turbine operating conditions such as the tip-speed ratio (i.e., the ratio between the velocity of the blade tip to the incoming velocity at hub height) and the yaw angle of the turbine can considerably affect wind turbine performance (e.g., power production). The impact of turbine operating conditions can also be detected in the flow upwind of the turbine, near- and far-wake regions.

Numerous numerical simulations, field and wind tunnel experiments have been performed (see the reviews of Crespo et al., 1999; Vermeer et al., 2003; Sørensen, 2011; Mehta et al., 2014) to study the performance of wind turbines and the airflow disturbed by their presence. Some of these works are discussed in the following, with an emphasis on wind tunnel studies.

4.1.1 Wind turbine performance

The performance of a wind turbine can be essentially characterized by the manner in which the power P and the thrust force T vary in different conditions. In order to facilitate the comparison, the normalized thrust force, called thrust coefficient C_T , and the normalized power, called power coefficient C_p , are widely used in the wind energy community. They are computed as

$$C_{T} = \frac{T}{0.5\rho(\frac{\pi}{4}d^{2})\bar{u}_{h}^{2}},$$

$$C_{p} = \frac{P}{0.5\rho(\frac{\pi}{4}d^{2})\bar{u}_{h}^{3}},$$
(4.1)

where ρ is the air density, d is the rotor diameter and \bar{u}_h is the mean incoming velocity at hub height. The variation of C_T and C_P as a function of tip-speed ratio for a turbine with zero yaw angle has been extensively studied in the literature (see Burton et al., 1995; Sørensen, 2011, for a detailed discussion). However, the variation of these parameters with yaw angle has received relatively less attention. Although previous experimental studies on yawed turbines (e.g., Krogstad and Adaramola, 2012; Ozbay et al., 2012) often showed that the power coefficient C_p is proportional to $\cos^3 \gamma$, where γ is the yaw angle, Pedersen (2004) reported that $C_p \propto \cos^2 \gamma$. This discrepancy indicates the need of further study on the power production of yawed turbines. Moreover, a proper estimation of the magnitude and the direction of the

thrust force for yawed turbines is of great importance as they affect both the strength and deflection of the wake. The thrust force is typically assumed to be normal to the rotor in classical studies of yawed rotors (see Burton et al., 1995) or in numerical simulations with standard actuator disk models without rotation (e.g., Jiménez et al., 2010), whereas to our knowledge this assumption has not been experimentally verified for wind turbines.

4.1.2 Upwind region

Based on the actuator disk concept, the velocity of the airflow is reduced upwind of the turbine (Sørensen, 2015). The axial induction factor a is introduced to express the amount of this velocity reduction at the rotor, which is defined as $a = (u_{\infty} - u_R)/u_{\infty}$, where u_{∞} is the axial velocity far upstream, and u_R is the axial velocity at the rotor plane. Applying axial momentum theory for a turbine with zero yaw angle leads to (Manwell et al., 2010)

$$a = \frac{1}{2} \left(1 - \sqrt{1 - C_T} \right). \tag{4.2}$$

Vortex sheet theory can be used to theoretically express the change of axial velocity u along the symmetry axis upwind of the actuator disc. It states that (Medici et al., 2011)

$$\frac{u}{u_{\infty}} = 1 - a \left(1 + \frac{2x}{d} \left(1 + \left(\frac{2x}{d} \right)^2 \right)^{-0.5} \right),\tag{4.3}$$

where x is the streamwise position with respect to the rotor, being negative for the upwind region. In addition to the theoretical prediction, some field measurements (Larsen and Hansen, 2014; Forsting et al., 2015; Simley et al., 2016), wind tunnel experiments (Medici et al., 2009, 2011; Howard and Guala, 2015) and numerical simulations (Simley et al., 2014) have been performed to study the upwind region. Medici et al. (2009) and Medici et al. (2011) measured the flow upwind of a model turbine in uniform inflow conditions. Howard and Guala (2015) quantified the flow upwind of a turbine in a boundary layer but they could not properly estimate the value of a as C_T was not measured in their study. In this regard, it is of interest to carry out a fully controlled wind tunnel study on the upwind region of a turbine immersed in a turbulent boundary layer.

For a yawed rotor, the flow in the upwind region becomes laterally asymmetric and more complex (Burton et al., 1995). Glauert (1926) postulated that the axial induction factor a is not uniform on an annular section of a yawed rotor, in such a way that it is bigger in the downwind side of the rotor compared to the upwind side. Although Glauert's model has been studied (e.g., Sant, 2007; Haans, 2011) and widely used in blade element momentum (BEM) simulations of yawed turbines (e.g., Hansen et al., 2006; Haans et al., 2006), to our knowledge, spatially resolved flow measurements in the upwind region of yawed turbines have not been performed to verify this model.

4.1.3 Near-wake region

Although many laboratory experiments have been recently performed to investigate turbine near wakes (e.g., Dobrev et al., 2008; Zhang et al., 2012; Yang et al., 2012; Zhang et al., 2013; Chamorro et al., 2013b; Sherry et al., 2013b,a; Odemark and Fransson, 2013; Okulov et al., 2014; Lignarolo et al., 2014), studying near wakes still remains a formidable challenge. This is due to the fact that the near-wake region is a complex heterogenous three-dimensional flow which is characterized by the signature of helical vortex structures, shedding from the tip and the root of rotor blades (Whale et al., 2000; Zhang et al., 2012), as well as the hub vortex (Felli et al., 2011; Iungo et al., 2013; Viola et al., 2014). Moreover, the flow distribution in this region is profoundly influenced by the geometry of the hub and the nacelle as well as the rotor properties such as the tip-speed ratio of the turbine and the blade cross-sectional profile (Crespo et al., 1999). Krogstad and Adaramola (2012) studied the mean flow distribution in the near wake of a turbine with different tip-speed ratios and yaw angles under uniform inflow conditions.

Phase-locked PIV measurements (e.g., Yang et al., 2012; Sherry et al., 2013a,b; Lignarolo et al., 2014) have been used to study the evolution of vortex structures in the near wake. However, previous studies (e.g., Dobrev et al., 2008) showed that random fluctuations (i.e., wandering) of vortex structures lead to an underestimation in the vortex strength represented by phase-averaged data .

Most of the above-mentioned laboratory experiments were carried out under uniform inflow conditions, which are not fully representative of non-uniform characteristics of ABL flows where wind turbines operate in the field. Zhang et al. (2012, 2013) studied the effect of different types of ABL flows (neutral and convective) on the near wake of a model turbine. Their studies were limited to a turbine with zero yaw angle and a given tip-speed ratio. It is thus of great interest to elucidate the near-wake region of a turbine under different tip-speed ratios and yaw angles for the case that the turbine is located in a turbulent boundary layer.

4.1.4 Far-wake region

The far-wake region located downwind of the near wake is of great importance as downwind turbines in wind farms have to usually operate in this region. Recent wind tunnel experiments (e.g., Chamorro and Porté-Agel, 2009, 2010; Zhang et al., 2013; Hancock and Pascheke, 2014; Hancock and Zhang, 2015) have studied the far-wake region under different boundary-layer conditions. Chamorro and Porté-Agel (2009) showed that, for boundary-layer incoming flows, velocity deficit profiles in the far-wake region have a Gaussian distribution. Self-similarity of velocity deficit profiles in the far wake has been examined in previous studies (e.g., Bastankhah and Porté-Agel, 2014; Xie and Archer, 2015; Abkar and Porté-Agel, 2015) and is the basis of simple far-wake analytical models (e.g., Bastankhah and Porté-Agel, 2014). It is also used by other studies (e.g., Sørensen et al., 2015) as an indicator to find the onset of the far-wake region.

Unsteady lateral oscillations of the wake center called wake meandering are a key dynamic feature of far wakes. The meandering tendency of turbine wakes has to be properly understood as it affects the performance of downwind turbines; for instance, it increases fatigue loads experienced by downwind turbines (Larsen et al., 2008). For uniform inflow conditions, periodic lateral oscillations of turbine wakes, termed vortex shedding, similar to what can be observed for bluff body wakes have been reported by previous studies (e.g., Medici and Alfredsson, 2006; Okulov et al., 2014). Nonetheless, in the case of boundary-layer inflow conditions, the wake meanders in an irregular manner due to large-scale structures in the boundary layer, so that the periodic vortex shedding is masked in this case (España et al., 2011, 2012). These large-scale structures in boundary-layer flows are termed in different ways in the literature: superstructures (Hutchins and Marusic, 2007), large-scale turbulent eddies by some studies in the wind energy community (e.g., Larsen et al., 2008; España et al., 2012), and very-large-scale motions (VLSMs) (e.g., Kim and Adrian, 1999); the latter one is mostly used in the current paper. VLSMs are inclined high- and low-speed streaks that are elongated in the streamwise direction, and they can be even as long as 20δ (Hutchins and Marusic, 2007; Fang and Porté-Agel, 2015), where δ is the boundary layer thickness. In addition, they contain substantial portions of turbulent kinetic energy and turbulent shear stress (Guala et al., 2006; Balakumar and Adrian, 2007; Lee and Sung, 2011). Previous studies (e.g., Hutchins et al., 2012) showed that VLSMs in the logarithmic region of laboratory-scale boundary layers and in the surface layer of ABLs are very similar, despite the existence of big differences in Reynolds numbers. In this regard, wind tunnel studies of VLSMs and their interaction with wind turbines can certainly provide more insights on wake meandering.

Proper orthogonal decomposition (POD) has been recently used in wind energy research (e.g., Andersen et al., 2013; Meyer et al., 2013; Bastine et al., 2015; Hamilton et al., 2015, 2016). In particular, Bastine et al. (2015) applied the POD technique on large-eddy simulation (LES) data, and they showed that POD can provide useful information related to wake meandering. Indeed, spatially resolved wind tunnel measurements can be used to further examine the applicability of the POD method for wake meandering studies.

In this wind tunnel study, we aim to comprehensively investigate the interaction of a neutrally-stratified turbulent boundary layer with a wind turbine operating under different tip-speed ratios and yaw angles. To achieve this goal, detailed wind tunnel measurements were carried out to study the performance of a model wind turbine as well as the flow field in the upwind, near-wake and far-wake regions. The paper is organized as follows. The experimental setup and incoming flow conditions are presented in Sect. 4.2. Wind turbine characteristics are shown and discussed in Sect. 4.3.1. The flow field upwind of the turbine is presented in Sect. 4.3.2. Mean flow field as well as unsteady vortex structures in the near-wake region are shown and discussed in Sect. 4.3.3. In Sect. 4.3.4, in addition to mean flow characteristics in the far-wake region, the wake meandering is studied. The POD analysis is performed in Sect. 4.3.5. Finally, a summary is provided in Sect. 4.4.

4.2 Experimental setup and incoming flow conditions

The experiment was conducted in the new closed-circuit wind tunnel at the WIRE laboratory of EPFL. The wind tunnel test section designed for boundary-layer flow studies is 28 m long, 2.25 m high, and 2.5 m wide. Due to the long test section of the wind tunnel, a turbulent boundary layer can naturally develop over the floor without using any tripping mechanism. The wind tunnel ceiling was adjusted to ensure that the pressure gradient is zero across the test section. A three-blade model wind turbine, designed and built at the WIRE laboratory, was placed at 22 m downwind of the entrance of the test section. The turbine diameter d and the hub height of the turbine z_h are 15 cm and 12.5 cm, respectively. The very low blockage ratio of the turbine rotor (less than 0.004 with respect to the cross-sectional area of the test section) ensures that the effect of the side walls and the ceiling of the test section on the turbine wake is negligible. The turbine blade profile is a 5% circular arc camber with 5% thickness. The mean incoming velocity at hub height \bar{u}_h is kept constant during measurements at 4.88 ms⁻¹, and its value is used in the remainder of this paper to normalize velocities.

Constant temperature hot-wire (HW) anemometry was used to characterize the incoming boundary-layer profile. The probe consists of a 5.0 μ m tungsten wire that is connected to an A.A. Lab Systems AN-1003 with overheat ratio set to 1.6. Streamwise velocity measurements were performed in a vertical profile starting at z=1.6 cm up to z=47.6 cm with intervals of 1 cm between measurement points (see #1 in Fig. 4.1). At each vertical location, the velocity data were sampled at a rate of 30000 Hz for a period of 60 s. The hot-wire anemometer was calibrated in the free-stream region against a Pitot-static tube at the beginning as well as the end of measurements. Figure 4.2 shows the vertical profiles of the normalized incoming mean streamwise velocity \bar{u}/\bar{u}_h as well as the streamwise turbulence intensity I obtained with hot-wire anemometry. The thickness of the boundary layer δ is approximately 40 cm at the measurement location, so the turbine rotor is within the lowest half of the turbulent boundary layer. In Fig. 4.3(a), a logarithmic profile is fitted to the measured velocity points in the surface

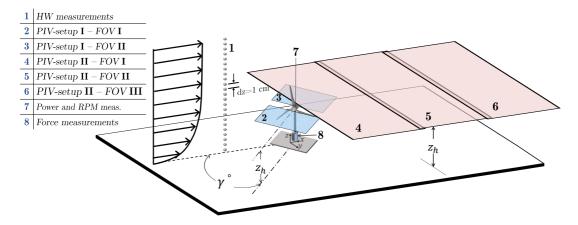


Figure 4.1 – Schematic figure of the different wind tunnel measurements performed in the current study.

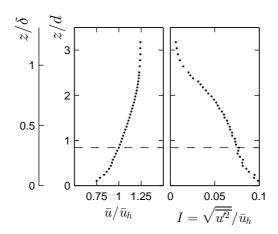


Figure 4.2 – Characteristics of the incoming boundary layer: normalized mean velocity (*left*), turbulence intensity (*right*). The *horizontal-dashed lines* represent the turbine axis.

layer (lowest 15% of the boundary layer) to obtain the friction velocity u_* and the aerodynamic surface roughness length z_0 . Table 4.1 summarizes the key characteristics of the incoming boundary layer as well as the wind turbine dimensions.

The streamwise velocity spectra at different heights normalized with u_* and z are plotted against $k_x z$ in Fig. 4.3(b), where k_x is the wavenumber. As shown in the figure, the curves collapse to a single curve with the change of slope from -1 to -5/3 at $k_x z = 1$, which is expected for a fully-developed turbulent boundary layer (Perry et al., 1986; Porté-Agel et al., 2000).

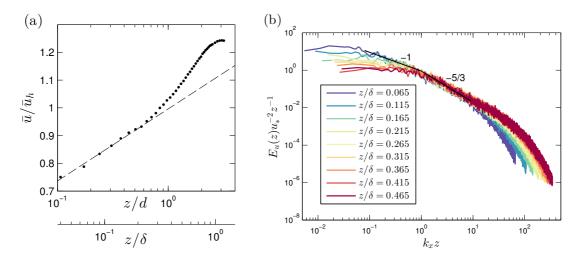


Figure 4.3 – (a) Normalized mean streamwise velocity profile of the incoming boundary layer in a semi-logarithmic scale. The dashed line shows the fitted logarithmic profile. (b) Normalized streamwise velocity spectra $(E_u(z)u_*^{-2}z^{-1})$ versus k_xz at different heights.

δ (cm)	z_0 (mm)	$u_* ({\rm ms}^{-1})$	$\bar{u}_h (\mathrm{ms}^{-1})$	d (cm)	z_h (cm)
40	0.022	0.22	4.88	15	12.5

Table 4.1 – Key characteristics of the incoming boundary layer as well as the wind turbine dimensions.

Two different high-resolution particle image-velocimetry (PIV) setups were employed to acquire detailed flow information. A standard 2-Dimensional, 2-Component (2D2C) PIV from LaVision, termed *PIV-setup I* hereafter, was used to measure streamwise and spanwise velocities in a horizontal plane (xy-plane) at hub height in two fields of view (FOVs) aligned with the turbine rotor; (i) FOV **I**: in front of the turbine (#2 in Fig. 4.1), and (ii) FOV **II**: just behind the turbine (#3 in Fig. 4.1). A 400 mJ dual-head Nd:Yag laser was used to illuminate the horizontal plane. Olive-oil particles generated by the home-made smoke machine were used as tracers for the PIV measurements. A 16-bit sCMOS camera (2560 × 2160 pixels) with a 105 mm lens was used to capture particle images in the laser sheet. The field of view (FOV) and the spatial resolution obtained by this PIV setup are $2d \times 1.7d$ and 0.013d, respectively. Data were sampled at a frequency of 10 Hz. The mean velocity field was obtained by ensemble averaging 1200 instantaneous velocity fields.

In addition to PIV-setup I discussed above, another PIV setup was employed to study the wake of the turbine, with the emphasis on the far-wake region. A stereo PIV system, termed PIV-setup II hereafter, was used to measure three velocity components in three horizontal FOVs (#4, 5 and 6 in Fig. 4.1) at different downwind locations with some overlapping. Large FOVs (each of them with the size of $4d \times 2.5d$) with a high spatial resolution 0.015d were obtained using two 29MP 12-bit CCD cameras (6600×4400 pixels) along with 105 mm lenses installed on Scheimpflug adapters. Data were sampled at a frequency of 1 Hz. The mean velocity field was obtained by ensemble averaging 800 to 1000 instantaneous velocity fields.

In addition to flow measurements, the performance of the turbine is fully characterized in this study. The power P extracted by the turbine from the incoming wind is equal to ΩQ , where Ω is the rotational velocity of the rotor and Q is the torque of the rotor shaft. The mechanical power is then converted to electricity in a DC generator attached to the rotor. For the DC generator, the shaft torque Q can be estimated by $k_M I$, where I is the generated electrical current and k_M is a known constant (Sen, 2007b). The rotational velocity Ω is also measured by the rotary encoder coupled to the DC-generator (#7 in Fig. 4.1). The rotational velocity of the turbine was controlled by changing the electrical load on the DC-generator. Moreover, a multi-axis force sensor was installed at the bottom of the turbine tower to measure the total thrust force T exerted on the turbine by the airflow (#8 in Fig. 4.1).

4.3 results and discussions

4.3.1 Wind turbine performance

Figure 4.4 shows the variation of the thrust coefficient C_T and the power coefficient C_p against tip-speed ratio λ for four different yaw angles $\gamma = 0^{\circ}$, 10° , 20° and 30° . It can be seen in the figure that both the thrust and power coefficients decrease with an increase in yaw angle. In spite of the complex behavior of yawed turbines, the reduction in power and thrust of a yawed turbine is generally explained in the literature in two different simple ways: due to (i) the reduction in the frontal area of a yawed rotor respective to the coordinate system aligned with the incoming flow, or (ii) the reduction of the effective incoming velocity (i.e., the velocity normal to the rotor) based on the coordinate system fixed to the rotor plane. The former suggests that both C_p and C_T are proportional to $\cos \gamma$ but the latter suggests that $C_T \propto \cos^2 \gamma$ and $C_p \propto \cos^3 \gamma$. To better illustrate the dependence of C_p and C_T on the yaw angle, Fig. 4.5(a) shows the reduction of C_P and C_T as a function of $\cos \gamma$ for different tip-speed ratios. For each tip-speed ratio, the values of C_p and C_T are divided by the ones corresponding to the same tip-speed ratio at $\gamma = 0^{\circ}$. Note that, as the horizontal axis of the plot is in a logarithmic scale, any function in the form of $a\cos^b\gamma$, where a and b are constants, is shown by a straight line. For the sake of comparison, the graphs of $\cos^{1.5} \gamma$, $\cos^2 \gamma$ and $\cos^3 \gamma$ are indicated in the figure by dashed, dotted and solid lines, respectively. As shown in the figure, for different tip-speed ratios, the variation of C_T is very similar and is approximately proportional to $\cos^{1.5} \gamma$. For tip-speed ratios close to the optimal one, C_p is approximately proportional to $\cos^3 \gamma$, which is similar to the prediction based on the value of the effective velocity. In general, the variation of C_p , however, largely depends on the operating tip-speed ratio. The value of C_p is reduced far more quickly with an increase in yaw angle if the turbine operates in higher tip-speed ratios. This finding suggests that if a yawed turbine does not work in the optimal tip-speed ratio, operating in higher tip-speed ratios is much worse than that in lower ones.

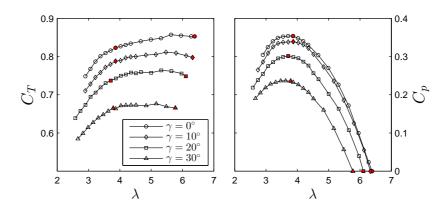


Figure 4.4 – Turbine performance versus tip-speed ratio (thrust coefficient C_T (*left*), and power coefficient C_p (*right*)) for different yaw angles: $\gamma = 0^\circ$ (*circle*), $\gamma = 10^\circ$ (*diamond*), $\gamma = 20^\circ$ (*square*), and $\gamma = 30^\circ$ (*triangle*). For red-coloured points, PIV measurements were performed.

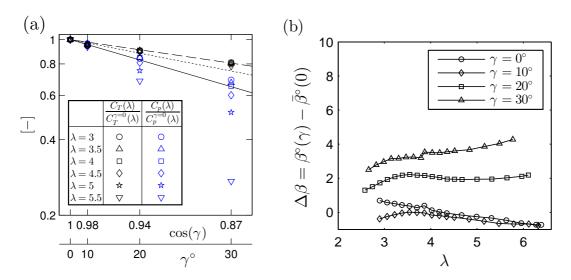


Figure 4.5 – (a) Variation of $C_T(\lambda)/C_T^{\gamma=0}(\lambda)$ and $C_p(\lambda)/C_p^{\gamma=0}(\lambda)$ for different tip-speed ratios versus $\cos \gamma$ in a semi-logarithmic scale. *Dashed*, *dotted* and *solid* lines represent $\cos^{1.5} \gamma$, $\cos^2 \gamma$ and $\cos^3 \gamma$ curves, respectively. (b) Variation of the angle between the net thrust force T and the rotor axis (β°) versus tip-speed ratio λ for different yaw angles.

As mentioned in Sect. 4.1.1, the proper estimation of the direction of the thrust force for yawed turbines is of great importance. Multi-dimensional force measurements performed in this study enabled us to measure the direction of the thrust force for different yaw angles and tip-speed ratios as shown in Fig. 4.5(b). The angle between the net thrust force and the the rotor axis is denoted by β . The value of β averaged over different tip-speed ratios at $\gamma = 0^{\circ}$ (i.e., $\beta(\gamma = 0^{\circ})$) is considered as the reference value for β . The figure shows that the value of $\Delta\beta$ is negligible for $\gamma = 10^{\circ}$ (in the range of $\pm 1^{\circ}$), likely within the measurement uncertainty. However, the difference is bigger for $\gamma = 20^{\circ}$ and $\gamma = 30^{\circ}$ which questions the assumption that the thrust force is exactly normal to the rotor in yawed conditions. The change in the direction of the net thrust force in higher yaw angles can be caused by the asymmetric distribution of the induced velocity for a yawed rotor as suggested by Glauert (1926). In addition, the component of the incoming velocity normal to the nacelle of the turbine (i.e., $u\sin\gamma$) increases with an increase in yaw angle, which in turn increases the drag force exerted on the nacelle. It is worth mentioning that the ratio of the nacelle size to the rotor diameter of wind turbines is much smaller in the field, which might make the effect of the drag force on the nacelle not as significant as the one in the wind tunnel.

For each yaw angle, velocity measurements using both *PIV setups I* and *II* were performed for two different tip-speed ratios: (i) The free-rotating tip-speed ratio λ_f , at which the electrical circuit connected to the DC generator is open and the turbine rotates freely. (ii) The optimal tip-speed ratio λ_o at which the power production is maximum. For each yaw angle, λ_f and λ_o are shown in Fig. 4.4 with red-colored points. These PIV measurements will be used in the following to study the flow characteristics in the three different regions affected by the presence of the turbine: upwind, near-wake and far-wake regions.

4.3.2 Upwind region

Non-yawed turbine

Figure 4.6(a) displays contours of the normalized mean streamwise velocity \bar{u}/\bar{u}_h in the upwind region of the turbine with zero yaw angle at the optimal tip-speed ratio $\lambda = \lambda_o$. In addition, induced velocities in both normal and tangential directions to the rotor are shown by vectors in the figure. Iso-velocity contours shown by *white lines* in the figure indicate a slight lateral asymmetry with respect to the rotor axis. The most possible explanation is that, due to the incoming shear flow, the rotor blades experience a varying angle of attack as they rotate (Hibbs, 1986). This unsteady condition results in a difference in the performance of rotor blades on the two sides of the rotor (the turbine rotates in the counter-clockwise direction seen from upstream). This probably explains why this asymmetric behavior was not observed in previous studies performed in free-stream flows (e.g., Medici et al., 2011). In addition, strong positive and negative tangential induced velocities can be seen in front of the rotor tips. They are associated with the flow expansion which generally occurs in front of bluff and porous objects.

Figure 4.6(b) shows the variation of the normalized mean streamwise velocity in the upwind region along the rotor axis $\bar{u}(x, y=0)/\bar{u}_h$ for PIV measurements as well as vortex theory predictions (Eq. 4.3). As shown in the figure, the agreement is remarkably good for most of the measurement range. This is in contrast with the discrepancies reported by Medici et al. (2011) and Simley et al. (2016) between the predictions made by Eq. 4.3 and their flow measurements.

For the sake of brevity, the upwind region for the turbine at $\lambda = \lambda_f$ is not shown here as it is rather similar to the one for $\lambda = \lambda_o$. The value of C_T is close for these two tip-speed ratios (see

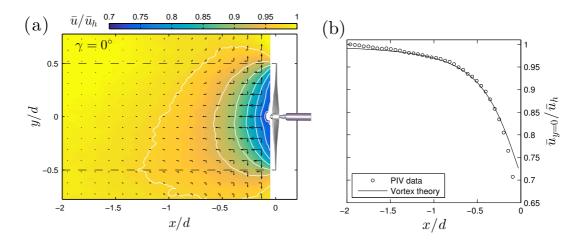


Figure 4.6 – (a) Vectors of mean normal and tangential velocities induced by the turbine with $\gamma = 0^{\circ}$ and $\lambda = \lambda_o$ in the upwind region. The background shows contours of the normalized mean streamwise velocity \bar{u}/\bar{u}_h . While lines are iso-velocity contours, and dashed lines represent the side tips of the rotor. (b) Variation of the mean normalized streamwise velocity in the upwind region along the rotor axis.

Fig. 4.4), and therefore they have a rather similar induced velocity distribution in the upwind region (see Eq. 4.3).

Yawed turbine

Figure 4.7(a) shows contours of the normalized mean streamwise velocity \bar{u}/\bar{u}_h in the upwind region of the turbine with $\gamma=30^\circ$ at $\lambda=\lambda_o$. A strong lateral asymmetry is observed just in front of the yawed turbine. This asymmetry is more obvious in Fig. 4.7(b) that shows the profiles of the normal (i.e., axial) induction factor a for a few upwind positions, where ξ and ζ are the tangential and normal directions to the yawed rotor, respectively. The strong asymmetry, especially in the central part, is partially associated to the increase of the frontal area of the nacelle in yawed case, shown by the shaded area in Fig. 4.7(b). Apart from that, as discussed in Sect. 4.1.2, Glauert (1926) hypothesized that the normal induced velocity on the downwind side of a yawed rotor should be bigger than the one on the upwind side. Both Figs. 4.7(a) and (b) show that for the outer part of the rotor, where the nacelle effect is minimum, Glauert's hypothesis is in agreement with our wind tunnel data. Note also that the sharp decrease in the value of the induction factor at the rotor tips is due to tip losses that has been extensively studied in the literature (e.g., Shen et al., 2005).

Another difference between the upwind region of yawed turbines with the one of non-yawed turbines is that the tangential induced velocity is not normal to the incoming flow in this case. Figure 4.7(a) shows that the tangential induced velocity decelerates the incoming flow on the upwind side and accelerates it on the downwind side of the rotor. As a result, as shown by the contour plot, the streamwise velocity is reduced more in front of the upwind tip of the rotor,

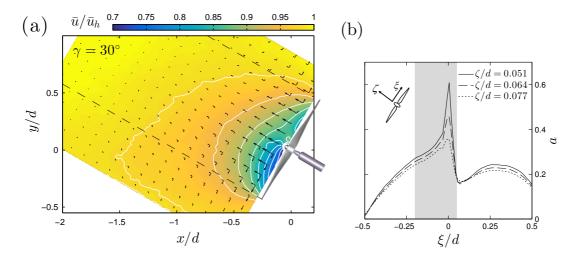


Figure 4.7 – (a) Vectors of mean normal and tangential velocities induced by the turbine with $\gamma=30^\circ$ and $\lambda=\lambda_o$ in the upwind region. The background shows contours of the normalized mean streamwise velocity \bar{u}/\bar{u}_h . While lines are iso-velocity contours, and dashed lines represent the side tips of the rotor. (b) Profiles of the normal induction factor a for different upwind positions. The shaded area indicates the frontal area of the nacelle.

even though the normal induced velocity is smaller there compared with the one in front of the downwind tip. This result stresses the importance of the tangential induced velocity in the upwind region, and generally, in the performance of yawed rotors.

4.3.3 Near-wake region

Mean velocity distribution

Figure 4.8 shows contours of the normalized mean streamwise velocity \bar{u}/\bar{u}_h in the near-wake region for three different cases: a non-yawed turbine operating at the free-rotating tip-speed ratio λ_f , a non-yawed turbine operating at the optimal tip-speed ratio λ_o , and finally a yawed turbine with $\gamma=30^\circ$ operating at the optimal tip-speed ratio λ_o . In general, the figure shows a lateral asymmetry for the near-wake region in all the cases, which is again likely related to the interaction of the rotating blades with the incoming shear flow.

For the turbine with zero yaw angle, a speed-up region is seen just behind the central part of the rotor for both tip-speed ratios, although it is considerably stronger for the higher tip-speed ratio λ_f . This speed-up region is partly associated with the flow expansion occurring around the turbine hub. In addition and more importantly, the angle of attack of the blade airfoil in the central part of the rotor becomes very low or even negative in the case of the higher tip-speed ratio λ_f (Krogstad and Adaramola, 2012), which substantially intensifies the speed-up region in this case. Further downstream, this high velocity region weakens the wake of the nacelle. As a result, the central part of the near-wake region seems weaker for the higher tip speed-ratio λ_f although the value of C_T shown in Fig. 4.4 is slightly higher in this case. It is also worth recalling that the central part of the rotor does not make a significant contribution to the overall thrust force compared to outer part due to large differences in their swept areas.

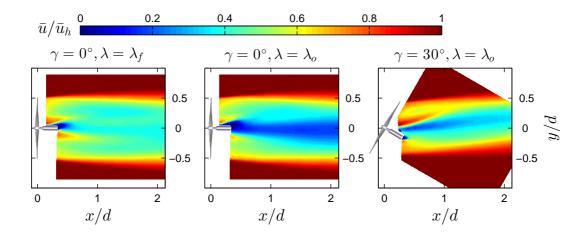


Figure 4.8 – Contour plots of the mean normalized streamwise velocity \bar{u}/\bar{u}_h in the near-wake region for different turbine operating conditions.

For the yawed turbine, the figure shows that the presence of the nacelle profoundly affects the central part of the near wake. It can be again explained by the increase in the frontal area of the nacelle for a yawed turbine compared with the case of zero yaw.

Dynamic characteristics

Instantaneous flow fields in the near-wake region can be studied to provide more insights into the dynamic characteristics of the near-wake region. Figure 4.9 shows contours of the instantaneous out-of-plane vorticity ω_z , non-dimensionalized with \bar{u}_h and d, for three different operating conditions. For each case, three randomly chosen instantaneous vorticity fields are shown in the figure.

As shown in the figure for the non-yawed case, the tip vortices are more distant from each other, stronger and persist longer in the optimal condition (i.e., $\lambda = \lambda_o$) compared with the other case. Firstly, one can simply show that the distance between two consecutive tip vortices, called helix pitch, is inversely proportional to the tip-speed ratio and can be approximated by $\pi d/(3\lambda)$ (Chamorro et al., 2013b). Secondly, the tip vortices for λ_o are stronger due to the higher lift to drag ratio, and consequently a higher pressure difference between the suction and

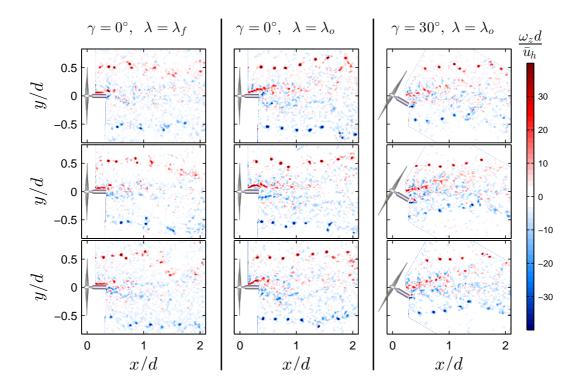


Figure 4.9 – Contours of the instantaneous out-of-plane vorticity ω_z , non-dimensionalized with \bar{u}_h and d, for different turbine operating conditions.

pressure sides of the blade airfoils in this case. Note that the pressure difference between the two sides of the blade airfoil at the tip is considered as the formation mechanism of tip vortices (Yang et al., 2012). Finally, the fact that tip vortices persist longer for λ_o can be explained by considering the mutual inductance instability, which is the most dominant mode of instability for helical vortex filaments (Felli et al., 2011). This instability is intensified by the decrease in the helix pitch, and it leads to the pairing and breakdown of helicoidal tip vortices (Widnall, 1972; Sarmast et al., 2014; Sherry et al., 2013b,a), as clearly seen in the figure for the case of higher tip-speed ratio λ_f . In addition to tip vortices, high vorticity regions in the center of the near wake are observed for all the operating conditions, which are related to the root and hub vortices as well as the boundary layer around the nacelle (Zhang et al., 2012).

For the yawed case, the tip vortices are seen to be less pronounced compared with the ones for the non-yawed turbine. This can be again explained by considering that the pressure difference between the two sides of the blade airfoil is likely to be lower for the yawed turbine, which results in weaker vortices shedding from the tip of the blades.

As mentioned in Sect. 4.1.3, phase-locked PIV measurements have been carried out in previous studies to visualize the mean flow field for a given position of the rotating blades. In this study, PIV measurements were freely performed and not synchronized with the azimuthal angle of the rotor blades. Therefore, a post-processing technique similar to the ones used in previous studies (e.g., Tobin et al., 2015) is employed here to calculate phase-averaged flow fields in the near-wake region. This technique can be summarized as follows. First, an arbitrary position just behind one of the blade tips is chosen as the reference position for the phase averaging. The averaging is then performed only over the instantaneous fields for which the reference position coincides with the center of a tip vortex. In order to find the location of tip vortices with respect to the reference position, the swirling strength λ_{ci} is determined within a search window around that position. The swirling strength λ_{ci} is the imaginary part of the complex eigenvalue pair of the velocity gradient tensor (Chakraborty et al., 2005). Within the search window, the maximum value of the swirling strength λ_{ci} indicates the location of the tip vortex. Note that the width of the search window is chosen slightly smaller than the helix pitch to ensure that one (and no more than one) tip vortex is always inside the window. It is worth mentioning that the benefit of using the swirling strength λ_{ci} over the out-of-plane vorticity ω_z is that it only detects high vorticity regions due to locally vortical structures, not due to shear flows. See Zhou et al. (1999) for more information on vortex identification methods.

Figure 4.10 shows contours of the phase-averaged out-of-plane vorticity $\bar{\omega}_z$, non-dimensionalized with \bar{u}_h and d, for the three different operating conditions. A slight tolerance (equal to the measurement resolution 0.013d) is permitted for the coincidence of tip vortices with the reference position, in order to ensure that sufficient instantaneous fields (at least 120 samples for each operating condition) are found for the phase averaging. The search windows are shown by black rectangles in the figure while the reference position is placed at the center of the rectangle.

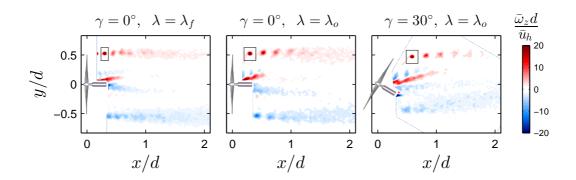


Figure 4.10 – Contours of the phase-averaged out-of-plane vorticity $\bar{\omega}_z$, non-dimensionalized with \bar{u}_h and d, for three different operating conditions.

Comparison of the phase-averaged contours with the instantaneous ones reveals that they substantially underestimate the downwind distance at which the breakdown of tip vortices occurs. For instance, based on the phase-averaged contours, the tip vortices for the non-yawed turbine persists no more than one rotor diameter downwind of the turbine for both tip-speed ratios, whereas the instantaneous fields (Fig. 4.9) show that the breakdown of tip vortices occurs much further downstream, particularly for the case of $\lambda = \lambda_o$. This smoothing feature of the phase averaging is known to be associated with the vortex wandering which denotes the random fluctuation of vortices around their statistically-averaged positions, seen in the instantaneous fields of Fig. 4.9. Prior studies (e.g., Heyes et al., 2004; Yang et al., 2012; Sherry et al., 2013a) reported that the amplitude of vortex wandering increases with the vortex age and, consequently, the smoothing effect on phase-averaged contours is more obvious for further downwind positions (Dobrev et al., 2008). In particular, the boundary-layer turbulence substantially amplifies vortex wandering (Beresh et al., 2010), which in turn intensifies the smoothing effect seen in phase-averaged contours. This discussion highlights the important fact that phase-locked measurements are not able to accurately predict the breakdown of tip vortices, especially in boundary-layer inflow conditions.

The vortices shedding from the root of the blades are clearly evident in phase-locked contours (Fig. 4.10) although they cannot be easily distinguished in some of the instantaneous contours (Fig. 4.9). In other words, phase-locked averaging seems to be more useful to visualize root vortices rather than tip vortices. One possible explanation for this difference is that root vortices, unlike tip vortices, are not directly influenced by the meandering motion of VLSMs in the outer flow (see Sect. 4.3.4 for the detailed discussion on VLSMs). The wandering motion and its smoothing effect on phase-averaged contours are therefore expected to be less significant for root vortices.

It is also worth mentioning that the root vortices shedding from the downwind side of the yawed rotor seem to persist more than the ones for the non-yawed rotor. This is probably due to the fact that the root vortices for the downwind side of the yawed rotor are more distant from the nacelle boundary layer, which acts as a mechanism to destabilize root vortices (Sherry

et al., 2013b). Moreover, note that the tips of a yawed rotor on the two sides are located at different streamwise positions, so the breakdown of tip vortices for the upwind side is obviously expected to occur further upstream.

4.3.4 Far-wake region

Mean velocity distribution

The effect of the yaw angle on the far-wake velocity distribution is extensively documented in a recent study of the authors (Bastankhah and Porté-Agel, 2016); therefore, only the effect of tip-speed ratio is discussed in this section for the sake of brevity. Figure 4.11 shows profiles of the normalized mean streamwise velocity \bar{u}/\bar{u}_h for a non-yawed turbine at selected downwind locations for two different tip-speed ratios. Unlike the near-wake region, the wake of the turbine in the far-wake region $(x/d \gtrsim 3)$, which is less sensitive to rotor dynamics, is similar for the two considered tip-speed ratios and, as expected, the lateral velocity profiles have approximately a Gaussian distribution. In addition, the figure shows that the velocity deficit in the far-wake center is slightly smaller for the optimal tip-speed ratio λ_0 despite having higher velocity deficit in the near-wake center. Due to the higher velocity gradient in the near-wake center for $\lambda = \lambda_0$, the flow entrainment becomes higher in the center of the near wake for this tip-speed ratio as shown by contours of the normalized lateral turbulent shear stress $\overline{u'v'}/\bar{u}_h^2$ in Fig. 4.12. As a result, the wake center for $\lambda = \lambda_0$ recovers faster and ultimately the velocity deficit in the far-wake center becomes slightly smaller in this case. This is consistent with the thrust measurements as C_T is found to be slightly lower for the optimal tip-speed ratio λ_o (see Fig. 4.4).

In general, this discussion confirms the known fact that, although the overall thrust coefficient along with incoming boundary-layer conditions can represent general characteristics of far-

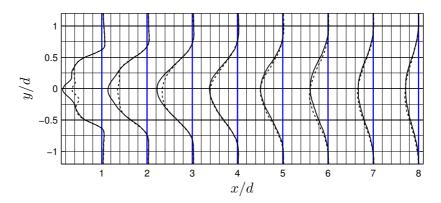


Figure 4.11 – Profiles of the normalized mean streamwise velocity \bar{u}/\bar{u}_h downwind of a non-yawed turbine at different downwind locations for different tip-speed ratios: optimal tip-speed ratio λ_o (solid lines), and free-rotating tip-speed ratio λ_f (dashed lines). For each downwind location, $\bar{u}=\bar{u}_h$ on the vertical thick blue lines. The width of grid squares corresponds to 17% of \bar{u}_h .

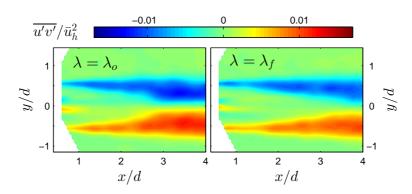


Figure 4.12 – Contours of the normalized lateral turbulent momentum flux $\overline{u'v'}/\bar{u}_h^2$ downwind of the turbine with zero yaw angle for two different tip-speed ratios: the optimal tip-speed ratio λ_o (*left*), and the free rotating tip-speed ratio λ_f (*right*).

wake regions (Crespo et al., 1999), it is not sufficient for near-wake predictions. Detailed information regarding rotor characteristics such as the operating tip-speed ratio, the blade geometry and the twist distribution is needed to systematically analyze and predict this very complex region.

Note also that for the higher tip-speed ratio λ_f , the wake is slightly deflected to one side. This might be due to: (i) the asymmetric distribution of loads on the rotor caused by the interaction of rotating blades with the incoming shear flow, (ii) the interaction between the rotating wake and the incoming boundary layer as reported by Fleming et al. (2014), (iii) measurement uncertainties, or the combination of all of the above-mentioned factors. However, the authors cannot strictly comment on the origin of this deflection at this stage, and more studies are needed to unravel it.

The transition from the near wake to the far wake has been investigated in previous studies (e.g., Vermeulen, 1980; Sørensen et al., 2015). Tip vortices in the near-wake region are generally assumed to act as a shield (Lignarolo et al., 2013), so that they prevent the entrainment of the outer flow into the wake. After the breakdown of tip vortices, the flow entrainment substantially increases until a self-similar Gaussian velocity profile is attained in the onset of the far-wake region. Sørensen et al. (2015) used this explanation to predict the downwind location where the far-wake region begins. According to this explanation, given the same incoming flow conditions, a faster breakdown of tip vortices results in a shorter near wake. However, our wind-tunnel measurements reveal that this is not necessarily always the case. Figure 4.11 shows that a Gaussian velocity profile is attained earlier for $\lambda = \lambda_0$ although the breakdown of tip vortices happens first for $\lambda = \lambda_f$ as clearly shown in Fig. 4.9. It seems that, in addition to the breakdown of tip vortices, the initial velocity profile in the near wake imposed by the load distribution on the rotor affects where a Gaussian velocity profile is attained. For instance, near-wake velocity profiles for the higher tip-speed ratio λ_f are more similar to a top-hat profile due to the speed-up region discussed in Sect. 4.3.3. As a consequence, more distance is needed to attain a Gaussian velocity profile, although the breakdown of tip vortices occurs earlier for this tip-speed ratio. In order to accurately predict the near-wake length, this finding suggests that one should also consider the velocity distribution in the near-wake region.

Wake meandering

VLSMs and their interaction with wind turbines: In order to provide a deeper understanding on wake meandering, as mentioned in Sect. 4.1.4, it is crucial to study the characteristics of very-large-scale motions (VLSMs) in the boundary layer and their interaction with wind turbines. Figure 4.13(a) shows the pre-multiplied spectrum scaled with u_*^2 ($k_x\Phi_{uu}/u_*^2$) for the incoming streamwise velocity fluctuation at the rotor hub height as a function of the streamwise wavelength λ_x . Note that Taylor's hypothesis (frozen convection) is used to reconstruct the data in the streamwise direction from the temporal information obtained with single-point hot-wire measurements. As previously used by Guala et al. (2006) and Balakumar and Adrian (2007), structures with $\lambda_x > 2\delta$ in the pre-multiplied spectrum are considered as VLSMs. The figure shows a peak at $\lambda_x \approx 5\delta$ (i.e., $\lambda_x \approx 13d$) corresponding to VLSMs. It is also worth mentioning that a spectral gap can be seen between VLSMs and large-scale motions (i.e., low frequency motions with $\lambda_x < 2\delta$) which is in agreement with previous studies (e.g., Balakumar and Adrian, 2007; Fang and Porté-Agel, 2015). VLSMs in the boundary layer can be also revealed by the autocorrelation of the streamwise velocity fluctuation ρ_{uu} which is defined as

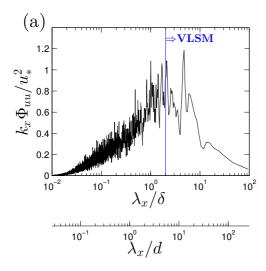
$$\rho_{uu}(\tau) = \frac{\overline{u'(t)u'(t-\tau)}}{\overline{u'(t)^2}},\tag{4.4}$$

where primes indicate turbulent fluctuations, and the overbar denotes ensemble averaging. Figure 4.13(b) shows profiles of ρ_{uu} for the incoming boundary layer at different heights. As shown in the figure, the correlation is around 0.1 at $\pm 1\delta$ (i.e., $\approx \pm 3d$), which again indicates the presence of very long structures in the boundary layer.

In order to estimate the length of VLSMs, as discussed earlier, we applied Taylor's hypothesis to single-point hot-wire measurements. However, this method provides no information about the size of VLSMs in other directions (e.g., width of VLSMs). We therefore use the PIV data to calculate the two-point correlation of the streamwise velocity fluctuation R_{uu} , which is an indicative of the spatial coherence in different directions. The value of $R_{uu}(x, y)$ with respect to a given reference position (x_{ref}, y_{ref}) is calculated by

$$R_{uu}(x,y) = \frac{\overline{u'(x_{ref}, y_{ref})u'(x,y)}}{\sqrt{\overline{u'(x_{ref}, y_{ref})^2 \times \overline{u'(x,y)^2}}}}.$$
(4.5)

Figure 4.14 shows contours of R_{uu} for two arbitrarily-chosen reference positions upwind of the turbine. For each contour plot, the corresponding reference position is shown by a *white plus* sign. As seen in the figure, the correlated region is laterally surrounded by anti-correlated



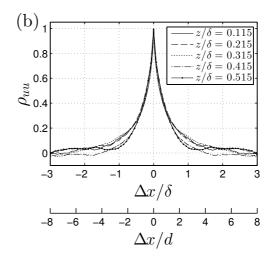


Figure 4.13 – (a) Non-dimensionalized pre-multiplied spectrum $k_x\Phi_{uu}/u_*^2$ of the incoming streamwise velocity at hub height versus the streamwise wavelength λ_x . (b) Auto-correlation of the streamwise velocity fluctuation ρ_{uu} for the incoming boundary layer at different heights.

regions. This reflects the presence of the lateral strip of high- and low-momentum regions in the turbulent boundary-layer flow (Lee and Sung, 2011). Moreover, the figure shows that even though the correlated region exceeds the streamwise extent of the FOV, it has a width just in the order of the turbine rotor diameter (i.e., $\approx 0.4\delta$). This is in agreement with previous studies (e.g., Hutchins and Marusic, 2007) showing that VLSMs in boundary-layer flows are streaks elongated in the streamwise direction, and they are of the order $0.3-0.5\delta$ wide. This points to the important fact that although very long structures exist in boundary-layer flows, their width is comparable to the size of the turbine rotor (at least the same order of magnitude). These long structures can be thus altered due to the presence of the rotor, and as clearly seen in the contour plots of Fig. 4.14, the spatial coherence abruptly decreases as the flow approaches the turbine. In fact, this questions the validity of the assumption that turbine wakes can be considered as passive tracers, which is commonly used in dynamic wake meandering models suggested by Larsen et al. (2008). The effect of this rather unrealistic assumption on the accuracy of the wake-meandering prediction is out of the scope of this current study but, indeed, it deserves further attention in future studies.

Next, the spatial coherence in the wake of the wind turbine is investigated. Figure 4.15 shows contours of R_{uu} in the wake of the turbine for different reference positions (x_{ref}, y_{ref}) . For the contour plots in the first row of the figure $y_{ref} = 0$, and for the ones in the second row $y_{ref} = -d/2$. The contour plots in each column correspond to the same x_{ref} as shown in the figure by *white plus* signs. The two contour plots corresponding to the very near-wake region $(x_{ref} = 1d)$ show that the spatial coherence is small in this region, and the flow is mostly influenced by the shear layer around the nacelle and probably the hub vortex as suggested by previous studies (e.g., Jungo et al., 2013). In addition, it can be seen that the correlated region in the wake center increases as the reference position is chosen further downstream, which is

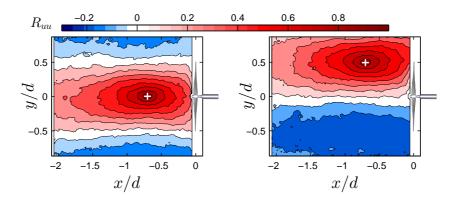


Figure 4.14 – Contours of the two-point correlation of the streamwise velocity fluctuation R_{uu} in the upwind region of the turbine with $\gamma = 0^{\circ}$ and $\lambda = \lambda_o$ for two different arbitrarily-chosen reference positions: $x_{ref} = -0.7d$ and $y_{ref} = 0$ (left), and $x_{ref} = -0.7d$ and $y_{ref} = -0.5$ (right).

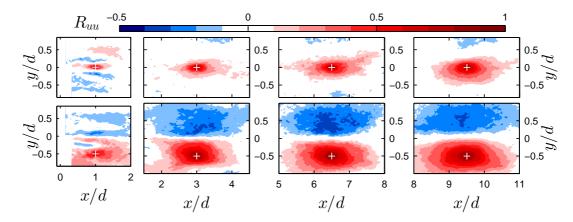


Figure 4.15 – Contours of the two-point correlation of the streamwise velocity fluctuation R_{uu} for different downwind locations. The turbine operates at $\gamma = 0^{\circ}$ and $\lambda = \lambda_o$. For each contour plot, the respective reference position (x_{ref}, y_{ref}) is indicated by a *white plus* sign.

similar to the variation of the integral time scale in the wake of a hydrokinetic turbine reported by Chamorro et al. (2013a). A strong anti-correlated region can be also seen for contour plots provided $y_{ref} = -0.5d$ (i.e., the plots in the second row of Fig. 4.15).

The question then arises of whether the positive and negative correlated regions in the turbine wake seen in Fig. 4.15 correspond to the so-called large-scale turbulent eddies, similar to what already seen for the incoming boundary layer. The answer to this question is negative. In fact, it will be shown in the following that the specific distribution of the spatial coherence seen in turbine wakes is mostly generated due to the wake meandering. The value of the wake velocity deficit is generally comparable to the magnitude of the turbulent fluctuations in the ambient flow, except in very far-wake regions. Thus, the meandering motion of the wake generates an excess streamwise velocity fluctuation that masks fluctuations caused by

large-scale turbulent structures. This can be clearly seen in Fig. 4.16 that shows contours of the instantaneous streamwise velocity field u and its fluctuation component $u' = u - \bar{u}$, both normalized with \bar{u}_h . In the following, we show that the general distribution of R_{uu} already seen in Fig. 4.15 can be described with the sole consideration of the wake meandering. Figure 4.17 displays a schematic figure of the wake meandering for two different time instances. As shown in the figure, the correlation of the streamwise velocity fluctuation between the wake center (point B) and the wake side (either points A or C) changes from positive to negative at different time instances depending on the instantaneous location of the wake. As a result, the ensemble-averaged correlation between point B with either points C or A tends to zero (i.e., $u'_R u'_A = u'_R u'_C = 0$) which is in agreement with the distribution of R_{uu} shown in Fig. 4.15 for $x_{ref} \ge 3$. The correlation between points on the opposite sides of the wake (points A and C) is, however, always negative regardless of the instantaneous position of the wake, and thus $u'_{C}u'_{A} < 0$. In addition to our PIV data (Fig. 4.15), this negative correlation has been reported by the simultaneous measurements of two hot-wire probes performed in the wake of a porous disk by España et al. (2012). As the wake moves downstream (e.g., at point B' in Fig. 4.17), the wake grows and also the magnitude of the wake meandering increases, so the spatial coherence expands which is again in agreement with the contour plots of R_{uu} in Fig. 4.15.

Even though single-point statistics of the streamwise velocity fluctuation have been used in the literature (e.g., Chamorro et al., 2012, 2013a; Barlas et al., 2016) to describe the size or the energy of the large-scale turbulent eddies in turbine wakes, this finding reveals that coherent structures indicated by these techniques are mostly generated just due to the wake meandering. Hutchins and Marusic (2007) showed that in general the meandering motion yields an underestimation in the prediction of the energy and size of very-large-scale structures in boundary-layer flows. In wake flows, however, we show that the meandering motion has a far more profound effect. Unlike boundary-layer flows, flow downwind of the turbine is not

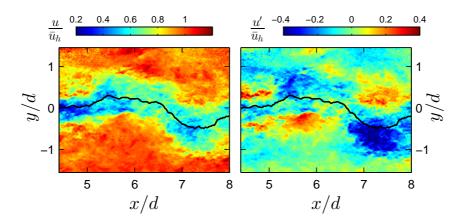
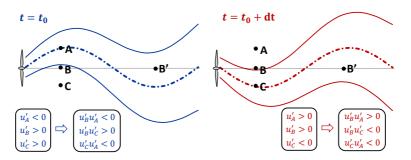


Figure 4.16 – Contours of the instantaneous streamwise wake velocity u (*left*) and its fluctuation component $u' = u - \bar{u}$ (*right*), both normalized with \bar{u}_h . Solid black lines represent the instantaneous wake center position calculated by Eq. 4.6.



 $Figure\ 4.17-Schematic\ figure\ of\ the\ wake\ meandering\ at\ two\ different\ time\ instances.$

horizontally homogenous (i.e., difference in ambient and wake velocities), therefore the wake meandering fundamentally affects the distribution of the streamwise velocity fluctuation, and consequently all the statistical information based on that.

Effect of turbine operating conditions on wake meandering: Next, we study the effect of turbine operating conditions (different tip-speed ratios and yaw angles) on the magnitude of the wake meandering. To do so, the wake-center trajectory for each instantaneous velocity field should be first determined. At each downwind location, the instantaneous position of the wake center y_c is computed as:

$$y_c = \frac{\int (\bar{u}_h - u)^2 y \, dy}{\int (\bar{u}_h - u)^2 \, dy}.$$
 (4.6)

As an example, the position of the wake center determined by Eq. 4.6 can be seen in Fig. 4.16 for an instantaneous flow field. It is worth mentioning that different definitions of the wake-center position (e.g., the one suggested by Bastine et al., 2015) were checked by the authors. Based on the visual inspection of several instantaneous velocity fields, Eq. 4.6 was found to provide a slightly better estimation of the wake center.

Figure 4.18 shows the standard deviation of the wake center position normalized with the rotor diameter for different yaw angles ($\gamma=0^\circ,10^\circ,20^\circ$ and 30°), and different tip-speed ratios ($\lambda=\lambda_o$ and λ_f). The standard deviation of the wake center position is an indicator of the wake meandering magnitude at each streamwise position. The figure clearly shows that the magnitude of the wake meandering is almost identical for different operating conditions which in turn supports the hypothesis that the magnitude of the wake meandering mostly depends on incoming boundary-layer characteristics rather than turbine operating conditions. It is also worth mentioning that the wake meandering magnitude is observed to increase approximately linearly with an increase in downwind distance which is in agreement with the LES results of Abkar and Porté-Agel (2015).

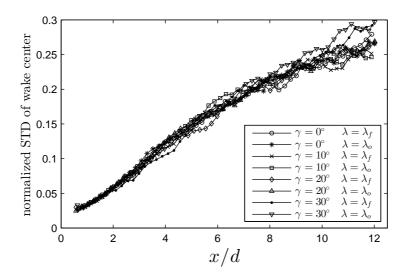


Figure 4.18 – Standard deviation of the wake-center position normalized with the rotor diameter d for different turbine operating conditions.

4.3.5 POD analysis

In order to study dynamic features of turbine wakes with PIV data, both spatial and temporal information of the flow field has to be analyzed. It means that one has to deal with the velocity information in N different instantaneous flow fields (i.e., temporal information), where each of them contains M measured points in the PIV plane (i.e., spatial information). As a powerful tool, the proper orthogonal decomposition (POD) can be used to provide a low-dimensional approximation of this high-dimensional problem, optimized for capturing the most energetic structures of the flow field (Berkooz et al., 1993). Since $M \gg N$ for the experimental data, the method called *snapshot POD* suggested by Sirovich (1987) is used here due to its lower computational cost. Based on this method, each instantaneous PIV measurement is considered as a flow snapshot. As experimental data are always a finite-dimensional case, the POD simply reduces to a singular value decomposition (SVD) of the given dataset (Holmes et al., 1998).

The mathematical procedure for applying the POD method on the PIV data will be briefly explained in the following (see Chatterjee, 2000; Tropea et al., 2007, for detailed information). The fluctuations of the three velocity components (u', v', w') from N snapshots are arranged in the matrix V with an $N \times 3M$ size as follows (Meyer et al., 2007)

$$V = \begin{pmatrix} u'_{11} & \cdots & u'_{1M} & v'_{11} & \cdots & v'_{1M} & w'_{11} & \cdots & w'_{1M} \\ u'_{21} & \cdots & u'_{2M} & v'_{21} & \cdots & v'_{2M} & w'_{21} & \cdots & w'_{2M} \\ \vdots & \ddots & \vdots & \vdots & \ddots & \vdots & \vdots & \ddots & \vdots \\ u'_{N1} & \cdots & u'_{NM} & v'_{N1} & \cdots & v'_{NM} & w'_{N1} & \cdots & w'_{NM} \end{pmatrix}, \tag{4.7}$$

where the i-th row of the matrix V corresponds to the i-th snapshot and i changes from 1 to

N. For each snapshot, the fluctuating velocity components of all the measurement points in the PIV plane are sequentially placed in one row of the matrix V. The SVD form of the matrix V is then

$$V = A\Sigma\Phi^T,\tag{4.8}$$

where Φ is an $3M \times 3M$ orthogonal matrix whose columns are the vectors of the POD modes ϕ , A is an $N \times N$ orthogonal matrix whose columns are the vectors of POD coefficients with a one-to-one correspondence with the POD modes ϕ . The matrix Σ is an $N \times 3M$ diagonal matrix whose diagonal elements consist of the singular values σ of the matrix V in a descending order $(\sigma_1 \geq \sigma_2 \geq ... \geq \sigma_N \geq 0)$. Note that the amount of the turbulent kinetic energy contained in a given POD mode is proportional to the square of the corresponding singular value (Chatterjee, 2000), and thus the first POD modes are the most important ones in terms of energy. By post-multiplying Eq. 4.8 with its transpose, the SVD problem is converted to a eigenvalue decomposition problem as

$$VV^T = A\Sigma^2 A^{-1}. (4.9)$$

Therefore, the eigenvalues of VV^T sorted in a descending order are the square of singular values (i.e., $\sigma_1^2, \sigma_2^2, ..., \sigma_N^2$), and the eigenvectors of VV^T arranged with respect to the corresponding eigenvalues are the POD coefficients. From Eq. 4.8, the POD modes ϕ are then simply equal to the rows of the matrix $\Sigma^{-1}A^TV$. The last step is to just reshape POD modes from 1D arrays into 2D arrays corresponding to the measurement points in the PIV plane.

We apply the POD method on the flow data obtained with the *PIV-setup II* for three different horizontal FOVs at hub height. A preprocessing method similar to the one used by Bastine et al. (2015) is also employed to reduce the effect of the incoming flow unsteadiness on the POD modes. According to this method, for a given downwind location, we set all the values of the velocity deficit lower than 20% of the maximum value equal to zero. Figure 4.19 shows the first six POD modes for the three different FOVs. Vectors represent the in-plane components of the POD modes (i.e., ϕ_u and ϕ_v) in the figure, and contour plots represent only their streamwise component (i.e., ϕ_u). Although the same color scaling is used for all the contour plots, the color bar is intentionally not shown in the figure as the POD modes without the respective coefficients do not contain quantitative physical information (Hamilton et al., 2015). The percentage value seen on each contour plot shows the value of the energy related to the plotted POD mode with respect to the total energy. Note that although the data shown in Fig. 4.19 is limited to the non-yawed turbine with $\lambda = \lambda_o$, qualitatively similar results are seen for other considered operating conditions.

For the near-wake region (i.e., FOV I), the shear layers caused by tip vortices as well as hub/root vortices are seen in some of the POD modes, e.g., modes 2, 3, 5 and 6. It is noteworthy to mention that these two shear layers merge together at around 2–3 rotor diameters downstream of the turbine. For further downwind distances, it seems that the first two modes are pair

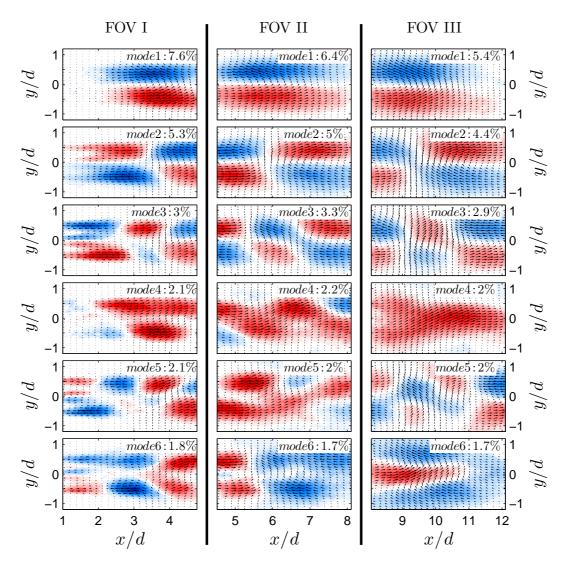


Figure 4.19 – Vectors of streamwise and spanwise components of the first six POD modes ϕ_u , ϕ_v for three different FOVs in the wake of the turbine operating at $\gamma=0^\circ$ and $\lambda=\lambda_o$. The background shows the contour plot of the streamwise component of POD modes ϕ_u . The turbine operates at $\gamma=0^\circ$ and $\lambda=\lambda_o$.

modes, and therefore, they most likely represent the two phases of a identical large-scale lateral motion of the wake. Note that the apparent inconsistency in the sign of modes belonging to different FOVs (e.g, the second mode for FOV II and FOV III) is resolved once the modes are multiplied by the respective POD coefficients (Hamilton et al., 2016).

In addition, it is interesting to note that the first three modes contain distinct dipole structures, which imply that these modes are responsible for periodic lateral motions. The wavelength of the periodic motion induced by each of these modes is twice the streamwise distance between consecutive negative and positive poles, and the amplitude of this periodic motion is equal to

the lateral distance between positive and negative poles. The current PIV measurements are not fast enough to see whether there is any connection between these POD modes and the periodic vortex shedding of the wake with the specific frequency reported by previous studies (e.g., Okulov et al., 2014)). In future studies, time-resolved measurements will be performed to study the temporal variation of the corresponding POD coefficients in the frequency domain.

The forth mode and the following ones have more complex and irregular distributions which are likely to account for: (i) random non-periodic lateral motions of the wake, (ii) the vertical meandering of the wake, or (iii) variation in the magnitude of the velocity deficit due to the low- and high-momentum structures in the incoming boundary layer.

Figure 4.20(a) shows the variation of the energy for the first 100 POD modes in three different considered FOVs. As seen in the figure, although the energy of the first two modes depends on the location of the FOV, the value of the energy for higher mode numbers is almost identical for different FOVs. This is expected as the first modes contain larger coherent structures that basically change as the wake moves downstream. In contrast, higher modes are associated with smaller turbulent scales that are unlikely to experience a significant change by moving downstream.

Moreover, the energy value is seen to decay rather slowly for all the three different FOVs. This can be easier seen in Fig. 4.20(b) which shows the sum of the energy in percentage for a given number of successive modes. The figure shows that the first 100 modes contain only about 55% of the total turbulent kinetic energy of the flow as the flow is fully turbulent. It therefore points out that the normal POD-based reduced-order modeling (ROM), without the consideration of closure models, is not useful in this case (Burkardt et al., 2006). Nonetheless, a few modes might be still able to approximate the general features of the wake. Figure 4.21 shows the approximated instantaneous velocity field reconstructed by the first 3 POD modes, 10 POD modes and 100 POD modes. The original instantaneous velocity field is already shown

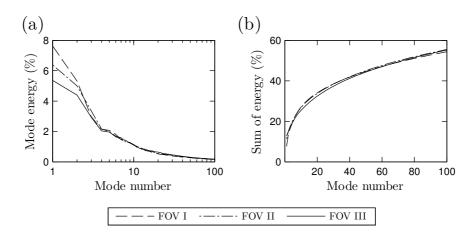


Figure 4.20 - (a) Energy of the first 100 POD modes for three different FOVs of *PIV-setup II* in a semi-logarithmic scale. (b) Sum of the energy for a given number of successive POD modes.

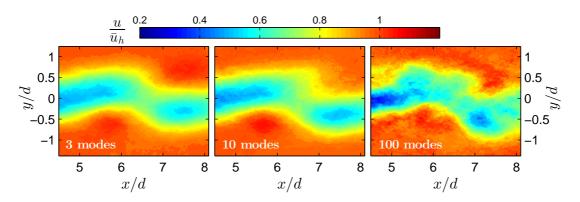


Figure 4.21 – The approximated instantaneous velocity field reconstructed by the first: 3 POD modes (*left*), 10 POD modes (*middle*) and 100 POD modes (*right*). The original instantaneous flow field is shown in Fig. 4.16.

in Fig. 4.16. As seen in the figure, the low-rank approximation of the velocity flow field with only the first three modes containing 15% of total energy can fairly well predict the wake center trajectory although it cannot provide detailed information about wake characteristics. This confirms the conclusion drawn by Bastine et al. (2015) that general features of turbine wakes such as the wake center trajectory can be captured with the use of first a few POD modes.

4.4 Summary

Wind tunnel experiments were performed to comprehensively study the interaction of a turbulent boundary layer with a model wind turbine operating under different tip-speed ratios and yaw angles. In these experiments, a three-blade horizontal-axis wind turbine was placed in a neutrally-stratified boundary layer generated in the recirculating wind tunnel at the WIRE Laboratory of EPFL. We carried out high-resolution PIV experiments to quantify the flow in the horizontal plane at hub height covering a broad streamwise range from 2 rotor diameters upstream of the turbine to 12 rotor diameters downstream. HW measurements were also performed to characterize the incoming boundary layer. In addition, power and thrust force measurements were carried out to study wind turbine performance under different conditions. The main conclusions of this study are summarized in the following.

(i) Wind turbine performance: The measurements reveal that the variation of C_T as a function of yaw angle is similar for different tip-speed ratios. However, the reduction of C_p for a yawed turbine depends on the operating tip-speed ratio, and it is considerably more for higher tip-speed ratios. Moreover, the results suggest that, although the thrust force can be considered perpendicular to the rotor for lower yaw angles, the assumption of perpendicularity is moderately violated for higher yaw angles.

(ii) *Upwind region*: In this region, vortex theory is found to acceptably predict the streamwise velocity along the rotor axis of the turbine with zero yaw angle. In addition, the flow in front of

the turbine is slightly asymmetric, which is likely to be caused by the interaction of the rotating blades with the incoming shear flow. For a yawed turbine, a strong lateral asymmetry is, however, observed in the upwind region. That is partly related to the asymmetric distribution of the induced velocity for yawed rotors, as suggested by Glauert (1926).

- (iii) Near-wake region: For the higher tip-speed ratio λ_f , a distinct speed-up region exists behind the central part of the rotor which makes the center of the near wake less pronounced in this case, despite having a slightly higher C_T compared with the case of optimal tip-speed ratio λ_o . Instantaneous vorticity fields suggest that tip vortices are stronger, more distant and more stable for the optimal tip-speed ratio λ_o . Due to the wandering smoothing effect, the phase-averaged techniques are clearly unable to determine the downwind location where the breakdown of tip vortices occurs. For root vortices, however, the smoothing effect in the phase-averaged data seems to be limited as the vortex wandering is less in this case.
- (iv) *Far-wake region*: As expected, lateral profiles of the wake velocity have a self-similar Gaussian distribution, and also the velocity deficit at the wake center is higher for turbines with higher thrust coefficients C_T . Moreover, we found that the faster breakdown of tip vortices does not necessarily lead to the earlier occurrence of self similarity. In fact, the results suggest that the initial velocity distribution in the near-wake region also has to be considered in order to predict where velocity profiles attain self similarity.
- (v) *VLSMs* and wake meandering: Single-point statistics as well as the two-point correlation of the streamwise velocity fluctuation in the incoming boundary layer confirm the existence of very-large-scale motions (VLSMs) in the form of alternating low- and high-momentum streaks. Although VLSMs are elongated in the streamwise direction, their width is of the same order of magnitude of the rotor size. The presence of the rotor is therefore able to alter VLSMs, which questions the assumption that turbine wakes can be treated as passive scalars. It is, however, important to note that the size of these structures after being affected by the rotor cannot be determined by the statistics based on the streamwise velocity fluctuation in turbine wakes. The study of spatial coherence in turbine wakes revealed that the wake meandering generates an excess streamwise velocity fluctuation which masks those generated by very-large-scale turbulent structures.

The magnitude of the wake meandering is found to be the same for different tip-speed ratios and yaw angles. It supports the hypothesis that the magnitude of the wake meandering mainly depends on incoming boundary-layer characteristics, rather than turbine operating conditions.

(vi) *POD analysis*: The POD study of the wake flow in a horizontal plane shows that some of the POD modes are regular dipole structures which imply periodic motions with specific wavelengths, while others contain more complex and irregular structures. Based on the energy distribution in POD modes, it can be concluded that POD-based reduced-order modeling cannot be used to precisely predict wind turbine wakes in turbulent boundary layer flows. However, the first three POD modes alone are likely enough to predict some general character-

Chapter 4. Wind tunnel study of a wind turbine under different operating conditions

istics of turbine wakes such as the instantaneous wake center trajectory.

A new miniature wind turbine for wind tunnel experiments: design, performance analysis and wake measurements¹

Abstract

Miniature wind turbines, employed in wind tunnel experiments to study the interaction of turbines with turbulent boundary layers, commonly suffer from poor performance with respect to their large-scale counterparts in the field. Moreover, although wakes of wind turbines have been extensively examined in wind tunnel studies, the proper characterization of the performance of wind turbines has received relatively less attention. In this regard, the present study concerns the design and the performance analysis of a new three-bladed horizontal-axis miniature wind turbine with a rotor diameter of 15 cm. Due to its small size, this turbine, called WiRE-01, is particularly suitable for studies of wind farm flows and the interaction of the turbine with an incoming boundary-layer flow. The turbine was designed based on Glauert's optimum rotor, and it was built with three-dimensional (3D) printing technology. Especial emphasis was placed on the accurate measurement of the mechanical power extracted by the miniature turbine from the incoming wind. In order to do so, a new setup was developed to measure the torque of the rotor shaft. Moreover, to provide a better understanding on the connection between the mechanical and electrical aspects of miniature wind turbines, the performance of different direct-current (DC) generators was studied. It is found that electrical outputs of the tested generators can be used to provide a rather acceptable estimation of the mechanical input power. Force and power measurements showed that the thrust and power coefficients of the miniature turbine can reach to 0.8 and 0.4, respectively, which are close to the ones of large-scale turbines in the field. Finally, the interaction of the turbine with a turbulent boundary layer was studied. The comparison of the spectral density of the thrust force and the one of the incoming velocity reveals new insights on the use of turbine characteristics to estimate incoming flow conditions. High-resolution stereoscopic

 $^{^{1}}$ The contents of this chapter are under review in *Experiments in Fluids*.

particle image-velocimetry (S-PIV) measurements were also performed in the wake of the turbine operating at optimal conditions. These measurements can serve as a dataset for the validation of numerical models.

5.1 Introduction

Wind tunnel experiments have become an increasingly valuable tool to elucidate the performance of wind turbines and their wake characteristics (Vermeer et al., 2003). A deep understanding of the wind turbine interaction with the atmospheric boundary layer (ABL) is essential as wind turbines operate in the ABL flow. Due to the unsteady nature of the ABL flow, wind turbines are subject to different incoming flow conditions (e.g., different wind direction and magnitude). Different scenarios of the ABL interaction with wind turbines can be simulated in a wind tunnel under fully controlled conditions. Additionally, as many wind turbines in wind farms have to operate in the wakes of upwind turbines, the study of the cumulative effects of turbine wakes in wind farms is of great importance. This goal can be achieved by performing wind tunnel simulations of the flow field in wind farms consisting of miniature wind turbines. Moreover, the usefulness of techniques to optimize the power production of the whole wind farm (e.g., yaw and pitch angle controls) can be first examined experimentally in wind tunnels.

In the light of the above-mentioned benefits of wind tunnel experiments, they have been widely used in the wind-energy community to study wind turbines and their wakes (e.g., Medici and Alfredsson, 2006; Cal et al., 2010; Chamorro and Porté-Agel, 2009, 2010, 2011; España et al., 2011, 2012; Markfort et al., 2012; Yang et al., 2012; Zhang et al., 2012, 2013; Iungo et al., 2013; Viola et al., 2014; Hancock and Pascheke, 2014; Hancock and Zhang, 2015; Tobin et al., 2015; Bastankhah and Porté-Agel, 2015, 2016; Howland et al., 2016). However, there are still some open issues that need to be addressed in order to improve the suitability of wind tunnel studies of wind turbines. Due to the inevitable difference between the Reynolds number of the wind tunnel flow and the ABL one, miniature wind turbines usually have a poor performance compared to their large-scale counterparts. In general, the performance of a wind turbine is quantified through the definition of the normalized thrust force, called thrust coefficient C_T , and the normalized power, called power coefficient C_P . They are given by

$$C_{T} = \frac{\bar{T}}{0.5\rho(\frac{\pi}{4}d^{2})\bar{u}_{h}^{2}},$$

$$C_{P} = \frac{\bar{P}}{0.5\rho(\frac{\pi}{4}d^{2})\bar{u}_{h}^{3}},$$
(5.1)

where T is the total thrust force exerted on the turbine by the incoming wind, P is the power extracted by the turbine from the incoming wind, ρ is the air density, d is the rotor diameter and \bar{u}_h is the mean streamwise incoming velocity at hub height. The overbar denotes temporal

averaging. The value of C_P reflects the ability of the turbine to extract power, and the overall strength of the turbine wake is determined by the value of C_T (Bastankhah and Porté-Agel, 2014). The values of C_P and C_T in most of the prior wind tunnel studies of miniature turbines under boundary-layer inflow conditions are much lower than those of large-scale turbines. This calls for a better design of miniature turbines in order to attain more realistic values of C_T and C_P .

Another remaining challenge for wind tunnel studies of wind turbines concerns the accurate measurement of the wind turbine performance. As an example, the magnitude of the thrust force for a miniature turbine with d=15 cm and $\bar{u}_h=5$ ms⁻¹ is smaller than 0.3 N, which makes it difficult to measure accurately. In this case, the turbine extracted power is less than 0.5 W.

The extracted power (i.e., mechanical power P_{mech}) for a turbine can be expressed as a product of the shaft torque Q_{sh} and the rotational velocity of the rotor Ω . This mechanical power is then converted to the electrical power in the generator attached to the rotor. The accurate measurement of the shaft torque Q_{sh} for a miniature turbine is a rather challenging task. Some previous studies (e.g., Medici and Alfredsson, 2006) used P_{el} to characterize the wind turbine performance as it can be easily measured. The value of P_{el} is, however, smaller than P_{mech} due to the mechanical and electrical losses in the generator. More importantly, as the electrical power is affected by the characteristics of the generator (Kang and Meneveau, 2010), it will be shown later that the use of electrical power can lead to misleading information about the performance of the wind turbine.

To our knowledge, only a few studies in the literature have tried to directly measure the shaft torque of miniature turbines. Kang and Meneveau (2010) measured the torque by mounting the generator inside a cylindrical housing with internal ball bearings where the rotation of the generator is prevented by the deflection of a strain-gauge sensor. Later, Howard et al. (2015) used a similar concept to measure the mechanical torque. Instead of using a strain-gauge sensor, they measured the torque by adding known weights to the customized moment arm attached to the generator. In spite of the merit of these studies, the calibration procedure of these methods is rather cumbersome and they cannot be easily applied to different operating conditions. Some other studies (e.g., Bastankhah and Porté-Agel, 2015, 2016; Stein and Kaltenbach, 2016; Qing'an et al., 2016), instead, benefited from known equations of direct-current (DC) generators to estimate the mechanical power from the electrical outputs. However, it is unclear whether this method can reliably estimate the turbine mechanical power. Overall, it seems that the power characterization of miniature turbines, as an interdisciplinary problem, suffers from a gap between the fluid mechanical aspect (i.e., the aerodynamic rotor performance) and the electrical one (i.e., DC-generator characteristics).

The purpose of this paper is to design and fully test a new generation of miniature wind turbines, more representative of large-scale turbines in the field. The new miniature turbine is suitable for wind tunnel experiments which aim at studying the ABL interaction with

wind turbines as well as turbine interactions with each other within wind farms. The wind turbine performance is characterized for different operating conditions. In particular, a new setup is developed to directly measure the torque of the rotor shaft under different operating conditions. Moreover, the paper provides a better understanding on the performance of DC generators in order to bridge the knowledge gap between the aerodynamic and electrical aspects of a wind turbine. Finally, high-resolution stereoscopic particle image velocimetry (S-PIV) measurements are used to quantify the wake of the miniature wind turbine under boundary-layer inflow conditions, mainly for numerical validation purposes.

The remainder of this paper is divided into four sections. In Sect. 5.2, the design of the miniature turbine is elaborated. The characterization of the wind turbine performance, including direct torque measurements, is given in Sect. 5.3. The interaction of the turbine with a turbulent boundary layer is measured and discussed in Sect. 5.4. Finally, a summary is presented in Sect. 5.5.

5.2 Wind turbine design

5.2.1 Rotor size

The ABL depth typically varies from a few hundred meters in stable conditions to 3 km in very unstable conditions (Garratt, 1994). The size of commercial wind turbines is in the order of 100 m nowadays (Burton et al., 1995). To properly simulate the ABL-turbine interaction in the wind tunnel, the size of the miniature wind turbines should be therefore small enough compared to the incoming boundary layer. More importantly, in order to study the interaction between wind turbines in wind farms, miniature turbines have to be small enough with respect to the wind tunnel cross-sectional area so that wind tunnel blockage effects are ensured to be minimal. On the other hand, the use of excessively small miniature turbines worsens the scaling issues associated with the difference in Reynolds number between the ABL and wind tunnel flows. After consideration of the above-mentioned limitations as well as the typical size of boundary-layer wind tunnels, the rotor diameter of the miniature turbine d is chosen here to be 15 cm, which is comparable to the size of the miniature turbines used in prior wind tunnel studies (e.g., Chamorro and Porté-Agel, 2009, 2010; Cal et al., 2010; Zhang et al., 2012, 2013).

5.2.2 Airfoil geometry

Due to the small size of the rotor, the rotor blades operate at very low chord Reynolds numbers Re_c given by

$$Re_c = \frac{\rho c u_{rel}}{\mu},\tag{5.2}$$

where ρ and μ are the density and kinematic viscosity of the air, respectively, c is the chord length of the blade cross-sectional area and u_{rel} is the relative flow velocity with respect to the blade. The value of Re_c for a miniature wind turbine with d=15 cm is estimated to be lower than 4×10^4 for incoming velocities u less than $10~{\rm ms}^{-1}$. Prior studies (e.g., Sunada et al., 1997; Laitone, 1997) showed that conventional airfoils for high Reynolds numbers (e.g., NACA airfoils) have a poor performance if they operate in very low Reynolds numbers. In general, an optimum airfoil (i.e., the one with the maximum lift to drag ratio) for very low Reynolds numbers has been found to have:

- a small thickness (Sunada et al., 1997, 2002),
- a 5% circular arc camber (Laitone, 1997; Sunada et al., 1997, 2002; Pelletier and Mueller, 2000),
- a sharp leading edge (Laitone, 1997; Sunada et al., 1997, 2002).

Moreover, as another advantage of thin cambered plates, they are found to be relatively insensitive to the turbulence level (Laitone, 1997; Pelletier and Mueller, 2000) and the surface roughness (Sunada et al., 2002). In order to satisfy the above-mentioned requirements, the airfoil is chosen to be a plate with a 5% circular arc camber, 5% maximum thickness and very sharp edges, as shown in Fig. 5.1 with the blue color. The rotor was built from liquid photopolymer resin by 3D printing technology with a polyjet process and a resolution of 16 μ m. The first tests of the rotor in the wind tunnel revealed that rotor blades could not tolerate the incoming wind with high velocities and were slightly deformed during the measurements. Due to construction limitations, we therefore had to modify the airfoil geometry to a cambered plate with a constant thickness of 5% and chamfered edges as shown in red color in Fig. 5.1.

Based on the data reported in the above-mentioned studies on cambered airfoils in very low Reynolds numbers, the data given in Table 5.1 seem to be reasonable estimations for airfoil design conditions. Note that a rather conservative design angle of attack was chosen to avoid stall conditions, as similarly done in prior studies (e.g., Sherry et al., 2013a).

5.2.3 Design tip-speed ratio

The tip-speed ratio λ is defined as $R\Omega/\bar{u}_h$, where R is the rotor radius and Ω is the rotor rotational velocity. Even though the airfoil performance is better at higher tip-speed ratios due to the higher chord Reynolds number, power losses because of the drag force are higher in this case (Wilson et al., 1976). This can be readily explained by the schematic of the blade element shown in Fig. 5.2(a). As can be seen in the figure, the angle of the relative wind φ becomes smaller if the turbine is designed to rotate faster (i.e., higher design tip-speed ratios). This increases the projection of the drag force in the tangential direction (i.e., $F_D \cos \varphi$), and decreases the one of the lift force (i.e., $F_L \sin \varphi$). As a result, drag losses increase for high design tip-speed ratios. Figure 5.2(b) shows the maximum achievable power at different λ_{design}

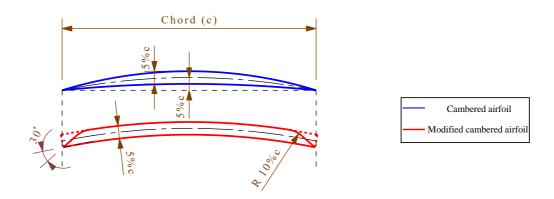


Figure 5.1 – Airfoil geometry: the cambered plate with very thin edges (*blue color*), and the cambered plate with constant thickness modified due to construction limits (*red color*).

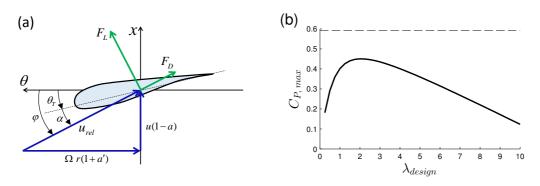


Figure 5.2 – (a) The velocity triangle for a rotor blade element. (b) The most achievable power coefficient $C_{P,max}$ as a function of the design tip-speed ratio for $C_L/C_D = 13$. Dashed line represents the Betz limit.

for the turbine with the selected airfoil (C_L/C_D =13). The figure shows that the maximum power production occurs at $\lambda_{design} \approx 2$ which is much lower than typical values of λ_{design} for large-scale turbines in the field. In order to have a design tip-speed ratio closer to the one of large-scale turbines, while maintaining a high value of C_P , we select the value of λ_{design} to be 4.5 for the miniature turbine.

Maximum Value of C_L/C_D	13
Angle of attack α where C_L/C_D is maximum	4°
Value of C_L where C_L/C_D is maximum	0.75

Table 5.1 – Airfoil design conditions

5.2.4 Optimum chord and twist distributions

The optimum distributions of chord and twist were obtained based on Glauert's optimum rotor (Glauert, 1935). See Sørensen (2015) for a detailed discussion on the optimum rotor design. Figure 5.3 shows the chord and twist distributions of the rotor blade. In order to limit the size of the rotor hub and satisfy other manufacturing constraints, we had to modify the distribution of the chord especially close to the root as shown in the figure. We believe that this modification does not significantly affect the turbine performance as the modification affects mostly the region close to the root, which has only a small contribution to the total torque generation. The three dimensional model of the whole rotor can be found in the electronic supplementary material so that the rotor can be readily employed by other researchers. To facilitate referring to this turbine rotor in future studies, we call it WiRE-01 rotor.

5.3 Wind turbine performance

5.3.1 Thrust force

The turbine is first placed in the WIRE wind tunnel under uniform inflow conditions. The test section of the wind tunnel is 28 m long, 2.6 m wide and 2 m high. The ratio of the miniature turbine frontal area to the wind tunnel cross-sectional one is less than 0.004, so blockage effects are negligible. More information about the wind tunnel can be found in the previous works of the authors (e.g., Bastankhah and Porté-Agel, 2015, 2016). A highly sensitive multi-axis force sensor with the resolution of 1.5×10^{-3} N is connected to the bottom of the turbine tower in order to measure the thrust force exerted on the turbine by the incoming

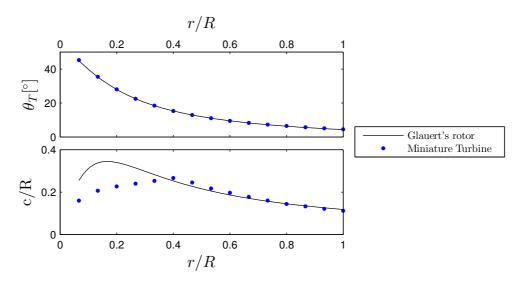


Figure 5.3 – Twist and chord distributions for the blade of the miniature turbine shown by *blue circles*. The ones suggested by the Glauert design method are shown with black lines.

wind. The free-stream velocity is measured with a Pitot-Static tube. Both thrust and velocity measurements were performed for a period of 60 s with the sampling frequency of 1000 Hz. Figure 5.4 shows the variation of the thrust coefficient C_T as a function of the tip-speed ratio λ for different incoming free-stream velocities. In general, the figure shows that the value of C_T for the miniature turbine reaches the value of 0.8, which is similar to the one of large-scale turbines in the field (e.g., $C_T = 0.8$ for Vestas V80-2MW wind turbine, Hansen et al., 2012). As mentioned earlier, having realistic values of C_T is very important as the overall strength of the wake largely depends on the value of C_T .

Figure 5.4 also shows that the value of C_T slightly decreases for high tip-speed ratios, which has been also observed in prior wind tunnel studies (e.g., Yang et al., 2012). This behaviour is, however, in contrast with the common assumption that C_T monotonically increases with the increase of the tip-speed ratio, usually observed for large-scale turbines (Burton et al., 1995). In the following, we try to explain this discrepancy by studying the dependence of C_T on λ for a single annulus.

Let us consider an annulus containing B blade elements, where B is the number of blades (B=3 here). The airfoil geometry of the blade element is assumed to be NACA0012 operating at $Re_c = 1.76 \times 10^6$, which is in the range of Re_c for large-scale turbines. Figure 5.5 shows the values of C_T as a function of the normal induction factor a for the annulus. In Fig. 5.5(a), the design tip-speed ratio is 4 while it is 6 in Fig. 5.5(b). Based on the tabulated airfoil data (Sheldahl and Klimas, 1981), the value of α_{design} and $C_{L,design}$ are selected as 6° and 0.63, respectively, for both design tip-speed ratios. Colored lines show the value of C_T for an annulus from the blade-element approach, whereas the black lines show the value of C_T based on the momentum theory. Note that for a > 0.4, the Glauert empirical relation is plotted as the momentum theory is invalid in this region (Spera, 1994; Manwell et al., 2010). The intersection of each colored line with the solid black line represents the operating condition of the blade element for the given tip-speed ratio (Wilson and Lissaman, 1974), shown by hollow circles in

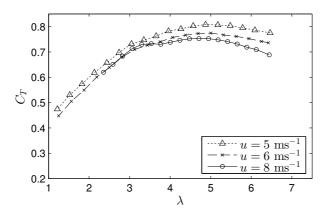


Figure 5.4 – Variation of the thrust coefficient C_T of the miniature turbine with the tip-speed ratio λ at different free-stream incoming velocities.

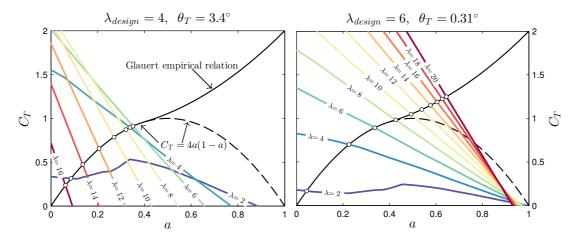


Figure 5.5 – Variation of the thrust coefficient C_T with the normal induction factor a for an annulus at two different design tip-speed ratios ($\lambda_{design} = 4$ and 6). The airfoil profile is NACA0012, operating at $Re_c = 1.76 \times 10^6$. The black lines represent the relationship based on the momentum approach, while the colored lines show it from the blade-element approach. For each tip-speed ratio, the operating condition is indicated by hollow white circles.

Fig. 5.5. As seen in the figure for $\lambda_{design} = 6$, both values of C_T and a increase monotonically with an increase of λ . Consequently, the blade element operates in turbulent wake state (i.e., a > 0.4) at high tip-speed ratios. In contrast, for $\lambda_{design} = 4$, both values of C_T and a increase initially and then decrease with an increase of λ . In this case, the blade element ultimately operates in the propeller state (i.e., a < 0) at very high tip-speed ratios. This explains why the variation of C_T at high tip-speed ratios is different for the miniature turbine (Fig. 5.4) compared with large-scale turbines. Based on the above discussion, it is simply due to the selection of a lower design tip-speed ratio for the miniature turbine, and it is not caused by the difference in chord Reynolds number between the miniature turbine and its large-scale counterparts. Now, the question is why the variation of C_T versus λ is so sensitive to λ_{design} . We try to answer this question by simplifying the governing equations for the considered annulus operating at high tip-speed ratios.

The value of C_T for the annulus at the radial position r is given by (Sørensen, 2015)

$$C_T = \frac{\sigma'(1-a)^2}{\sin^2 \varphi} \left(C_L \cos \varphi + C_D \sin \varphi \right),\tag{5.3}$$

where $\sigma' = Bc/2\pi r$. For high tip-speed ratios, the value of φ is small, so one can assume that $\sin \varphi \approx \varphi$ and $\cos \varphi \approx 1$. Equation 5.3 can be therefore reduced to

$$C_T \approx \frac{\sigma'(1-a)^2 C_L}{\varphi^2} \left(1 + \varphi \frac{C_D}{C_L} \right). \tag{5.4}$$

The term $\varphi C_D/C_L$ in the above equation can be neglected with respect to unity as both φ and C_D/C_L are small. Moreover, the angular induction factor a' is small at high tip-speed ratios, so

from Fig. 5.2(a), $\varphi \approx (1-a)/\lambda$. Equation 5.4 can be thus simplified to

$$C_T \approx \sigma' \lambda^2 C_L.$$
 (5.5)

For an ideal airfoil and small angles of attack, $C_L \approx 2\pi\alpha$ (Abbott and Von Doenhoff, 1959), where $\alpha = \varphi - \theta_T$. Equation 5.5 can be therefore rewritten as

$$\frac{C_T}{2\pi\sigma'} \approx -\lambda a + (\lambda - \lambda^2 \theta_T). \tag{5.6}$$

The above equation states that the value of C_T has a linear relationship with a for high tipspeed ratios. The slope of this linear relationship is negative and its magnitude increases with an increase of λ . This is in agreement with the BEM predictions at high tip-speed ratios for both design tip-speed ratios shown in Fig. 5.5. Furthermore, based on Eq. 5.6, the x-intercept (i.e., $1 - \lambda \theta_T$) of this linear relationship is a function of twist angle θ_T . For a low design tipspeed ratio, the twist angles θ_T is large, so the x-intercept rapidly decreases with an increase of λ . For a high design tip-speed ratio, in contrast, the twist angle θ_T has a small value, so the x-intercept does not largely decrease with an increase of λ . This is confirmed by Fig. 5.5, showing that the x-intercept of the C_T curves (colored lines) sharply decreases with increasing λ for $\lambda_{design} = 4$ ($\theta_T = 3.4^\circ$), while it experiences little change for $\lambda_{design} = 6$ ($\theta_T = 0.31^\circ$). The sharp decrease of the x-intercept of the colored lines in Fig. 5.5 for $\lambda_{design} = 4$ leads to the reduction of the operating C_T (intersecting point with the solid black line shown by hollow circles) for high tip-speed ratios. One can therefore conclude that the different variations of C_T versus λ observed for different design tip-speed ratios are due to the difference in the value of the twist angle.

It is important to note that, even if a high value is chosen for the design tip speed ratio of the rotor, the local design tip-speed ratio for blade elements close to the root of the rotor is much lower. As a result, the central part of the rotor inevitably operates as a propeller (i.e., a < 0) at high-tip speed ratios as experimentally observed by prior studies (e.g., Krogstad and Adaramola, 2012; Bastankhah and Porté-Agel, 2015).

5.3.2 Power extraction

Wind turbine: energy conversion

As mentioned in Sect. 5.1, one of the crucial tasks in wind tunnel studies of wind turbines is to accurately determine the extracted power by the wind turbine (i.e., mechanical power P_{mech}). The mechanical power is converted to electrical power in the generator as shown in Fig. 5.6. All the mechanical input power P_{mech} is, however, not available for the conversion to electrical power, mainly due to friction losses. The converted power is denoted by P_{conv} in Fig. 5.6 and it is equal to $P_{mech} - P_f$, where P_f denotes power losses mainly due to the friction of the bearings and the friction between the moving parts of the machine and the air (Chapman, 2005). Moreover, as shown in the figure, P_{conv} is not entirely available at the

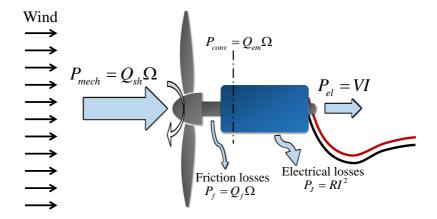


Figure 5.6 – Energy conversion in a miniature wind turbine.

machine's electrical terminals. Some part of this converted power has to overcome electrical losses in the generator. Electrical losses are equal to RI^2 , where R is the armature resistance plus the resistance of the brush contacts on the commutator (Chapman, 2005). Note that R is obviously different from the external resistance used to electrically load the generator.

In general, the converted power P_{conv} can be expressed in terms of $Q_{em}\Omega$, where Q_{em} is called electromagnetic torque (Sen, 2007a) (also called armature torque Q_a , Theraja and Theraja, 2006). Thus,

$$Q_{sh} = Q_{em} + Q_f, (5.7)$$

where Q_f is the friction torque (i.e., P_f/Ω).

The generator used for small model wind turbines is usually a permanent-magnet DC (PMDC) machine. Figure 5.7 shows the equivalent electrical circuit of a PMDC machine in the *generator* mode. If a PMDC generator operates in steady-state conditions, the inductance *L* term in Fig. 5.7 can be neglected (Sharma, 2007; Hughes, 2013). Hence,

$$V_{ind} = V + RI, (5.8)$$

where V_{ind} is the induced voltage (i.e., induced electromotive force, EMF) due to the motion of the armature in the generator. Note that, from Eq. 5.8, V_{ind} is always bigger than the terminal voltage V for a generator. Moreover, for PMDC machines in general, one can show that (Hughes, 2013)

$$V_{ind} = K\Omega, (5.9)$$

$$Q_{em} = KI, (5.10)$$

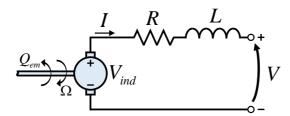


Figure 5.7 – Equivalent electrical circuit of a permanent magnet DC generator.

where *K* is called the EMF constant in Eq. 5.9 and the torque constant in Eq. 5.10. This constant is the same in the both equations if they are expressed in SI units. The value of *K* basically depends only on intrinsic characteristics of the PMDC machine (e.g., machine size, number of poles and magnetic field magnitude) and does not change with operating conditions (Chapman, 2005).

Equation 5.10 can be used to find the electromagnetic torque Q_{em} . In order to estimate the value of the shaft torque Q_{sh} , one has to therefore model the friction torque Q_f . In general, the friction torque Q_f varies with the rotational velocity Ω . Different friction models (e.g., Stribeck friction) have been suggested in the literature (Canudas et al., 1987; Armstrong, 1988; Olsson et al., 1998; Tjahjowidodo et al., 2007). A linear relationship between Q_f and the rotational velocity Ω similar to the one used by Canudas et al. (1987) is considered in this paper due to its simplicity. Hence,

$$Q_f \approx \alpha \Omega + \beta,$$
 (5.11)

where α and β are constants whose values can be estimated based on the DC-machine data provided by the manufacturer. Direct torque measurements will be employed in the following to see whether this method can acceptably predict the shaft torque Q_{sh} .

Direct measurement of shaft torque Q_{sh}

A high-precision rotary torque sensor with an operating range of ± 10 mNm and an accuracy equal to 0.1% of full scale is used in the current study. In order to measure the shaft torque of the generator, the shaft of the rotary torque sensor is directly connected to the shaft of the generator. It is not practically possible to mount the torque sensor between the rotor and the DC generator in the wind tunnel. A separate setup is therefore built as shown in Fig. 5.8. In this setup, a load machine which is basically a more powerful electrical motor simulates the incoming wind effect by rotating the shaft of the torque sensor and the DC machine. Both the load machine and the DC machine are connected to servo controllers so that their operating conditions are separately controlled and monitored. The rotational velocity of both of them are also measured by attached rotary encoders. Note that the use of a separate setup for torque measurements enables us to systematically study the effect of each variable (e.g., rotational

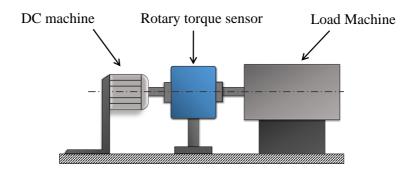


Figure 5.8 – Schematic of the setup for direct measurements of the shaft torque Q_{sh} of DC generators.

velocity Ω) on the performance of the DC generator, keeping other variables (e.g., electrical current I) unchanged. This cannot be easily done if the torque sensor is directly connected to the miniature turbine in the wind tunnel.

In general, the operating condition of a miniature turbine can be uniquely described by the value of its rotational velocity and the generated electrical current. In this torque-sensor setup, the rotational velocity of the load machine and the generated electrical current of the DC machine are separately controlled. Therefore, any operating condition of the miniature turbine can be simulated by the torque-sensor setup. Note that the setup can be also used to measure the shaft torque of the DC machine in *motor* mode. To do so, we only need to reverse the direction of the energy conversion in the setup; i.e., the DC machine acts as a motor to rotate the load machine which acts as a generator in this case.

For the sake of completeness, we study the performance of three brushed DC machines with different sizes and power, all manufactured by Maxon company. All of them are suitable for being used in small-sized wind-turbine models. Table 5.2 shows their characteristics as

		DC-machine I	DC-machine II	DC-machine III
		DCX10L	DCX14L	DCX16L
Outer diameter (mm)		10	14	16
Nominal voltage (V)	V_N	4.5	12	9
Nominal speed (rpm)	Ω_N	7110	7330	11100
Nominal torque (mNm)	Q_N	2.2	6.86	11.9
Nominal current (A)	I_N	0.648	0.646	1.88
No load speed (rpm)	Ω_n	12000	10300	13100
No load current (mA)	I_n	25.2	23.2	54.8
Torque constant (mNm/A)	K	3.52	10.9	6.52

Table 5.2 – Manufacturer-provided data of the DC machines studied in this paper.

provided by the manufacturer. A more powerful electrical machine with a nominal torque of 32 mNm is also used as the load machine.

Figure 5.9 shows the difference between the measured shaft torque Q_{sh} and KI as a function of the rotational velocity Ω for different electrical currents and DC machines in both *generator* and *motor* modes. If Eqs. 5.7 and 5.10 stated in Sect. 5.3.2 are valid for DC machines in real situations, $Q_{sh} - KI$ should not depend on the electrical current I because, as mentioned earlier, it should be equal to the friction torque Q_f that varies only with the rotational velocity Ω . The figure shows that, although the relationship between $Q_{sh} - KI$ and Ω slightly changes with the electrical current in some cases (especially for DC-machine II), the overall agreement is acceptable and one can assume that $Q_{sh} \approx KI + Q_f(\Omega)$.

The conclusion drawn above is in contrast with what was suggested by Kang and Meneveau (2010) in their pioneering study. They compared the manufacturer-provided data with measured quantities and reported a significant deviation. Specifically, they compared the value of KI with the measured P_{el}/Ω , and showed that there is a big difference between them. In addition, they showed that V is not linearly proportional to Ω . Firstly, note that KI should be compared with P_{conv}/Ω , which is clearly bigger than P_{el}/Ω due to the electrical losses. Secondly, as stated in Eq. 5.9, V_{ind} is supposed to be linearly proportional to Ω , not V. In fact, even from their own data, the shaft torque is found to be linearly proportional to the electrical current, and the value of the slope for this linear relationship is very similar to the manufacturer-provided value of the torque constant K (equation 4 in the original study). This in turn confirms the fact that $Q_{sh} \approx KI + Q_f$.

Figure 5.9 also shows that the value of Q_{sh} is bigger than Q_{em} in the *generator* mode while it is smaller than Q_{em} in the *motor* mode. This is expected as the energy is converted from the electrical form to the mechanical one in motors, contrary to generators. Furthermore, it can be seen that the friction torque Q_f increases with the increase of rotational speed Ω , as expected. The figure also shows that a linear relationship similar to Eq. 5.11 can acceptably approximate the variation of Q_f with Ω , even though a polynomial fit matches better. One possible explanation for this non-linear behavior is that core losses are neglected in this study compared to friction losses. See Chapman (2005) for more information.

The data shown in Fig. 5.9 can be used to find the values of α and β in Eq. 5.11. We, however, wonder how well theses values can be estimated based on the data of the DC machines provided by the manufacturer. This could be of great interest particularly for those who cannot perform direct torque measurements and therefore can only use the manufacturer-provided data. To do so, one can use the DC-machine data at nominal and no-load operating conditions presented in Table 5.2. Note that manufacturer-provided data are usually for DC machines in *motor* mode. By using these data, hence, we implicitly assume that the magnitude of the friction torque is similar for both modes, which is supported by the data of Fig. 5.9. At nominal conditions, friction torque is equal to $KI_N - Q_N$ for a DC motor, where I_N and Q_N are the electrical current and the shaft torque at nominal conditions, respectively. At no-

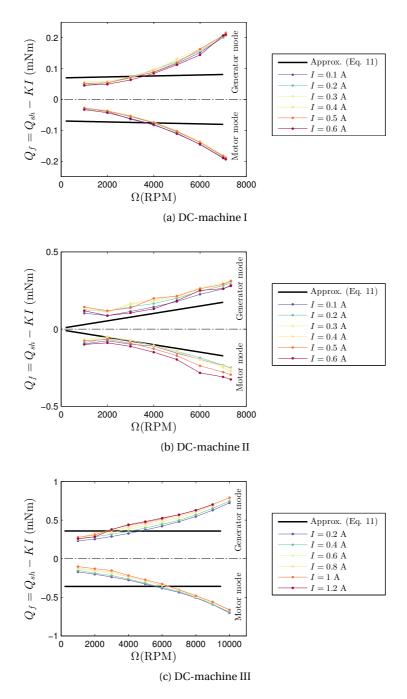


Figure 5.9 – Measured values of $(Q_{sh}-KI)$ versus the rotational velocity Ω for different electrical currents and DC machines in both *motor* and *generation* modes. The black lines show the prediction of the friction torque Q_f based on Eq. 5.11 and using the manufacturer-provided data.

load conditions, Q_{sh} is equal to zero for a DC motor and thereby $Q_f = KI_n$, where I_n is the electrical current at no-load conditions. The predictions of the Q_f based on the data of Table 5.2 are shown by black solid lines in Fig. 5.9. Clearly, they are not in good agreement with the measured data, especially for DC machines I and III. However, they might be still useful for making a rough estimation about the magnitude of the friction torque. This will be further discussed in the following.

Power coefficient C_P of the miniature turbine

Figure 5.10 shows the variation of the power coefficient C_P of the miniature turbine as a function of the tip-speed ratio λ at the free-stream velocity of 8 ms⁻¹. To see the effect of the DC generator on the wind-turbine performance, the data are shown for the rotor connected to both DC generators II and III under the same incoming flow conditions. For each DC generator, the value of the power P is calculated based on: (i) the measured shaft torque Q_{sh} multiplied by Ω , (ii) the electromagnetic torque Q_{em} multiplied by Ω , (iii) the electromagnetic torque Q_{em} plus the friction torque Q_f multiplied by Ω , where Q_f is estimated based on the data provided by the manufacturer as discussed in Sect. 5.3.2, and finally (iv) the terminal voltage V times the electrical current I. As shown in the figure, the value of C_P based on the measured mechanical input power ($P_{mech} = Q_{sh}\Omega$) is very similar for both cases. This is expected as the mechanical power does not depend on generator characteristics. The figure also shows that the values of C_P based on the converted power (i.e., $P_{conv} = Q_{em}\Omega$) are smaller than the ones based on the mechanical power, and they are different for the two DC machines. This can be explained by the fact that $P_{conv} = P_{mech} - P_f$ and the value of friction losses (i.e., P_f) depend on generator characteristics. It is also interesting to note that the difference between P_{conv} and P_{mech} is smaller for lower tip-speed ratios. At lower tip-speed ratios, the turbine rotates slower so the friction torque is smaller. Moreover, the value of the electromagnetic torque is generally quite high for low tip-speed ratios, so the friction torque becomes less important.

By modeling the friction torque (Eq. 5.11) and adding it to the converted power, the figure shows that one can have a rather acceptable estimation of the mechanical input power. This approximation method is more promising if the shaft torque is not much smaller than the nominal value because, in this case, the friction torque is likely to be negligible compared to the electromagnetic torque. The DC machine should not, however, work beyond the nominal operating range as the linear proportionality between the electromagnetic torque and the electrical current does not necessarily hold anymore, and working in these conditions can also permanently damage the machine (Krishnan, 2009). It is also important to remind that DC-machine characteristics change with temperature, so the manufacturer-provided data are not likely to be reliable at high temperatures (Krishnan, 2009).

Figure 5.10 also shows the value of C_P based on the generated electrical power P_{el} for both DC generators. As seen in the figure and also shown by Kang and Meneveau (2010), the generated power is much smaller than the extracted one due to mechanical and electrical losses. More importantly, the figure shows that the use of electrical power can lead to misleading

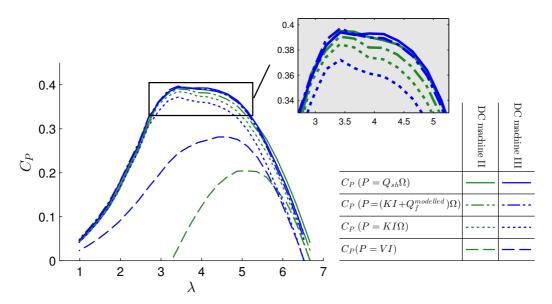


Figure 5.10 – Variation of the power coefficient C_P with the tip-speed ratio λ for the miniature turbine with two different DC machines under the same inflow conditions. For each DC machine, the turbine power is calculated with different methods. The free-stream incoming velocity is equal to 8 ms⁻¹.

information on wind turbine characteristics. For instance, it significantly overestimates the value of the optimal tip-speed ratio λ_{opt} , at which the extracted power P_{mech} is maximum. The reason is that electrical losses in the generator (i.e., RI^2) rapidly increase with the increase of the electrical current I. The value of P_{el} therefore becomes very small for lower tip-speed ratios (i.e., higher electrical currents). This is why the maximum generated power in Fig. 5.10 occurs at tip-speed ratios higher than the optimal one.

The variation of the power coefficient C_P (based on measured P_{mech}) with the tip-speed ratio λ is shown in Fig. 5.11 for different incoming free-stream velocities. As seen in the figure, the value of C_P increases with the increase of the incoming flow velocity, which is due to the better performance of the rotor blades at higher Reynolds numbers. The value of C_P for the miniature turbine can be as high as 0.4 as shown in the figure, which is quite remarkable for a miniature wind turbine with d=15 cm. The optimal tip-speed ratio λ_{opt} varies slightly with the change of the incoming velocity but overall the best performance occurs at $\lambda_{opt} \approx 4$ which is smaller than the design tip-speed ratio ($\lambda_{design}=4.5$). The difference is due to the use of likely inaccurate airfoil design information presented in Table 5.1.

5.4 Turbine interaction with a turbulent boundary layer

The interaction of the miniature turbine with a boundary layer is elaborated herein. The turbine hub height z_h is selected to be 12.5 cm in order to have a ratio of z_h/d similar to the

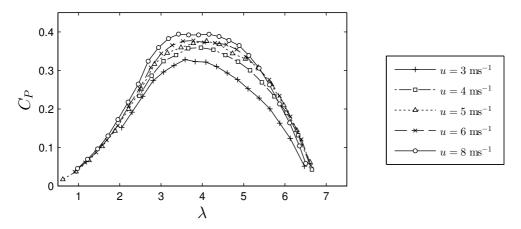


Figure 5.11 – Variation of the thrust coefficient C_P of the miniature turbine with the tip-speed ratio λ at different free-stream incoming velocities.

one of large-scale turbines in the field. A schematic figure of the miniature wind turbine is shown in Fig. 5.12(a). The turbine is placed in a smooth boundary layer developed in the WIRE boundary-layer wind tunnel. Due to the long test section of the wind tunnel, the boundary layer is naturally developed over the floor without the need of any tripping mechanism. The mean incoming velocity at hub height is kept constant at 5 ms⁻¹ during the measurements. Figure 5.12(b) shows the variations of the thrust coefficient C_T and the power coefficient C_P versus the tip-speed ratio for the miniature turbine in the boundary layer. As shown, the turbine performance in this case is similar to the one under uniform inflow conditions with the same velocity magnitude (Fig. 5.11).

Recent works (e.g., Bottasso et al., 2015; Cacciola et al., 2016) have shown the potential of using the information related to the wind-turbine performance to provide insights on the incomingflow characteristics. In order to extend this stream of research, we compare the spectral density of the thrust force for two different tip-speed ratios with the one of the incoming flow at hub height, obtained with hot wire measurements, as seen in Fig. 5.13. For each operating condition, both velocity and thrust measurements were performed over a period of 60 s with a sampling frequency of 15000 Hz. As shown in the figure, some strong peaks exist in the spectral density of the thrust force, unlike the one of the incoming flow. The peaks occur in the rotational frequency of the rotor f_T and its harmonics (shown by dashed black lines in Figs. 5.13(a) and (b)) which is in agreement with what was reported by Yang et al. (2012). For the higher tip-speed ratio, it is interesting to note that there are also some peaks in half of the rotational frequency $f_T/2$ and its harmonics (shown by dotted black lines in Fig. 5.13(b)). In general, these peaks are not limited to the wind turbine as they are observed usually for any rotating machine. Different machinery defects can be responsible for the observed peaks in the spectral density of the thrust force. The ones associated with f_T and its harmonics can be caused by vibrations due to the rotor mass imbalance, bent shaft and angular and parallel misalignments (Scheffer and Girdhar, 2004). The ones with $3f_T$ and its harmonics can be

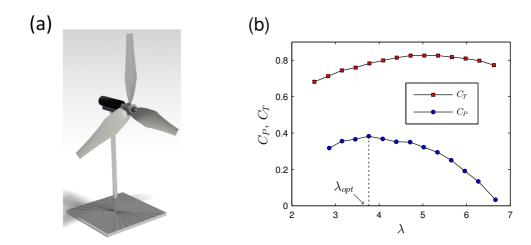


Figure 5.12 – (a) Schematic figure of the miniature wind turbine placed in the turbulent boundary layer. (b) Variation of C_T and C_P with the tip-speed ratio λ for the miniature turbine placed in the boundary layer with $\bar{u}_h = 5 \text{ ms}^{-1}$.

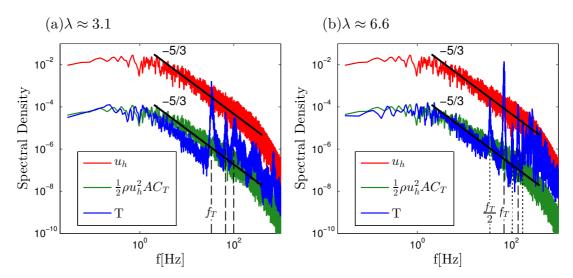


Figure 5.13 – Spectral density of the incoming velocity at hub height u_h , the thrust force T and $(1/2)\rho u_h^2 AC_T$ for two different tip-speed ratios. The rotational frequency of the rotor f_T and its harmonics are shown by dashed lines. One half of the rotor rotational frequency $0.5 f_T$ and its harmonics are shown by dotted lines.

also related to the blade pass frequency (BPF) (De Silva, 2007). Finally, the peaks at $f_T/2$ and its harmonics that are seen for the higher tip-speed ratio are mainly due to the mechanical looseness, either between the rotor and the shaft or between the baseplate and the ground. See Scheffer and Girdhar (2004) for more information on the vibration analysis of rotating machines.

For frequencies lower than f_T , the figure shows that the thrust spectral density closely matches the one of $(1/2)\rho u^2 AC_T$, where A is the rotor area. As low-frequency scales contain most of

the turbulent kinetic energy of a turbulent flow, this matching can be employed as a useful technique to estimate incoming flow characteristics for wind turbines operating in the field. For those turbines, time-resolved measurements of the turbine thrust force are likely to be more feasible and affordable than those of the incoming flow, so the spectral density of the thrust force can be used to predict the one of the incoming velocity at low frequencies. This means that a strain-gauge sensor installed on the turbine tower can potentially reveal valuable quantitative information on the incoming flow, e.g., turbulence intensity and the integral length scale.

Finally, in order to provide a complete dataset for the validation of numerical models, the flow field in the wake of the miniature turbine is also quantified in this paper. To achieve this goal, a high-resolution stereoscopic particle image velocimetry (S-PIV) system from LaVision was employed to measure the three velocity components in planes normal to the incoming flow (i.e., yz planes, where y and z denote the lateral and vertical directions, respectively). A 400 mJ dual-head Nd:Yag laser together with two 16-bit sCMOS cameras (2560×2160) was used to capture the wake flow in field of views (FOVs) with the size of $3d \times 2d$ and the spatial resolution of 0.023d. The mean velocity field was obtained by ensemble averaging 1200 instantaneous velocity fields, and the data were sampled with a frequency of 10 Hz. Velocity measurements were performed at the optimal tip-speed ratio λ_{opt} . Note that we do not intend to extensively discuss the turbine-wake characteristics here. Detailed discussions on turbine wakes can be found in the literature (see for instance Wu and Porté-Agel, 2011). In the following, the wake of the new miniature turbine is qualitatively discussed and compared with the wakes measured in previous wind-tunnel studies.

Figure 5.14 shows contours of the normalized velocity deficit $\Delta \bar{u}/\bar{u}_h$ overlaid with vectors of in-plane velocity components in yz planes at different downwind locations. As seen in the figure, the wake of the new miniature turbine is qualitatively similar to those reported in previous wind tunnel studies. However, as mentioned earlier, this turbine has more realistic values of C_T and C_P . As a consequence, the wake is much stronger for this turbine in terms of both velocity deficit (due to high C_T) and rotation (due to high C_P) than the ones in previous wind tunnel studies (e.g., Chamorro and Porté-Agel, 2009; Zhang et al., 2012; Yang et al., 2012).

As expected, Fig. 5.14 shows that values of the velocity deficit and the wake rotation decrease as the wake moves downstream, although the wake is not yet recovered after 10 rotor diameters. The wake recovery is usually associated with the turbulent momentum flux acting as a mechanism to transfer the energy from the outer flow into the wake. Figures 5.15 and 5.16 show contours of the normalized vertical and lateral momentum fluxes (i.e., $\overline{u'w'}/\bar{u}_h^2$ and $\overline{u'v'}/\bar{u}_h^2$, respectively) at different downwind locations. As shown in the figures, their maximum values occur at around x/d=3-4, and they both have a non-symmetrical structure which is in agreement with previous studies (e.g., Chamorro and Porté-Agel, 2009). This tilting of turbulent flux distributions is likely associated with the rotation of the wake (Wu and Porté-Agel, 2011).

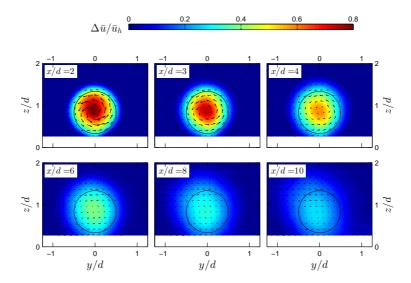


Figure 5.14 – Contours of the normalized velocity deficit $\Delta \bar{u}_h/\bar{u}_h$ in yz planes at different downwind locations for the miniature turbine operating at $\lambda = \lambda_o$. The vector field represents the in-plane velocity components. The black circles show the frontal area of the wind turbine.

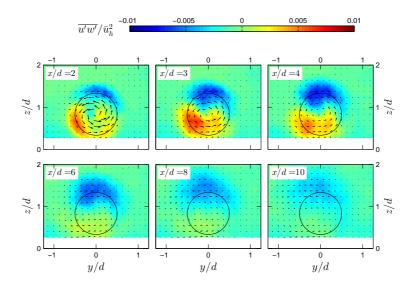


Figure 5.15 – Contours of the normalized vertical momentum turbulent flux $\overline{u'w'}/\bar{u}_h^2$ in yz planes at different downwind locations for the miniature turbine operating at $\lambda=\lambda_o$. The vector field represents the in-plane velocity components. The black circles show the frontal area of the wind turbine.

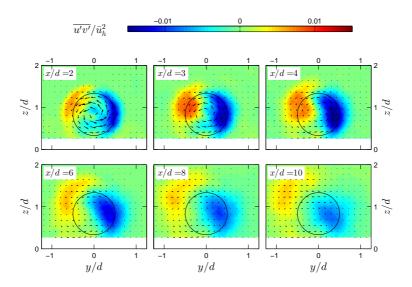


Figure 5.16 – Contours of the normalized lateral momentum turbulent flux $\overline{u'v'}/\bar{u}_h^2$ in yzplanes at different downwind locations for the miniature turbine operating at $\lambda = \lambda_o$. The vector field represents the in-plane velocity components. The black circles show the frontal area of the wind turbine.

The streamwise turbulence intensity $I_u = \sigma_u / \bar{u}_h$ is one of the other important turbulence statistics of turbine wakes. The characterization of the turbulence intensity is of great importance as it induces harmful fatigue loads on blades of downwind turbines (Frandsen, 2007). The turbulence intensity I_u in turbine wakes consists of the turbulence intensity of the inflow $I_{u,in}$ and the one added (or subtracted) due to the presence of the turbine $I_{u,add}$. The value of $I_{u,add}$ is given by (Wu and Porté-Agel, 2012)

$$I_{u,add} = +\sqrt{I_u^2 - I_{u,in}^2} \qquad I_u \ge I_{u,in}$$

$$I_{u,add} = -\sqrt{I_{u,in}^2 - I_u^2} \qquad I_u < I_{u,in}$$
(5.12)

$$I_{u,add} = -\sqrt{I_{u,in}^2 - I_u^2} \qquad I_u < I_{u,in}$$
 (5.13)

Figure 5.17 shows the contours of $I_{u,add}$ in yz planes at different downwind locations. As seen in the figure, the added streamwise turbulence intensity has a horseshoe shape with the maximum level close to the top-tip level. Moreover, the value of $I_{u,add}$ is negative downwind of the turbine bottom tip meaning that the turbine suppresses the turbulence in this region, which is in agreement with prior studies (e.g., Wu and Porté-Agel, 2011).

Some quantitative information on key turbulence statistics of the wake can be found in Appendix 1 for numerical validation purposes.

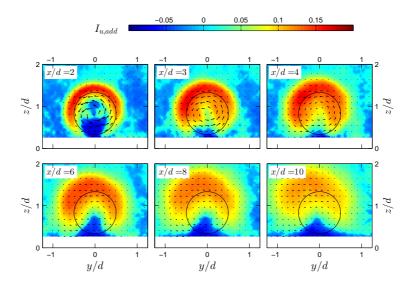


Figure 5.17 – Contours of the added streamwise turbulence intensity $I_{u,add}$ in yz planes at different downwind locations for the miniature turbine operating at $\lambda = \lambda_o$. The vector field represents the in-plane velocity components. The black circles show the frontal area of the wind turbine.

5.5 Summary

A new three-bladed horizontal-axis miniature wind turbine with a diameter of 15 cm, suitable for wind tunnel studies of wind turbine wakes and wind farm flows, is designed and fully characterized in this study. The main motivation for the design of a new miniature turbine is to achive higher and more realistic (similar to those of field-scale turbines) values of C_T and C_P , compared with previously used miniature wind turbines. The turbine, designed based on Glauert's optimum rotor, is built with 3D-printing technology.

Force measurements are performed in the wind tunnel to calculate the thrust coefficient C_T for different incoming velocities. Overall, the magnitude of C_T of the miniature turbine is found to be around 0.8 at the optimal tip-speed ratio, which is similar to the one of large-scale turbines. Moreover, it is found that the value of C_T slightly decreases at high tip-speed ratios for the miniature turbine, contrary to the one of large-scale turbines. A simple theoretical analysis is employed to show that the variation of C_T with tip-speed ratio λ can be different at high tip-speed ratios depending on the value of the blade twist angle.

For the sake of accurate measurement of the turbine extracted power, a new setup is developed to directly measure the torque of the rotor shaft. The measurements show that the value of power coefficient C_P can reach to around 0.4, which is considerable for a miniature turbine with this small size. Particular attention is also focused on the conversion of mechanical energy into electrical one in the generator. To this end, the performance of different DC generators is systematically studied for various operating conditions. It is found that the

use of the manufacturer-provided data for the tested generators can yield a fairly acceptable estimation of the turbine extracted power.

The interaction of the turbine with a turbulent boundary layer is also studied in this paper. An interesting similarity is found between the spectral density of the thrust force T and the one of $(1/2)\rho u_h^2 AC_T$ at low-frequency scales. This means that time-resolved thrust measurements can be used in the field to provide useful information about the incoming flow. Finally, high-resolution S-PIV measurements are carried out to quantify the wake of the miniature turbine and provide a unique dataset for the validation of numerical models. The results show that the more realistic values of C_T and C_P of the new turbine, compared with previously used miniature turbines, leads to turbine wake flows that have stronger velocity deficit and wake rotation strength.

5.6 Appendix 1

This appendix presents lateral and vertical profiles of key turbulent statistics of the wake of the new miniature turbine (WiRE-01): (i) normalized velocity deficit $\Delta \bar{u}/\bar{u}_h$ (Fig. 5.18), (ii) normalized in-plane velocity components $(\bar{w}/\bar{u}_h$ and \bar{v}/\bar{u}_h) (Fig. 5.19), (iii) added streamwise turbulence intensity $I_{u,add}$ (Fig. 5.20) and (iv) normalized turbulent momentum fluxes $(\bar{u}'\bar{w}'/\bar{u}_h^2)$ and $(\bar{u}'\bar{v}'/\bar{u}_h^2)$ (Fig. 5.21).

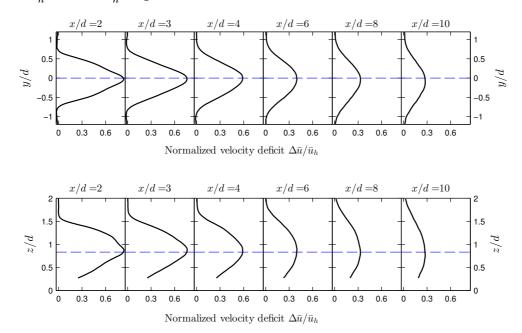


Figure 5.18 – Lateral (*top*) and vertical (*bottom*) profiles of the normalized velocity deficit through the hub level at different downwind locations. Blue dashed lines represent the rotor axis.

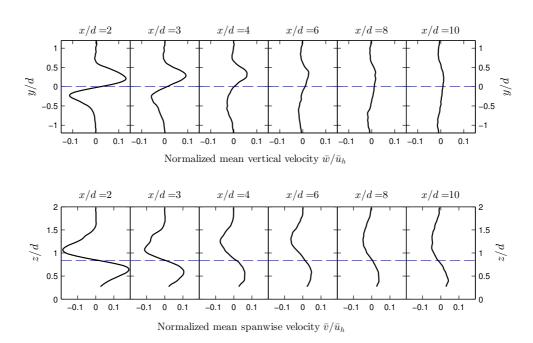


Figure 5.19 – Lateral profiles of the normalized vertical velocity (*top*) and vertical profiles of the normalized spanwise velocity (*bottom*) through the hub level at different downwind locations. Blue dashed lines represent the rotor axis.

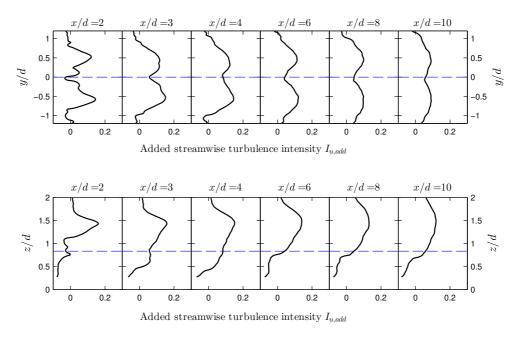


Figure 5.20 – Lateral (*top*) and vertical (*bottom*) profiles of the added streamwise turbulence intensity through the hub level at different downwind locations. Blue dashed lines represent the rotor axis.

Chapter 5. A new miniature wind turbine for wind tunnel experiments

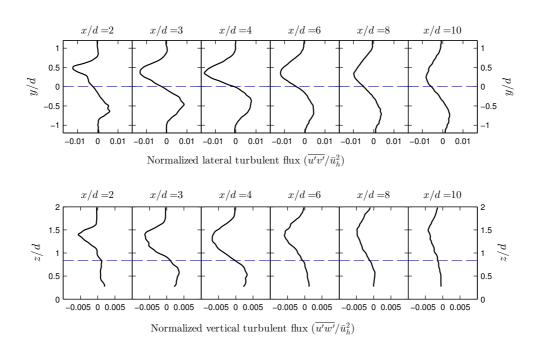


Figure 5.21 – Lateral profiles of the normalized lateral momentum turbulent flux (*top*) and vertical profiles of the normalized vertical momentum turbulent flux (*bottom*) through the hub level at different downwind locations. Blue dashed lines represent the rotor axis.

6 Overall summary and future research perspectives

6.1 Overall summary

This thesis presents theoretical and experimental studies on the interaction of wind turbines with turbulent boundary-layer flows. Key elements and findings of these studies are summarized below.

- **Study 1**: A new simple analytical model was proposed in this study to predict the streamwise velocity distribution in the far wake of a non-yawed turbine. The proposed model is based on the conservation of mass and momentum, and a Gaussian distribution is considered for velocity deficit profiles in the wake. The model predictions are found to be in good agreement with the numerical and experimental data of different cases if a proper wake growth rate is used for each case. Moreover, in terms of the power prediction of downwind turbines, the error of the model predictions is found to be small and rather insensitive to the position of the downwind turbines, compared to that of top-hat models.
- Study 2: Wind tunnel measurements were performed to study the wake of a miniature turbine under yawed conditions. In general, the results show that, with the increase of yaw angle, the wake deflection increases and the wake velocity deficit decreases. The experimental data were also used to perform a budget study of the continuity and Reynolds-averaged Navier-Stokes equations. This theoretical study provides new insights on the wake of yawed turbines. For instance, it mathematically shows that the wake deflection angle has an asymmetric distribution with respect to the wake center, which is consistent with the experimental data. Moreover, the study explains the mechanism for the formation of a counter-rotating vortex pair (CVP) in the wake cross-section under highly-yawed conditions. Potential theory was also used to show that the vertical displacement of the wake center in highly yawed conditions is due to the interaction of the wake rotation, CVP and the ground. Finally, this study helped us develop governing equations upon which a simple analytical wake model is built. This model aims at predicting the streamwise velocity distribution in the wake of a yawed

turbine. The proposed model, validated against the experimental data, can be used to assess the suitability of yaw angle control for optimizing the power production in wind farms.

- Study 3: Detailed wind tunnel measurements were performed to study the interaction of a turbine with an incoming boundary layer at different tip-speed ratios and yaw angles. Power and force measurements were carried out to characterize the wind turbine performance. In addition, hot-wire and S-PIV measurements were performed to study the flow in the upwind, near wake and far-wake regions. These measurements provide new insights into the effect of turbine operating conditions on flow characteristics in these regions. For the upwind region, the results show a strong lateral asymmetry under yawed conditions. For the near-wake region, the evolution of tip and root vortices was studied with the use of both instantaneous and phase-averaged vorticity fields. The results suggest that the vortex breakdown position cannot be determined based on phase-averaged statistics, particularly for tip vortices under turbulent inflow conditions. Moreover, the measurements in the near-wake region indicate a complex velocity distribution with a speed-up region in the wake center, especially for higher tip-speed ratios. In order to elucidate the meandering tendency of far wakes, particular focus was placed on studying the characteristics of very-large-scale motions in the boundary layer and their interaction with wind turbines. Although the very-large-scale motions are elongated in the streamwise direction, their cross sections are found to have a size comparable to the rotor area, so they can be affected by the presence of the turbine. In addition, the study of spatial coherence in turbine wakes reveals that any statistics based on streamwise velocity fluctuations cannot provide reliable information about the size of large turbulent structures in turbine wakes due to the effect of wake meandering. The results also suggest that the magnitude of wake meandering does not depend on turbine-operating conditions. Finally, POD analysis of the turbine wake shows that the first a few POD modes alone are likely enough to predict some general characteristics of turbine wakes such as the instantaneous wake-center trajectory.
- Study 4: A new miniature wind turbine with the rotor diameter of 15 cm was designed and examined in this study. The goal was to achieve performance levels (e.g., thrust and power coefficients) that are as close as possible to those of large-scale wind turbines. The turbine was designed based on Glauert's optimum rotor and it was built with the 3D-printing technology. Particular focus was given to the accurate characterization of the power extracted by the turbine from the incoming wind. To this end, we developed a new setup to measure the shaft torque of the rotor. Moreover, to examine the possibility of estimating the extracted power from electrical outputs, the performance of different DC generators was studied in detail. The results for the tested generators show that electrical outputs together with the data provided by the manufacturer can be used to provide a rather acceptable estimation of the extracted power. In general, it is found that the power and thrust coefficients of the miniature turbine can reach to values of 0.4 and 0.8 in optimal conditions, respectively, which are close to the ones of large-scale

turbines. Moreover, the thrust coefficient is found to decrease slightly at high tip-speed ratios, unlike the one for large-scale turbines. Our results show that this reduction is due to the relatively larger twist angle selected for the blades of the miniature turbine. In addition, the comparison between the spectral density of the thrust force and incoming velocity reveals that the thrust measurements for wind turbines can be used to estimate the incoming flow characteristics. This is of interest in particular for wind turbines operating in the field.

6.2 Future research perspectives

Based on the results obtained in this work, the following areas are proposed for further research:

- Wind tunnel studies of wind farm flows: The interaction of the boundary layer flow with the new miniature wind turbine is in detail studied in this thesis. The next step is to use this turbine to study the interaction of multiple wakes in wind farms with different configurations and layouts. As this turbine has more realistic characteristics compared to those used in prior wind tunnel studies, wind tunnel simulations of wind farms using this turbine can be more representative of the ones in the field. Moreover, the power production in wind farms can be accurately determined by means of the new developed setup. In particular, the possibility of wind farm power optimization by controlling the yaw angle of turbines can be experimentally studied using the designed miniature turbine.
- Effects of thermal stratification on wind turbine wakes: The studies performed in this thesis were limited to neutrally-stratified flow conditions while the ABL flow is commonly thermally stratified. Hence, the study on the effects of thermal stratification on turbine wakes is of particular interest. Some recent wind tunnel studies (e.g., Chamorro and Porté-Agel, 2010; Zhang et al., 2013; Hancock and Pascheke, 2014; Hancock and Zhang, 2015) have investigated effects of thermal stratification on the wake of a standalone turbine. However, these studies were limited to boundary layers with rather small temperature gradients. Moreover, they were unable to simulate the capping inversion layer, which, as shown in previous numerical studies (e.g., Abkar and Porté-Agel, 2013), can considerably affect the vertical entrainment of the energy in large wind farms. In order to address the limitations of the prior research, wind tunnel measurements can be carried out in the new boundary-layer wind tunnel at the WIRE laboratory to study effects of a realistic thermally-stratified ABL flow capped by the inversion layer on turbine wakes.
- Wind turbine operation in complex terrain: In general, the study on the performance of wind turbines and their wakes over complex terrain suffers from the lack of enough attention in spite of its many practical applications for onshore wind turbines. As the

Chapter 6. Overall summary and future research perspectives

studies in this thesis are limited to flat terrain, future wind tunnel experiments can be carried out to study wind turbines and wind farms in interaction with topographies with different shapes and slopes.

• Wake recovery under different operating conditions: The wake recovery rate is a key parameter in the analytical wake models developed in this thesis. Although we generally know that incoming flow conditions affect the wake recovery, the quantitative relationship between them remains unknown. More experimental and theoretical studies are therefore required to systematically investigate the wake recovery under different conditions (e.g., different thermal stabilities and surface cover types). It is also of interest to study the growth of accumulated wakes in large and very large wind farms.

Bibliography

- Abbott, I. H. and Von Doenhoff, A. E. *Theory of wing sections, including a summary of airfoil data.* Courier Corporation, 1959.
- Abkar, M. and Porté-Agel, F. The effect of free-atmosphere stratification on boundary-layer flow and power output from very large wind farms. *Energies*, 6(5):2338–2361, 2013.
- Abkar, M. and Porté-Agel, F. Influence of atmospheric stability on wind-turbine wakes: A large-eddy simulation study. *Physics of Fluids (1994-present)*, 27(3):035104, 2015.
- Abraham, G. The flow of round buoyant jets issuing vertically into ambient fluid flowing in a horizontal direction. In *5th International Water Pollution Research Conference*, San-Francisco, July–August 1970.
- Amoura, Z., Roig, V., Risso, F., and Billet, A. Attenuation of the wake of a sphere in an intense incident turbulence with large length scales. *Physics of Fluids (1994-present)*, 22(5):055105, 2010.
- Andersen, S. J., Sørensen, J. N., and Mikkelsen, R. Simulation of the inherent turbulence and wake interaction inside an infinitely long row of wind turbines. *Journal of Turbulence*, 14(4): 1–24, 2013.
- Armstrong, B. Friction: Experimental determination, modeling and compensation. In *Robotics and Automation, 1988. Proceedings., 1988 IEEE International Conference on*, pages 1422–1427. IEEE. 1988.
- *Openwind theoretical basis and validation.* AWS truepower, LCC, version1.3 edition, April 2010.
- Bagchi, P. and Balachandar, S. Response of the wake of an isolated particle to an isotropic turbulent flow. *Journal of Fluid Mechanics*, 518:95–123, 2004.
- Balakumar, B. and Adrian, R. Large-and very-large-scale motions in channel and boundary-layer flows. *Philosophical Transactions of the Royal Society of London A: Mathematical, Physical and Engineering Sciences*, 365(1852):665–681, 2007.
- Barlas, E., Buckingham, S., and van Beeck, J. Roughness effects on wind-turbine wake dynamics in a boundary-layer wind tunnel. *Boundary-Layer Meteorology*, 158(1):27–42, 2016.

- Barthelmie, R., Folkerts, L., Larsen, G., Rados, K., Pryor, S., Frandsen, S., Lange, B., and Schepers, G. Comparison of wake model simulations with offshore wind turbine wake profiles measured by sodar. *Journal of Atmospheric and Oceanic Technology*, 23:881–901, 2005.
- Barthelmie, R., Hansen, K., Frandsen, S., Rathmann, O., Schepers, J., Schlez, W., Phillips, J., Rados, K., Zervos, A., Politis, E., and Chaviaropoulos, P. Modelling and measuring flow and wind turbine wakes in large wind farms offshore. *Wind Energy*, 12(5):431–444, 2009.
- Barthelmie, R. J. and Jensen, L. Evaluation of wind farm efficiency and wind turbine wakes at the nysted offshore wind farm. *Wind Energy*, 13(6):573–586, 2010.
- Barthelmie, R. J., Frandsen, S. T., Nielsen, M., Pryor, S., Rethore, P.-E., and Jørgensen, H. E. Modelling and measurements of power losses and turbulence intensity in wind turbine wakes at middelgrunden offshore wind farm. *Wind Energy*, 10(6):517–528, 2007.
- Bastankhah, M. and Porté-Agel, F. A new analytical model for wind-turbine wakes. *Renewable Energy*, 70:116–123, 2014.
- Bastankhah, M. and Porté-Agel, F. A wind-tunnel investigation of wind-turbine wakes in yawed conditions. In *Journal of Physics: Conference Series*, volume 625, page 012014. IOP Publishing, 2015.
- Bastankhah, M. and Porté-Agel, F. Experimental and theoretical study of wind turbine wakes in yawed conditions. *Journal of Fluid Mechanics*, 806:506–541, 2016.
- Bastine, D., Witha, B., Wächter, M., and Peinke, J. Towards a simplified dynamic wake model using POD analysis. *Energies*, 8(2):895–920, 2015.
- Beresh, S. J., Henfling, J. F., and Spillers, R. W. Meander of a fin trailing vortex and the origin of its turbulence. *Experiments in fluids*, 49(3):599–611, 2010.
- Berkooz, G., Holmes, P., and Lumley, J. L. The proper orthogonal decomposition in the analysis of turbulent flows. *Annual review of fluid mechanics*, 25(1):539–575, 1993.
- Bottasso, C., Cacciola, S., and Schreiber, J. A wake detector for wind farm control. In *Journal of Physics: Conference Series*, volume 625, page 012007. IOP Publishing, 2015.
- Broadwell, J. E. and Breidenthal, R. E. Structure and mixing of a transverse jet in incompressible flow. *Journal of Fluid Mechanics*, 148:405–412, 1984.
- Burkardt, J., Gunzburger, M., and Lee, H.-C. POD and CVT-based reduced-order modeling of navier–stokes flows. *Computer Methods in Applied Mechanics and Engineering*, 196(1): 337–355, 2006.
- Burton, T., Sharpe, D., Jenkins, N., and Bossanyi, E. *Wind energy handbook*. Wiley, 1st edition, 1995.

- Cacciola, S., Bertelè, M., and Bottasso, C. Simultaneous observation of wind shears and misalignments from rotor loads. In *Journal of Physics: Conference Series*, volume 753, page 052002. IOP Publishing, 2016.
- Cal, R. B., Lebrón, J., Castillo, L., Kang, H. S., and Meneveau, C. Experimental study of the horizontally averaged flow structure in a model wind-turbine array boundary layer. *Journal of Renewable and Sustainable Energy*, 2:013106, 2010.
- Calaf, M., Meneveau, C., and Meyers, J. Large eddy simulation study of fully developed wind-turbine array boundary layers. *Physics of Fluids (1994-present)*, 22(1):015110, 2010.
- Canudas, C., Astrom, K., and Braun, K. Adaptive friction compensation in dc-motor drives. *IEEE Journal on Robotics and Automation*, 3(6):681–685, 1987.
- Chakraborty, P., Balachandar, S., and Adrian, R. J. On the relationships between local vortex identification schemes. *Journal of Fluid Mechanics*, 535:189–214, 2005.
- Chamorro, L. P. and Porté-Agel, F. A wind-tunnel investigation of wind-turbine wakes: boundary-layer turbulence effects. *Boundary-Layer Meteorol.*, 132:129–149, 2009.
- Chamorro, L. P. and Porté-Agel, F. Effects of thermal stability and incoming boundary-layer flow characteristics on wind-turbine wakes: A wind-tunnel study. *Bound.-Layer Meterol.*, 136:515–533, 2010.
- Chamorro, L. P. and Porté-Agel, F. Turbulent flow inside and above a wind farm: A wind-tunnel study. *Energies*, 4(11):1916–1936, 2011.
- Chamorro, L. P., Guala, M., Arndt, R., and Sotiropoulos, F. On the evolution of turbulent scales in the wake of a wind turbine model. *Journal of Turbulence*, (13):N27, 2012.
- Chamorro, L. P., Hill, C., Morton, S., Ellis, C., Arndt, R., and Sotiropoulos, F. On the interaction between a turbulent open channel flow and an axial-flow turbine. *Journal of Fluid Mechanics*, 716:658–670, 2013a.
- Chamorro, L. P., Troolin, D. R., Lee, S.-J., Arndt, R., and Sotiropoulos, F. Three-dimensional flow visualization in the wake of a miniature axial-flow hydrokinetic turbine. *Experiments in fluids*, 54(2):1–12, 2013b.
- Chapman, S. Electric machinery fundamentals. Tata McGraw-Hill Education, 2005.
- Chatterjee, A. An introduction to the proper orthogonal decomposition. *Current science*, 78 (7):808–817, 2000.
- Cleve, J., Greiner, M., Enevoldsen, P., Birkemose, B., and Jensen, L. Model-based analysis of wake-flow data in the nysted offshore wind farm. *Wind Energy*, 12(2):125–135, 2009.
- Coleman, R. P., Feingold, A. M., and Stempin, C. W. Evaluation of the induced-velocity field of an idealized helicoptor rotor. Technical report, DTIC Document, 1945.

- Cortelezzi, L. and Karagozian, A. R. On the formation of the counter-rotating vortex pair in transverse jets. *Journal of Fluid Mechanics*, 446:347–373, 2001.
- Crastoa, G., Gravdahla, A., Castellanib, F., and Piccionib, E. Wake modeling with the actuator disc concept. *Energy Procedia.*, 24:385–392, 2012.
- Crespo, A., Hernandez, J., and Frandsen, S. Survey of modelling methods for wind turbine wakes and wind farms. *Wind Energy*, 2:1–24, 1999.
- Dahlberg, J. Å. and Medici, D. Potential improvement of wind turbine array efficiency by active wake control (awc). In *Proceedings of the European Wind Energy Conference and Exhibition*, pages 65–84, 2003.
- De Silva, C. W. Vibration monitoring, testing, and instrumentation. CRC Press, 2007.
- Dobrev, I., Maalouf, B., Troldborg, N., and Massouh, F. Investigation of the wind turbine vortex structure. In *14th international symposium on applications of laser techniques to fluid mechanics, Lisbon, Portugal*, pages 07–10, 2008.
- Dufresne, N. and Wosnik, M. Velocity deficit and swirl in the turbulent wake of a wind turbine. *Marine Technology Society Journal*, 47(4):193–205, 2013a.
- Dufresne, N. P. and Wosnik, M. Velocity deficit and swirl in the turbulent wake of a wind turbine. *Marine Technology Society Journal*, 47(4):193–205, 2013b.
- Eames, I., Johnson, P. B., Roig, V., and Risso, F. Effect of turbulence on the downstream velocity deficit of a rigid sphere. *Physics of Fluids (1994-present)*, 23(9):095103, 2011a.
- Eames, I., Jonsson, C., and Johnson, P. B. The growth of a cylinder wake in turbulent flow. *Journal of Turbulence*, 12(39):1–16, 2011b.
- España, G., Aubrun, S., Loyer, S., and Devinant, P. Spatial study of the wake meandering using modelled wind turbines in a wind tunnel. *Wind Energy*, 14(7):923–937, 2011.
- España, G., Aubrun, S., Loyer, S., and Devinant, P. Wind tunnel study of the wake meandering downstream of a modelled wind turbine as an effect of large scale turbulent eddies. *Journal of Wind Engineering and Industrial Aerodynamics*, 101:24–33, 2012.
- Fan, L. N. Turbulent buoyant jets into stratified or flowing ambient fluids. Technical report, W. M. Keck Laboratory of Hydraulics and Water Resources, 1967.
- Fang, J. and Porté-Agel, F. Large-eddy simulation of very-large-scale motions in the neutrally stratified atmospheric boundary layer. *Boundary-Layer Meteorology*, 155(3):397–416, 2015.
- Felli, M., Camussi, R., and Di Felice, F. Mechanisms of evolution of the propeller wake in the transition and far fields. *Journal of Fluid Mechanics*, 682:5–53, 2011.

- Fleming, P. A., Gebraad, P. M. O., Lee, S., van Wingerden, J., Johnson, K., Churchfield, M., Michalakes, J., Spalart, P., and Moriarty, P. Evaluating techniques for redirecting turbine wakes using SOWFA. *Renewable Energy*, 70:211–218, 2014.
- Forsting, A. R. M., Troldborg, N., Sathe, A., and Angelou, N. Analysis of two-dimensional inflow measurements by lidar-based wind scanners. 2015.
- Frandsen, S. T. On the wind speed reduction in the center of large clusters of wind turbines. *J. Wind Engng. Ind. Aerodyn.*, 39:251–256, 1992.
- Frandsen, S. T. *Turbulence and turbulence-generated structural loading in wind turbine clusters.* PhD thesis, Risø National Laboratoy, 2007.
- Frandsen, S. T., Barthelmie, R., Pryor, S., Rathmann, O., Larsen, S., Højstrup, J., and Thøgersen, M. Analytical modelling of wind speed deficit in large offshore wind farms. *Wind Energ*, 9: 39–53, 2006.
- GH WindFarmer Theory Manual. Garrad Hassan and Partners Ltd, May 2009.
- Garratt, J. R. Review: the atmospheric boundary layer. *Earth-Science Reviews*, 37(1-2):89–134, 1994.
- Gaumond, M., Réthoré, P. E., Ott, S., Peña, A., Bechmann, A., and Hansen, K. S. Evaluation of the wind direction uncertainty and its impact on wake modeling at the horns rev offshore wind farm. *Wind Energy*, 10.1002/we.1625, 2013.
- Gebraad, P. M. O., Teeuwisse, F. W., Wingerden, J. W., Fleming, P. A., Ruben, S. D., Marden, J. R., and Pao, L. Y. Wind plant power optimization through yaw control using a parametric model for wake effects a CFD simulation study. *Wind Energy*, 19:95–114, January 2014.
- Glauert, H. A general theory of the autogyro. HM Stationery Office, 1926.
- Glauert, H. Airplane propellers. In Aerodynamic theory, pages 169–360. Springer, 1935.
- Grant, I. and Parkin, P. A DPIV study of the trailing vortex elements from the blades of a horizontal axis wind turbine in yaw. *Experiments in Fluids*, 28(4):368–376, 2000.
- Grant, I., Parkin, P., and Wang, X. Optical vortex tracking studies of a horizontal axis wind turbine in yaw using laser-sheet, flow visualisation. *Experiments in fluids*, 23(6):513–519, 1997.
- Guala, M., Hommema, S., and Adrian, R. Large-scale and very-large-scale motions in turbulent pipe flow. *Journal of Fluid Mechanics*, 554:521–542, 2006.
- Haans, W. *Wind turbine aerodynamics in yaw: unravelling the measured rotor wake.* PhD thesis, TU Delft, Delft University of Technology, 2011.

- Haans, W., Sant, T., Van Kuik, G., and van Bussel, G. Measurement and modelling of tip vortex paths in the wake of a HAWT under yawed flow conditions. In *43th AIAA Aerospace Sciences Meeting and Exhibit*, pages 136–145, 2005.
- Haans, W., Sant, T., van Kuik, G., and van Bussel, G. Stall in yawed flow conditions: A correlation of blade element momentum predictions with experiments. *Journal of Solar Energy Engineering*, 128(4):472–480, 2006.
- Haans, W., van Kuik, G., and van Bussel, G. J. W. Experimentally observed effects of yaw misalignment on the inflow in the rotor plane. In *Journal of Physics: Conference Series*, volume 75, page 012012. IOP Publishing, 2007.
- Hamilton, N., Tutkun, M., and Cal, R. B. Wind turbine boundary layer arrays for cartesian and staggered configurations: Part ii, low-dimensional representations via the proper orthogonal decomposition. *Wind Energy*, 18(2):297–315, 2015.
- Hamilton, N., Tutkun, M., and Cal, R. B. Low-order representations of the canonical wind turbine array boundary layer via double proper orthogonal decomposition. *Physics of Fluids* (1994-present), 28(2):025103, 2016.
- Hancock, P. and Pascheke, F. Wind-tunnel simulation of the wake of a large wind turbine in a stable boundary layer: Part 2, the wake flow. *Boundary-layer meteorology*, 151(1):23–37, 2014.
- Hancock, P. and Zhang, S. A wind-tunnel simulation of the wake of a large wind turbine in a weakly unstable boundary layer. *Boundary-Layer Meteorology*, 156(3):395–413, 2015.
- Hansen, K. S., Barthelmie, R. J., Jensen, L. E., and Sommer, A. The impact of turbulence intensity and atmospheric stability on power deficits due to wind turbine wakes at horns rev wind farm. *Wind Energy*, 15(1):183–196, 2012.
- Hansen, M. O. L., Sørensen, J. N., Voutsinas, S., Sørensen, N., and Madsen, H. A. State of the art in wind turbine aerodynamics and aeroelasticity. *Progress in aerospace sciences*, 42(4): 285–330, 2006.
- Heyes, A., Jones, R., and Smith, D. Wandering of wing-tip vortices. In *Proceedings of the 12th International Symposium on Applications of Laser Techniques to Fluid Mechanics*, pages 35–3, 2004.
- Hibbs, B. D. HAWT performance with dynamic stall. Technical report, Solar Energy Research Institute, 1986.
- Holmes, P., Lumley, J. L., and Berkooz, G. *Turbulence, coherent structures, dynamical systems and symmetry*. Cambridge university press, 1998.
- Howard, K., Hu, J., Chamorro, L., and Guala, M. Characterizing the response of a wind turbine model under complex inflow conditions. *Wind Energy*, 18(4):729–743, 2015.

- Howard, K. B. and Guala, M. Upwind preview to a horizontal axis wind turbine: a wind tunnel and field-scale study. *Wind Energy*, 2015.
- Howland, M. F., Bossuyt, J., A., M.-T. L., Meyers, J., and Meneveau, C. Wake structure in actuator disk models of wind turbines in yaw under uniform inflow conditions. *Journal of Renewable and Sustainable Energy*, 8:043301, 2016.
- Hughes, A. Electric motors and drives: fundamentals, types and applications. Newnes, 2013.
- Hutchins, N. and Marusic, I. Evidence of very long meandering features in the logarithmic region of turbulent boundary layers. *Journal of Fluid Mechanics*, 579:1–28, 2007.
- Hutchins, N., Chauhan, K., Marusic, I., Monty, J., and Klewicki, J. Towards reconciling the large-scale structure of turbulent boundary layers in the atmosphere and laboratory. *Boundary-layer meteorology*, 145(2):273–306, 2012.
- Iungo, G. V., Viola, F., Camarri, S., Porté-Agel, F., and Gallaire, F. Linear stability analysis of wind turbine wakes performed on wind tunnel measurements. *Journal of Fluid Mechanics*, 737:499–526, 2013.
- Jensen, N. O. A note on wind turbine interaction. Technical Report Risø-M-2411, Risoe National Laboratory, Roskilde, Denmark, 1983.
- Jiménez, Á., Crespo, A., and Migoya, E. Application of a LES technique to characterize the wake deflection of a wind turbine in yaw. *Wind energy*, 13(6):559–572, 2010.
- Johansson, P. B. V., George, W. K., and Gourlay, M. J. Equilibrium similarity, effects of initial conditions and local Reynolds number on the axisymmetric wake. *Phys. Fluids.*, 15(3): 603–617, 2003.
- Johnson, P. B., Jonsson, C., Achilleos, S., and Eames, I. On the spread and decay of wind turbine wakes in ambient turbulence. In *Journal of Physics: Conference Series*, volume 555, page 012055. IOP Publishing, 2014.
- Kang, H. and Meneveau, C. Direct mechanical torque sensor for model wind turbines. *Measurement Science and Technology*, 21(10):105206, 2010.
- Katić, I., Højstrup, J., and Jensen, N. A simple model for cluster efficiency. In *Proceedings of the European wind energy association conference and exhibition*, pages 407–409, Rome, Italy, 1986.
- Kelso, R. M., Lim, T. T., and Perry, A. E. An experimental study of round jets in cross-flow. *Journal of fluid mechanics*, 306:111–144, 1996.
- Kikkert, G. A. *BUOYANT JETS WITH TWO AND THREE-DIMENSIONAL TRAJECTORIES*. PhD thesis, University of Canterbury, 2006.

- Kim, K. and Adrian, R. Very large-scale motion in the outer layer. *Physics of Fluids (1994-present)*, 11(2):417–422, 1999.
- Kiranoudis, C. T. and Maroulis, Z. B. Effective short-cut modelling of wind park efficiency. *Renewable Energy*, 11:439–457, 1997.
- Krishnan, R. Permanent magnet synchronous and brushless DC motor drives. CRC press, 2009.
- Krogstad, P. and Adaramola, M. S. Performance and near wake measurements of a model horizontal axis wind turbine. *Wind Energy*, 15(5):743–756, 2012.
- Laitone, E. Wind tunnel tests of wings at reynolds numbers below 70 000. *Experiments in Fluids*, 23(5):405–409, 1997.
- Larsen, G. C. and Hansen, K. S. Full-scale measurements of aerodynamic induction in a rotor plane. In *Journal of Physics: Conference Series*, volume 555, page 012063. IOP Publishing, 2014.
- Larsen, G. C., Madsen, H. A., Thomsen, K., and Larsen, T. J. Wake meandering: a pragmatic approach. *Wind energy*, 11(4):377–395, 2008.
- Lee, J. H. and Chu, V. *Turbulent jets and plumes: a Lagrangian approach.* Springer Science & Business Media, 2012.
- Lee, J. H. and Sung, H. J. Very-large-scale motions in a turbulent boundary layer. *Journal of Fluid Mechanics*, 673:80–120, 2011.
- Legendre, D., Merle, A., and Magnaudet, J. Wake of a spherical bubble or a solid sphere set fixed in a turbulent environment. *Physics of Fluids (1994-present)*, 18(4):048102, 2006.
- Lignarolo, L., Ragni, D., Krishnaswami, C., Chen, Q., Simao Ferreira, C., and van Bussel, G. Experimental analysis of the kinetic energy transport and turbulence production in the wake of a model wind turbine. In *ICOWES Conference, Lyngby*, pages 16–19, 2013.
- Lignarolo, L., Ragni, D., Krishnaswami, C., Chen, Q., Ferreira, C. S., and Van Bussel, G. Experimental analysis of the wake of a horizontal-axis wind-turbine model. *Renewable Energy*, 70: 31–46, 2014.
- Lissaman, P. B. S. Energy effectiveness of arbitrary arrays of wind turbines. AIAA, 17:8, 1979.
- Lu, H. and Porté-Agel, F. Large-eddy simulation of a very large wind farm in a stable atmospheric boundary layer. *Physics of Fluids* (1994-present), 23(6):065101, 2011.
- Mahesh, K. The interaction of jets with crossflow. *Annual review of fluid mechanics*, 45: 379–407, 2013.
- Manwell, J. F., McGowan, J. G., and Rogers, A. L. *Wind energy explained: theory, design and application.* John Wiley & Sons, 2010.

- Markfort, C., Zhang, W., and Porté-Agel, F. Turbulent flow and scalar transport through and over aligned and staggered wind farms. *Journal of Turbulence*, 13(1):N33, 2012.
- Marmidis, G., Lazarou, S., and Pyrgioti, E. Optimal placement of wind turbines in a wind park using monte carlo simulation. *Renewable Energy*, 33:1455–1460, 2008.
- Marzouk, Y. M. and Ghoniem, A. F. Vorticity structure and evolution in a transverse jet. *Journal of Fluid Mechanics*, 575:267–305, 2007.
- Medici, D. and Alfredsson, P. Measurement on a wind turbine wake: 3D effects and bluff body vortex shedding. *Wind Energy*, 9:219–236, 2006.
- Medici, D., Dahlberg, J.-Å., and Alfredsson, P. H. Measurements of the flow upstream a rotating wind turbine model. In *Progress in Turbulence III*, pages 87–90. Springer, 2009.
- Medici, D., Ivanell, S., Dahlberg, J.-Å., and Alfredsson, P. H. The upstream flow of a wind turbine: blockage effect. *Wind Energy*, 14(5):691–697, 2011.
- Mehta, D., Van Zuijlen, A., Koren, B., Holierhoek, J., and Bijl, H. Large eddy simulation of wind farm aerodynamics: A review. *Journal of Wind Engineering and Industrial Aerodynamics*, 133:1–17, 2014.
- Meyer, K. E., Pedersen, J. M., and Özcan, O. A turbulent jet in crossflow analysed with proper orthogonal decomposition. *Journal of Fluid Mechanics*, 583:199–227, 2007.
- Meyer, K. E., Naumov, I. V., Kabardin, I., Mikkelsen, R., and Sørensen, J. N. PIV in a model wind turbine rotor wake. In *10th International Symposium on Particle Image Velocimetry, Delft, The Netherlands, July 1-3, 2013*, 2013.
- Micallef, D., Ferreira, C. S., Sant, T., and van Bussel, G. Wake skew angle variation with rotor thrust for wind turbines in yaw based on the mexico experiment. In *5th PhD Seminar on Wind Energy in Europe*, 2009.
- Micallef, D., Bussel, G., Ferreira, C. S., and Sant, T. An investigation of radial velocities for a horizontal axis wind turbine in axial and yawed flows. *Wind Energy*, 16(4):529–544, 2013.
- Muppidi, S. and Mahesh, K. Two-dimensional model problem to explain counter-rotating vortex pair formation in a transverse jet. *Physics of Fluids (1994-present)*, 18(8):085103, 2006.
- Nygaard, N., Jensen, L., Downey, R., and Méchali, M. Construction and validation of a new offshore wake model. In *ICOWES Conference*, pages 26–37, Lyngby, June 2013.
- Odemark, Y. and Fransson, J. H. The stability and development of tip and root vortices behind a model wind turbine. *Experiments in fluids*, 54(9):1–16, 2013.
- Okulov, V. L., Naumov, I. V., Mikkelsen, R. F., Kabardin, I. K., and Sørensen, J. N. A regular strouhal number for large-scale instability in the far wake of a rotor. *Journal of Fluid Mechanics*, 747:369–380, 2014.

- Okulov, V. L., Naumov, I. V., Mikkelsen, R. F., and Sørensen, J. N. Wake effect on a uniform flow behind wind-turbine model. In *Journal of Physics: Conference Series*, volume 625, page 012011. IOP Publishing, 2015.
- Olsson, H., Åström, K. J., De Wit, C. C., Gäfvert, M., and Lischinsky, P. Friction models and friction compensation. *European journal of control*, 4(3):176–195, 1998.
- Ooms, G. A new method for the calculation of the plume path of gases emitted by a stack. *Atmospheric Environment (1967)*, 6(12):899–909, 1972.
- Ozbay, A., Tian, W., Yang, Z., and Hu, H. Interference of wind turbines with different yaw angles of the upstream wind turbine. In *42nd AIAA Fluid Dynamics Conference and Exhibit*, page 2719, 2012.
- Pedersen, T. F. On wind turbine power performance measurements at inclined airflow. *Wind Energy*, 7(3):163–176, 2004.
- Pelletier, A. and Mueller, T. J. Low reynolds number aerodynamics of low-aspect-ratio, thin/flat/cambered-plate wings. *Journal of Aircraft*, 37(5):825–832, 2000.
- Perry, A., Henbest, S., and Chong, M. A theoretical and experimental study of wall turbulence. *Journal of Fluid Mechanics*, 165:163–199, 1986.
- Pope, S. B. Turbulent flows. Cambridge university press, 2000.
- Porté-Agel, F., Meneveau, C., and Parlange, M. B. A scale-dependent dynamic model for large-eddy simulation: application to a neutral atmospheric boundary layer. *Journal of Fluid Mechanics*, 415:261–284, 2000.
- Porté-Agel, F., Wu, Y. T., Lu, H., and Conzemius, R. J. Large-eddy simulation of atmospheric boundary layer flow through wind turbines and wind farms. *Journal of Wind Engineering and Industrial Aerodynamics*, 99(4):154–168, 2011.
- Porté-Agel, F., Wu, Y. T., and Chen, C. H. A numerical study of the effects of wind direction on turbine wakes and power losses in a large wind farm. *Energies*, 6(10):5297–5313, 2013.
- Qing'an, L., Murata, J., Endo, M., Maeda, T., and Kamada, Y. Experimental and numerical investigation of the effect of turbulent inflow on a Horizontal Axis Wind Turbine (Part I: Power performance). *Energy*, 113(C):713–722, 2016.
- Rajaratnam, N. Turbulent jets. Elsevier, 1976.
- Sant, T. *Improving BEM-Based Aerodynamic Models in Wind Turbine Design Codes.* PhD thesis, Delft University of Tecnology, 2007.
- Sarmast, S., Dadfar, R., Mikkelsen, R. F., Schlatter, P., Ivanell, S., Sørensen, J. N., and Henningson, D. S. Mutual inductance instability of the tip vortices behind a wind turbine. *Journal of Fluid Mechanics*, 755:705–731, 2014.

- Scheffer, C. and Girdhar, P. *Practical machinery vibration analysis and predictive maintenance*. Elsevier, 2004.
- Sen, P. C. Principles of electric machines and power electronics. John Wiley & Sons, 2007a.
- Sen, P. C. Principles of electric machines and power electronics. John Wiley & Sons, 2007b.
- Sharma, S. Basics of Electrical Engineering. IK International Pvt Ltd, 2007.
- Sheldahl, R. E. and Klimas, P. C. Aerodynamic characteristics of seven symmetrical airfoil sections through 180-degree angle of attack for use in aerodynamic analysis of vertical axis wind turbines. Technical report, Sandia National Labs., Albuquerque, NM (USA), 1981.
- Shen, W. Z., Mikkelsen, R., Sørensen, J. N., and Bak, C. Tip loss corrections for wind turbine computations. *Wind Energy*, 8(4):457–475, 2005.
- Sherry, M., Nemes, A., Jacono, D. L., Blackburn, H. M., and Sheridan, J. The interaction of helical tip and root vortices in a wind turbine wake. *Physics of Fluids (1994-present)*, 25(11): 117102, 2013a.
- Sherry, M., Sheridan, J., and Jacono, D. L. Characterisation of a horizontal axis wind turbine's tip and root vortices. *Experiments in Fluids*, 54(3):1–19, 2013b.
- Simley, E., Pao, L. Y., Gebraad, P., and Churchfield, M. Investigation of the impact of the upstream induction zone on lidar measurement accuracy for wind turbine control applications using large-eddy simulation. In *Journal of Physics: Conference Series*, volume 524, page 012003. IOP Publishing, 2014.
- Simley, E., Angelou, N., Mikkelsen, T., Sjöholm, M., Mann, J., and Pao, L. Y. Characterization of wind velocities in the upstream induction zone of a wind turbine using scanning continuous-wave lidars. *Journal of Renewable and Sustainable Energy*, 8(1):013301, 2016.
- Sirovich, L. Turbulence and the dynamics of coherent structures. part i: Coherent structures. *Quarterly of applied mathematics*, 45(3):561–571, 1987.
- Sørensen, J. N. Aerodynamic aspects of wind energy conversion. *Annual Review of Fluid Mechanics*, 43:427–448, 2011.
- Sørensen, J. N. General Momentum Theory for Horizontal Axis Wind Turbines. Springer, 2015.
- Sørensen, J. N., Mikkelsen, R. F., Henningson, D. S., Ivanell, S., Sarmast, S., and Andersen, S. J. Simulation of wind turbine wakes using the actuator line technique. *Philosophical Transactions of the Royal Society of London A: Mathematical, Physical and Engineering Sciences*, 373(2035):20140071, 2015.
- Spera, D. A. Wind turbine technology. 1994.

- Stein, V. P. and Kaltenbach, H.-J. Wind-tunnel modelling of the tip-speed ratio influence on the wake evolution. In *Journal of Physics: Conference Series*, volume 753, page 032061. IOP Publishing, 2016.
- Sunada, S., Sakaguchi, A., and Kawachi, K. Airfoil section characteristics at a low reynolds number. *Journal of Fluids Engineering*, 119(1):129–135, 1997.
- Sunada, S., Yasuda, T., Yasuda, K., and Kawachi, K. Comparison of wing characteristics at an ultralow reynolds number. *Journal of aircraft*, 39(2):331–338, 2002.
- Tennekes, H. and Lumley, J. L. A first course in turbulence. The MIT press, 1972.
- Theraja, B. and Theraja, A. K. *A text book of electrical technology*, volume 2. S Chand & Co Ltd, 2006.
- Thøgersen, M. L. Wind pro / park: Introduction to wind turbine wake modelling and wake generated turbulence. Technical report, EMD International A/S, Niels Jernes Vej 10, DK-9220 Aalborg, Denmark, 2005.
- Tjahjowidodo, T., Al-Bender, F., Van Brussel, H., and Symens, W. Friction characterization and compensation in electro-mechanical systems. *Journal of sound and vibration*, 308(3): 632–646, 2007.
- Tobin, N., Hamed, A. M., and Chamorro, L. P. An experimental study on the effects of winglets on the wake and performance of a model wind turbine. *Energies*, 8(10):11955–11972, 2015.
- Troldborg, N., Sørensen, J., and Mikkelsen, R. Actuator line simulation of wake of wind turbine operating in turbulent inflow. In *Journal of Physics: Conference Series*, volume 75, page 012063. IOP Publishing, 2007.
- Tropea, C., Yarin, A. L., and Foss, J. F. *Springer handbook of experimental fluid mechanics*, volume 1. Springer Science & Business Media, 2007.
- Vermeer, L., Sørensen, J., and Crespo, A. Wind turbine wake aerodynamics. *Progress in Aerospace Sciences*, 39:467–510, 2003.
- Vermeulen, P. E. J. An experimental analysis of wind turbine wakes. In *3rd Int. Symp. on Wind Energy Systems*, pages 431–450, Lyngby, 1980.
- Viola, E, Iungo, G. V., Camarri, S., Porté-Agel, E, and Gallaire, F. Prediction of the hub vortex instability in a wind turbine wake: stability analysis with eddy-viscosity models calibrated on wind tunnel data. *Journal of Fluid Mechanics*, 750:R1, 2014.
- Wang, X. and Kikkert, G. A. Behaviour of oblique jets released in a moving ambient. *Journal of Hydraulic Research*, 52(4):490–501, 2014.
- Whale, J., Anderson, C. G., Bareiss, R., and Wagner, S. An experimental and numerical study of the vortex structure in the wake of a wind turbine. *Journal of Wind Engineering and Industrial Aerodynamics*, 84(1):1–21, 2000.

- White, F. M. Fluid Mechanics. McGraw-Hill, 2009.
- Widnall, S. E. The stability of a helical vortex filament. *Journal of Fluid Mechanics*, 54(04): 641–663, 1972.
- Wilson, R. E. and Lissaman, P. B. Applied aerodynamics of wind power machines. Technical report, Oregon State Univ., Corvallis (USA), 1974.
- Wilson, R. E., Lissaman, P. B., and Walker, S. N. Aerodynamic performance of wind turbines. final report. Technical report, Oregon State Univ., Corvallis (USA). Dept. of Mechanical Engineering, 1976.
- Wu, J. S. and Faeth, G. M. Sphere wakes at moderate Reynolds numbers in a turbulent environment. *AIAA journal*, 32(3):535–541, 1994.
- Wu, Y. and Porté-Agel, F. Large-eddy simulation of wind-turbine wakes: Evaluation of turbine parametrisations. *Bound.-Layer Meterol.*, 138:345–366, 2011.
- Wu, Y. and Porté-Agel, F. Atmospheric turbulence effects on wind-turbine wakes: An LES study. *Energies*, 5:5340–5362, 2012.
- Xie, S. and Archer, C. Self-similarity and turbulence characteristics of wind turbine wakes via large-eddy simulation. *Wind Energy*, 18:1815–1838, October 2015.
- Yang, Z., Sarkar, P., and Hu, H. Visualization of the tip vortices in a wind turbine wake. *Journal of Visualization*, 15(1):39–44, 2012.
- Zhang, W., Markfort, C. D., and Porté-Agel, F. Near-wake flow structure downwind of a wind turbine in a turbulent boundary layer. *Experiments in fluids*, 52(5):1219–1235, 2012.
- Zhang, W., Markfort, C. D., and Porté-Agel, F. Wind-turbine wakes in a convective boundary layer: A wind-tunnel study. *Boundary-Layer Meteorology*, 146(2):161–179, 2013.
- Zhou, J., Adrian, R. J., Balachandar, S., and Kendall, T. Mechanisms for generating coherent packets of hairpin vortices in channel flow. *Journal of Fluid Mechanics*, 387:353–396, 1999.

Majid Bastankhah

 $Curriculum\ Vitae$

Avenue Jomini 4, CH-1004 Lausanne, Switzerland

+41 78 9619502

majid.bastankhah@epfl.ch

₱ Place of Birth: Iran, Mashhad

o Date of Birth: 11 October, 1986

EDUCATION

2012 – present	Ph.D. in Mechanical engineering EPFL, Lausanne, Switzerland
2009 - 2012	M.Sc. in Mechanical Engineering Sharif University of Technology, Tehran, Iran
2004 - 2009	B.Sc. in Mechanical Engineering Sharif University of Technology, Tehran, Iran

PROFESSIONAL EXPERIENCE

Doctoral assistant	2012 - 2016
Laboratory of Wind Engineering and Renewable Energy (WIRE), EPFL, Switzerland	
Senior Simulator of Turbo Machinery	2010 - 2012

Farab company, Tehran, Iran

RESEARCH INTERESTS

Turbulence

Atmospheric boundary layers Experimental fluid mechanics Environmental fluid mechanics

Honors & Awards

2014	Best Poster Presentation 21st Symposium on Boundary Layers and Turbulence, Leeds, United Kingdom 9-13 June 2014
2014	Outstanding Student Poster (OSP) Award EGU General Assembly, Vienna, Austria, 27 April-02 May 2014

2013 Best poster award Green days, EPFL, Switzerland

2010 Best Student of Higher Education Sharif University of Technology, Tehran, Iran

2009 National Gold Medal in Mechanical Engineering Olympiad $\it Tehran, Iran$

2009 Ranked 1st in the Nationwide M.Sc. Entrance Exam in Mechanical Engineering Tehran, Iran

2004 Ranked 83th in the Nationwide B.Sc. Entrance Exam in Mathematic and Physic Tehran, Iran

131

JOURNAL PUBLICATIONS

- M. Bastankhah and F. Porté-Agel, A new analytical model for wind-turbine wakes, *Renewable Energy*, 70:116–123, 2014.
- M. Bastankhah and F. Porté-Agel, Experimental and theoretical study of wind turbine wakes in yawed conditions, *Journal of Fluid Mechanics*, 806:506–541, 2016.
- M. Bastankhah and F. Porté-Agel, Wind tunnel study of the boundary layer flow interaction with a wind turbine under different operating conditions, under review in *Physics of Fluids*, 2016.
- M. Bastankhah and F. Porté-Agel, A new miniature wind turbine for wind tunnel experiments: design, performance analysis and wake measurements, under review in *Experiments in Fluids*, 2016.

Conference Publications

- M. Bastankhah and F. Porté-Agel. A wind-tunnel investigation of wind-turbine wakes in yawed conditions, *Journal of Physics: Conference Series*, 625:012014, 2015.
- **M. Bastankhah** and F. Porté-Agel. A new analytical model for wind-Turbine wakes. *ICOWES conference*, Lyngby, 2013.

Reference

Prof. Fernando Porté-Agel, EPFL, Switzerland

fernando.porte-agel@epfl.ch